UC Davis
UC Davis Electronic Theses and Dissertations

Title

A Cognitively Informed and Network Based Investigation of Human Neural Activities, Behaviors, and Performance in Human-Autonomy Teaming Tasks

Permalink

https://escholarship.org/uc/item/6735d0s8

Author

Bales, Gregory

Publication Date

2023

Peer reviewed|Thesis/dissertation

A Cognitively Informed and Network Based Investigation of Human Neural Activities, Behaviors, and Performance in Human-Autonomy Teaming Tasks

By

GREGORY LYLE BALES
DISSERTATION

Submitted in partial satisfaction of the requirements for the degree of

DOCTOR OF PHILOSOPHY

in

Mechanical and Aerospace Engineering

in the

OFFICE OF GRADUATE STUDIES

of the

UNIVERSITY OF CALIFORNIA

DAVIS

Approved:

_____

Zhaodan Kong, Chair

_____

Sanjay Joshi

_____

Allison Anderson

Committee in Charge

2023

Para mi querido Abuelito

Contents

LIST OF FIGURES

LIST OF TABLES

ABSTRACT

A Cognitively Informed and Network Based Investigation of Human Neural Activities, Behaviors, and Performance in Human-Autonomy Teaming Tasks

Human-autonomy teams are expected to provide solutions in a wide range of applications, such as human directed search and rescue, hazard containment and mobilization, and space exploration. These teams consist of autonomous agents that coordinate their actions with the human partner to achieve common goals. Despite the advancements of current autonomous systems, it is the human's ability to engage their knowledge and expertise that makes human-autonomy teams especially effective in tasks dominated by dynamic and uncertain conditions. The human and their autonomous teammate should have shared plans and a similar focus of attention. However, studies have shown that a human's miscomprehension of an autonomous system's state, decisions, or course of action can result in misuse or disuse of the agent, causing a reduction in team performance. The aim of this dissertation is to improve human-autonomy team task proficiency by investigating methods to measure changes in human cognitive state as reflected in neurophysiological measures using methods derived from network science. This work is comprised of two primary studies. In the first study, we examined human behaviors and brain activity acquired via electroencephalography (EEG) to probe the interactions between cognitive processes, behaviors, and performance in a human-multiagent team task. We showed that measurable changes in brain activity indicate a higher burden on the cognitive resources associated with visual-spatial reasoning required to estimate a more complex kinematic state of robotic agents. These conclusions were reinforced by complementary behavioral shifts in gaze and pilot inputs. Next, we showed that EEG inter-channel connectivity network metrics distinguish gaze behaviors associated with the attention process more effectively than traditional single-channel features. In the second study we explored the relationship between neurophysiological features and human trust in an autonomous system while performing a team task. Trust prediction models were constructed using a variety of feature types determined from an EEG timeseries. A comparison of model performance

between traditional EEG signal powers with inter-channel connectivity network metrics revealed that measures of dynamic changes in synchronous behavior between distant brain regions can capture cognitive activities that predict a human's trust in an autonomous system. We showed that both single-channel powers and network-metrics defined from brain regions associated with reasoning and attention have the greatest impact on trust prediction. In a third study, we explore the interaction between behaviors and performance for subjects of various skills in a manual grinding task. We show that there were observable and distinguishable sensorimotor behaviors associated with two distinct techniques utilized by the individual subjects, and that task performance is affected by these techniques.

Acknowledgments

Not once throughout this long, and often meandering, journey did I walk it alone. I am eternally grateful for the guidance and support from those who encouraged and challenged me.

I would first like to thank my advisor, Professor Zhaodan Kong for his support and guidance. His willingness to take a chance on an older student, and his patience have been invaluable.

I am deeply grateful to Professor Sanjay Joshi, a member of my Committee, and Professor Barbara Linke. Both offered invaluable emotional support at the moments of greatest need.

I would like to thanks Professor Steve Robinson and Professor Allison Anderson, also a member of my Committee, for the amazing opportunity to be part of the NASA HOME team.

In addition, I want to thank all of the students in the University of California, Davis in the Cyber-Human-Physical Systems Laboratory, especially Dr. Peng Wei, who let me vent and added extra perspective on the graduate school experience both in and out of the lab.

And from the bottom of my heart, thank you to my family. For my Mother, Father, Amanda, Whitley, and Audrey, all of whom gave me unwavering support, unfathomable patience, and unconditional love.

Chapter 1

Introduction

Human-autonomy teams are expected to provide solutions in a wide range of applications, such as human directed search and rescue [1], hazard containment and mobilization [2], and space exploration [3]. These teams consist of autonomous agents that coordinate their actions with the human partner to achieve a common goal. Despite the advancements of current autonomous systems, it is the human's ability to engage their knowledge and expertise, both general and domain specific, that makes human-autonomy teams especially effective in tasks dominated by dynamic and uncertain conditions. In many applications, humans are required to be "in-the-loop", implying an active, rather than supervisory role. These types of human-autonomy tasks present a fundamental problem: how can we optimize a natural and effective collaboration between the autonomy and its human partner? Considering the various cognitive constraints placed upon the human, this problem can be particularly difficult to solve. Consequently, a major goal in human-autonomy teaming (HAT) research is to maximize task performance through a fusion of the autonomous features of the agent(s) and the cognitive skills of the human.

1.1 Human-Autonomy Teaming

As autonomous systems become more capable of reasoning and decision making in the presence of uncertainty, the interaction between humans and these systems can be more accurately described in terms of human-human teaming. Consequently, the human and their autonomous teammate should have shared plans [4], and a similar focus of attention [5] in order to maximize team task efficiency. Therefore, a broader

investigation of human-autonomy interaction requires an examination of human factors such as workload and situation awareness [6]. It is critical for the human to comprehend and predict the behaviors of the agent within the context of achieving their shared goals. Likewise, it is critical for the autonomous agent to understand the cognitive state of the human in order modulate or communicate their own intentions. Achieving effective and efficient human-autonomy team task performance can be significantly augmented if the autonomous agent has direct access to the internal cognitive state of the human in real-time.

Significant work has examined what information can be effectively passed to the human operator [7] or how its presentation can affect the team-performance [8]. Other work has attempted to construct an adaptable teamwork-centered interface by adopting characteristics of human-to-human teams [9]. Recent research has also examined how robots can adapt their interactions via an observation of the external actions and decisions to reason about the mental state of their human partner [10]. Nevertheless, these efforts do not examine detailed aspects of human cognitive behavior. As autonomous agents become more sophisticated and independent, it is critical for the agent to understand behaviors and expected outcomes of the human in order to make appropriate decisions about their use [11]. Access to the real-time mental state of the human could be used to modify the behavior of autonomous systems [12]. For example, adaptable automation could be calibrated to specific individual differences [13].

1.1.1 Human Cognitive State Estimation

Even a seemingly basic scenario, such as controlling a robotic group through direct teleoperation, can be a challenging task. Successful performance can impose a heavy burden on a human operator's cognitive resources [14]. The underlying mental action and processes related to memory, attention, reasoning, problem-solving, comprehension, and language organization is known as a person's cognitive state [15].

1.1.1.1 Electroencephalogram

Extensive research in neuroscience has demonstrated that cortical activation within given regions increases with cognitive demands [16], and neuroimaging measures of cortical

activity (Table A.2) can provide an index of cognitive activity. Electroencephalography (EEG) is a common, noninvasive method for recording brain signals in humans. The electrical activity of neurons within the neocortex of the brain generate detectable voltages that can be recorded via electrodes placed directly onto the scalp [16]. Attention, memory performance, and cognitive workload have been studied using signals acquired via EEG [17,18]. EEG has also been employed in social human-robot interaction research [19] and Brain Computer Interface (BCI) implementations [20]. These studies primarily include the magnitude and spatial distribution of spectral power in the θ (4-8Hz), α (8-12Hz), β (12-30Hz), and γ (>30Hz) bands. For example, modulations of θ-band power in the frontal cortex of the brain are thought to be a key mechanism of sustained attention and goal-related behaviors. Increased θ is a hallmark of improved task performance and sustained attention, known to reflect the cognitive demands of a given task [21,22]. By comparison, modulations in α-band oscillations over the entire head occur in all the historic cognitive domains of perception, attention, and access to working memory [23].

EEG has proven to be an effective tool for estimating certain human cognitive states such as fatigue, workload, and vigilance in rapid timescales [24,25]. However, cognitive function is not necessarily confined to monolithic, self contained regions of the brain. Each cortical area can perform multiple cognitive functions, and conversely, many cognitive function are performed by more than one area. It is more accurate to state that perception and cognition emerge through cooperation of numerous distinct brain regions [23].

1.1.1.2 Network Neuroscience

The human brain is known to have distributed neurophysiological networks consisting of functionally integrated clusters of synchronized activity with sparse connections between them [26]. The topology of large scale cortical networks changes dynamically during cognition, adapting itself to the demands of the task and resource limitations of different cortical areas [27]. For example, there is evidence demonstrating that cognitive control networks shift their connectivity in a task dependent manner to dynamically reconfigure brain networks for goal directed behavior [28]. It is widely believed that the attention system is controlled by a distributed network of brain regions [29]. In neuroscience,

descriptive measures of the local and global features of inter-channel network topology have been widely applied to EEG data. For example, functional long range α-band interactions between brain regions exert top-down influences to inhibit sensory susceptibility [30]. These analyses have revealed nonrandom topological aspects, such as high clustering or short path length [31] and metrics of dynamic functional connectivity may indicate changes in macroscopic neural activity patterns underlying critical aspects of cognition and behavior [32].

1.2   This Dissertation

The use of EEG band power analysis in cognitive research is extremely mature. However, few studies have investigated the use of dynamic EEG functional connectivity networks to estimate human cognitive state in real time, and fewer still have attempted to use them in human-autonomy team studies [33]. The incorporation of EEG measures and methods derived from network science into human-autonomy team applications remains a relatively open and unexplored field.

A major goal in human-autonomy teaming (HAT) is the development of systems that can automatically support the operator in executing working tasks. An important step in achieving that goal is to develop accurate real-time estimates of the changes in human cognitive state. **In this research, I propose to use elements of cognitive science and the mathematics of network theory to identify and decode changes in human cognitive activity during human-automation team tasks.**

The research conducted for this dissertation consisted of three human subject experiments.

Experiment 1: An EEG Network Examination of Human Robot Teaming

We explored both behaviors and neurophysiological characteristics of human subjects as they piloted a team of robots in a target identification and acquisition task. It is the

4

difficulty in estimating the kinematic state of the robot group that is the main experimental factor. In addition to gaze and pilot input, we examine both spectral powers and metrics of EEG inter-channel functional connectivity networks based on ensemble averages of performance within each subject. The results of this investigation have been published in [34], [35], and [36]. The details of this experiment are outlined in Chapter 2.

Experiment 2: An EEG Network Examination of Human Trust in Autonomy

We explore how a human's trust in an autonomous system correlates with changes in neurophysiological characteristics as they perform a collaborative sorting task in concert with a simulated robotic arm. It is the capability of the robot that is the main experimental factor used to elicit changes in trust. We examine temporal changes in both spectral powers and metrics of EEG inter-channel functional connectivity networks. The results of this experiment have been submitted for publication [37]. The details of this experiment are outlined in Chapter 3.

Experiment 3: Investigating Human Behaviors in a Manual Grinding Task

We investigated the gaze and motor behaviors that were elicited by humans of different levels of experience as they perform a manual grinding task. The results of this investigation have been published in [38], [39], and [40]. The details of this experiment are outlined in Chapter 4.

Chapter 2

An EEG Network Examination of Human Robot Teaming

Preface

Effective human-multiagent teams will incorporate the cognitive skills of the human with the autonomous capabilities of the multiagent group to maximize task performance. However, producing a seamless fusion requires a greater understanding of the human's cognitive state as it reacts to uncertainties in both the task environment and agent dynamics. In this chapter we present our experiment regarding human robot teaming. We present a comprehensive analysis of human-multiagent interaction as cognition affects behaviors which determine performance, as shown in Figure 2.1.

The major contributions of this chapter are as follows: 1) We show that the decrease in task performance associated with geometric complexity (GC) is directly reflected in neurophysiological and behavioral measures. Furthermore, we show that higher performing subjects engage more actively in the task by utilizing a greater amount of visual-spatial reasoning and focused attention; 2) We propose a network-cognitive-scientific approach of analyzing EEG data. We show that a set of features based on dynamic networks of EEG functional connectivity can be used to distinguish gaze behaviors associated with attention, thereby establishing a correlation of cognitive processes with behaviors in real time. As far as we know, this is one of the first instances such a methodology has been applied to analyze human-multiagent performance using data obtained from testing in a real, rather than simulated environments.

The contents of this chapter have been previously published in [34], [35], and [36].
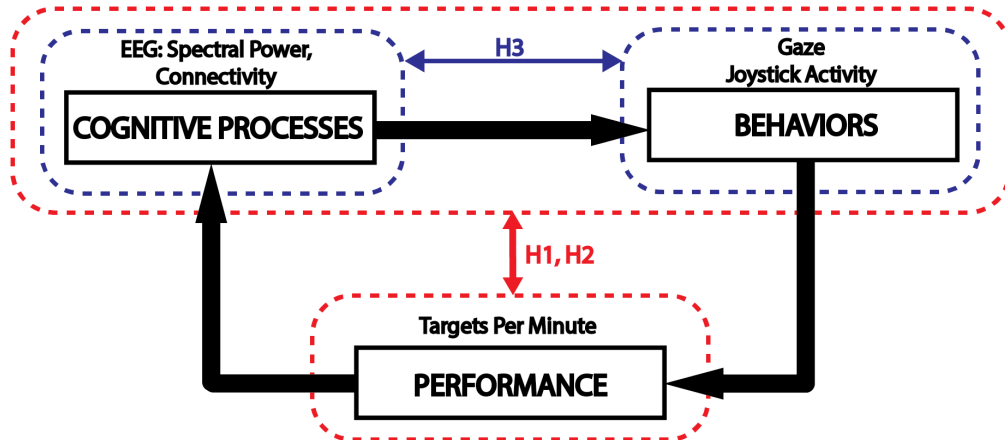
Figure 2.1: Performance to behavior loop connecting the cognitive processes that drive behaviors, which in turn affect the overall task performance. The four measures and the interrelationships examined by each hypothesis are indicated: H1 and H2 in red, and H3 in blue.

2.1 Introduction

To date, researchers have made key advancements by testing human subjects within simulated environments [41]. Such methods are justified by the fact that controlled environments greatly limit the effects of confounding factors. Nevertheless, it has been observed [42] that given identical tasks, testing in real, rather than simulated environments can increase the workload [43] and reaction times of the human subjects. Test scenarios in which human subjects interact with real robots provide the opportunity to gain insight into how humans handle, not only the complexities of robot dynamics and variations in environment, but also the inherent uncertainties in the human-robot interaction.

2.1.1 Present Study

As an essential property of cognitive operation, attention can be roughly divided into two categories: 1) bottom-up, a stimulus-driven process in which a salient sensory event

captures focus; and 2) top-down, a voluntary goal-driven process based on tasks, memory, knowledge, and expectations [44]. Memory, or more specifically working memory, is the cognitive capacity to maintain and manipulate information for limited periods in the absence of continuous sensory stimulation [45]. Working memory has been implicated as the primary factor in the ability to control attention [46]. As mentioned in Chapter 1, attention, memory performance, and cognitive workload have been studied using signals acquired via EEG. In addition, a behavioral proxy of attention often used in research is gaze, the coordinated motion of the eyes and the head. A majority of studies are concerned with two types of gaze movements: saccades, rapid movements in which the gaze shifts from one location to another; and fixations, the period during which the gaze is stationary and useful information is collected from the area of interest [47].

Given the attention-demanding nature of many human-multiagent team tasks, a natural question arises: *Does complexity of the kinematic state of the multiagent team impact task performance, and if so, is it reflected in the behavioral and neurophysiological measures?* It has been shown [36] that the performance of a human-multiagent team task will decrease with an increasingly complex spatial distribution of the agents. A decline in performance would be a natural consequence of the increase in mental computation [43] necessary to continuously estimate the kinematic state of the group. Therefore, these cognitive demands should present themselves in the α and θ band features of EEG. In addition, changes in external behaviors, such as gaze and pilot input activity, should also be present. These results would be indicative of the visual-spatial nature of the task. Moreover, changes in both cognitive activity and gaze that are associated with attention should correlate dynamically.

2.1.2 Experimental Hypotheses

The levels of geometric complexity in these experiments are embodied by two different spatial configurations of ground robots: the *serpentine* (low GC) and *rectangle* (high GC). In the remainder of this chapter, levels of GC will be referred to by the type of configuration. The objective of these human-multiagent team task was to acquire the

maximum number of randomly appearing targets in a fixed period of time. Consequently, targets acquired per minute (T_{pm}) is the metric of task performance that is employed in this study.

Our first two studies examine the differences in neurophysiological and behavioral measures grouped by the factors of configuration and task performance. These relationships, shown in Figure 2.1, are outlined in red. The dependent variables are listed in Table 2.1.

Our third study examines the dynamic relationship between cognitive processes and behaviors. Unlike the first two studies, we assume a-priori that cognitive activity and behaviors are linked through the process of attention. As mentioned in Section 2.1.1, gaze is a proxy measure for attention. Consequently, the occurrence of saccades represents shifts in top-down and/or bottom-up attention, both of which are mediated by a distributed network of brain regions [30]. The continuous changes in cognitive processes will manifest in dynamics of the topological properties of EEG functional connectivity networks. Therefore, measures associated with these topological properties and gaze behavior should correlate. These relationships are outlined in blue in Figure 2.1.

H0.5: *Task performance, measured in T_{PM}, will decrease from serpentine to rectangular configuration.* The increase in cognitive resources needed to estimate the state of the rectangular configuration will result in an increase in target misses, or a slower target-to-target transit time, both of which will ultimately result in a lower number of targets per minute.

H1: *The greater cognitive resources that are required to pilot the rectangular configuration (high GC) will present statistically significant differences in neurophysiological and behavioral measures.* More specifically, θ power in the mid and frontal regions and α power in the occipital regions of the brain should increase. In addition, long range functional connectivity in the α band would indicate top down

control of the visual attention process. These outcomes would imply an increase in visual-spatial reasoning and cognitive processing, all of which are consistent with well-established cognitive scientific literature. Furthermore, significant differences in gaze and pilot input activity should be present. The study was within-subject, and the single factor Configuration had two levels: *serpentine* (low *GC*) and *rectangle* (high *GC*).

H2: The subjects with higher performance have a natural proclivity for this particular human-robot task. Therefore, *they will utilize fewer cognitive resources than those with lower performance.* The lower cognitive demands should be reflected in the average neurophysiological and behavioral measures, as described in *Hypothesis 1.* The study was between-subject, and the single factor Performance had two levels: *high* and *low.*

H3: Cognition and gaze behavior are strongly linked during the performance of a human-multiagent task. Therefore, *a properly selected set of features derived from functional connectivity network-based metrics can distinguish between visual behaviors associated with attention.* Specifically, average values of network metrics at periods corresponding to each gaze state will differ. The magnitude of the differences will be unique to each subject, but the specific features will apply to all subjects. This study was within-subject and the single factor Gaze had two levels: *saccade* and *fixation.*

2.2 Methods

In the Present Study, we defined geometric complexity (*GC*) as the number of agents required to estimate the kinematic state of the robotic group. In order to determine the impact of *GC* on human-multiagent team performance, we conducted a series of human subject experiments based on a target identification and acquisition task, but with real ground robots and humans locally embedded in the task space. We utilized an EEG device to measure changes in both spectral power and functional connectivity in the α

and θ bands associated with cognitive activity. In addition, a pair of eye-tracking glasses measured gaze behavior.

2.2.1 Experimental Design

This experiment was conducted in the Cyber-Human-Physical Systems (CHPS) Lab at the University of California, Davis. The study consisted of a 4.2 m by 5.5 m test arena surrounded by motion tracking cameras. The test arena will be referred to as the "task space". This task space contained ground robots under the control of human subjects. Two wall mounted projectors displayed interactive targets onto the floor. We have integrated several modules into a measurement suite to record behavioral, neurophysiological, and mechanical data. Each module is named for its primary measure: 1) Gaze: a wearable eye tracking system by SensoMotoric Instruments; 2) EEG: an Emotiv Epoc headset [48] with an array of 14 electrodes positioned via the International 10-20 system; and 3) 3D Pose: an Optitrack motion capture system consisting of 12 wall mounted cameras. These modules are shown in Figure 2.2, along with one of the target-to-target trials in this chapter.

1. Gaze: a wearable eye tracking system by SensoMotoric Instruments (SMI). Data was sampled at 60 Hz. The gaze data is presented as the pixel position within a video image with a resolution of 1280 by 960 pixels.
2. EEG: an Emotiv Epoc headset is an array of 14 electrodes positioned via the International 10-20 system. Data was sampled at 128 Hz.
3. 3D Pose: a motion capturing system by Optitrack consisting of 12 cameras circumferentially positioned around the task space. The robots and eye tracking glasses were fitted with an array of reflective spheres allowing pose estimation within an accuracy of <1mm. Data was sampled at 30 Hz.
4. We have the joystick inputs from the user (v_w, ω_c). These are sampled at 30Hz and filtered with a first order Butterworth filter at a corner frequency of 3Hz.

The coordinate system established by the Optitrack module will be referred to as the "world" frame, denoted by W. In addition, each trial was recorded using an overhead
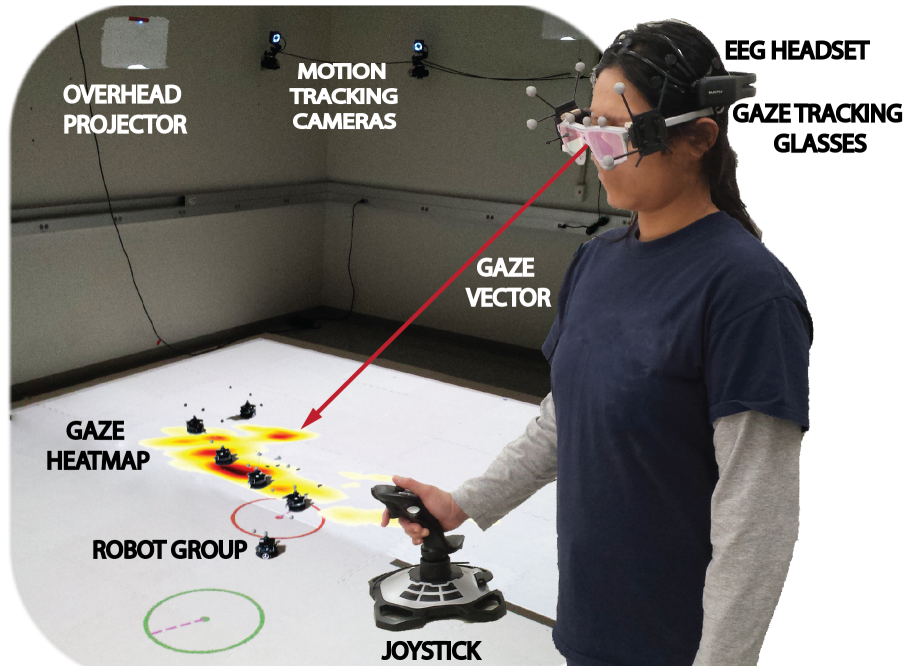
Figure 2.2: Detail of the human-robot interaction arena with motion tracking cameras and projectors, as well as a robot group, and a subject outfitted with gaze tracking glasses. START and FINISH targets are given by the green and red circles respectively. Gaze distribution in the visual field is represented as a heatmap on the floor of the task space.

camera. Several examples are shown in Figure 2.5b. Piloting commands of linear and angular velocity (v and ω respectively) from the human subjects were applied with a Logitech Force 3D Joystick. Command signals were sampled at 30Hz and smoothed with a first-order Butterworth filter at a corner frequency of 3Hz.

Our test subjects were required to pilot a group of six Pololu m3pi differential drive vehicles in each of two configurations. Only the input from a single joystick was used to pilot the group. In order to simplify control, reverse commands were not allowed. A centralized controller calculated the six independent non-interacting path-following control laws [49], with simple minimum inter-robot spacing rules to prevent collisions. Maximum speed limits ensured stability. The control signals were broadcast wirelessly to each individual robot.

The two multirobot configurations are shown in Figure 2.5a. For the serpentine configuration, the human subject piloted a lead cart while the five trailing robots would simply follow the path established by the leader. The rectangular configuration was

(a) Detail of cart kinematics used for the configuration controller.

(b) Detail of rigid body kinematics used for the configuration controller.
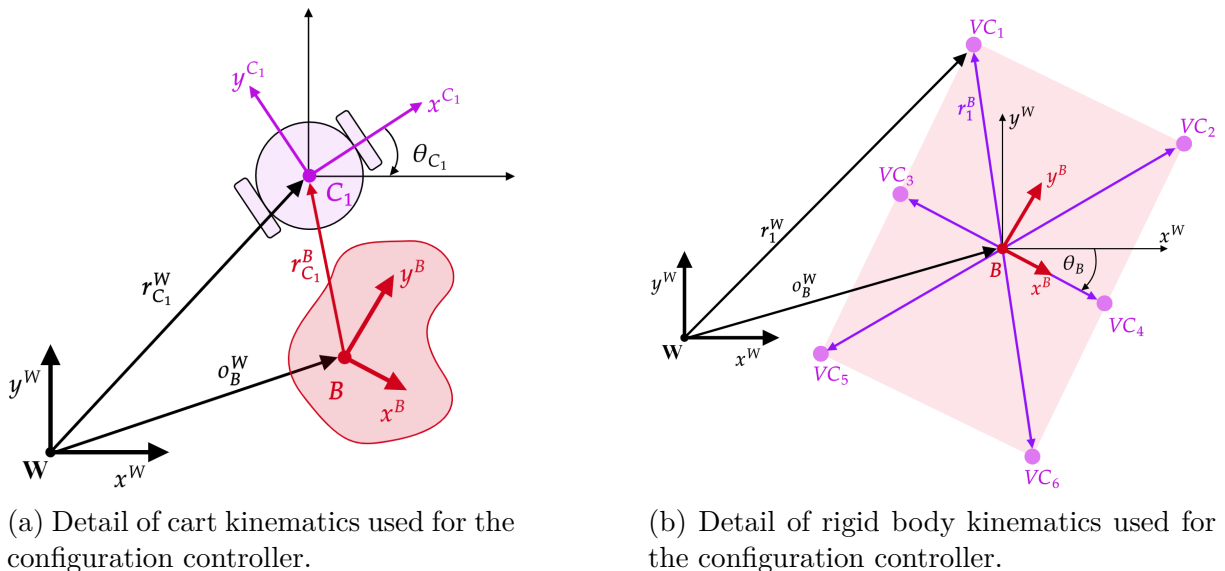
Figure 2.3: Details of the coordinate descriptions for the robotic configurations.

maneuvered by piloting the central motion of a virtual rigid body. The six unique command paths were established by the motion of virtual carts positioned about the center of a rectangular virtual shape, as seen in Figure 2.3b and Figure 2.4. The controlled motion of the rectangular configuration deviated from its perfect shape depending upon the aggressiveness of the human subject's piloting commands. Examples of the group motion are shown in Figure 2.5b. Simulations of the movement can be found at https://youtu.be/QoLUWKFrHWA and https://youtu.be/TpCnO3kb2jo. The deviation of the carts from a perfect rectangular shape is also visible in Figure 2.6.

The kinematics of the robotic group can be described mathematically by the motion of vectors in a given coordinate system. We denote the position of cart i in the world frame as r_i^W. The origin of serpentine configuration o_{srp}^W was defined by the position of the third robot in the chain: $o_{srp}^W = r_3^W$. We chose this position to distribute each subject's focus over the larger group, rather than the lead robot. In contrast, the origin of the rectangular configuration was defined as the instantaneous centroid of the six carts: $o_{rct}^W = \frac{1}{6} \sum_{i=1}^{6} r_i^W$. Piloting this group required human subjects to estimate the true position of the centroid. An example of the coordinate system for the rectangular configuration is detailed in Figure 2.3b.

13
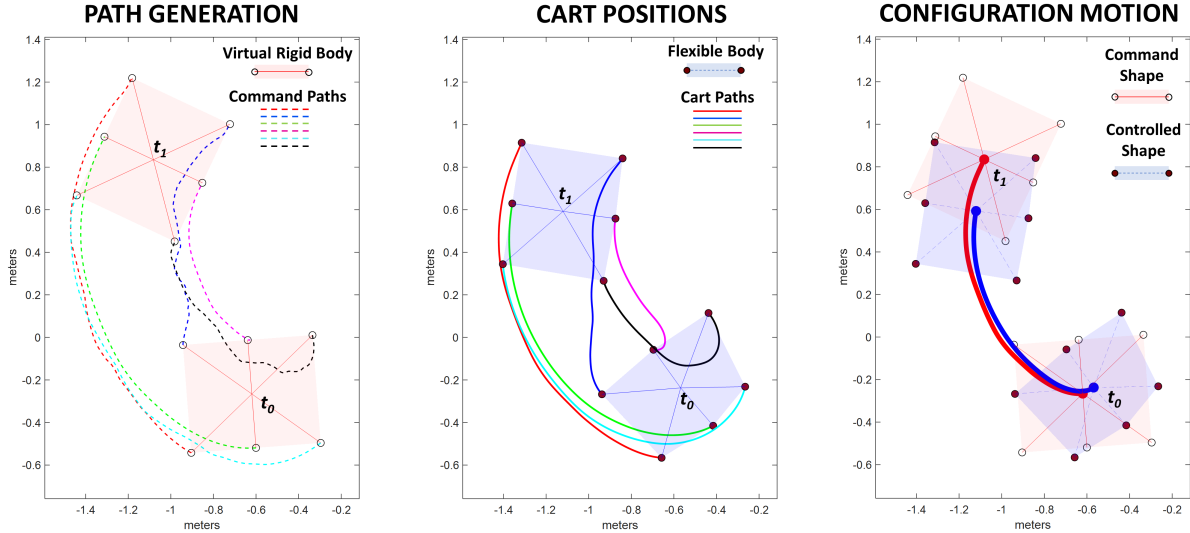
Figure 2.4: Detail of configuration controller. Command paths are determined by the control algorithm assuming carts with unicycle kinematics. The true path of the carts deviates slightly from the command causing a distortion in the shape of the controlled configuration.

Using the lead robot, a subject could effectively acquire targets with the serpentine configuration by tracking, at the very least, two robots: the lead cart; and the third cart. The rectangular configuration however, may require all six robots for adequate estimation of the origin depending on the distortion of the controlled shape as shown in Figure 2.6. Consequently, we assigned the serpentine a *GC* of 2, and the rectangle a *GC* of 6. Regardless of how aggressively the subject attempts to pilot the rectangular configuration, we expect it to be more difficult to perform the task effectively than the serpentine configuration.

2.2.2 Participants

Ten subjects completed the tests; 9 male and 1 female. All subjects were undergraduate students between the ages of 18 to 22. Each subject was instructed on both the testing procedure and proper use of the test equipment. In addition, there were two training sessions in which subjects would control first a single robot, then all six robots in each configuration as shown in Figure 2.7. We demonstrated for them how to acquire the target using each configuration. For all subjects, the test series proceeded as follows: training to the serpentine trials; and finally to the rectangular trials.
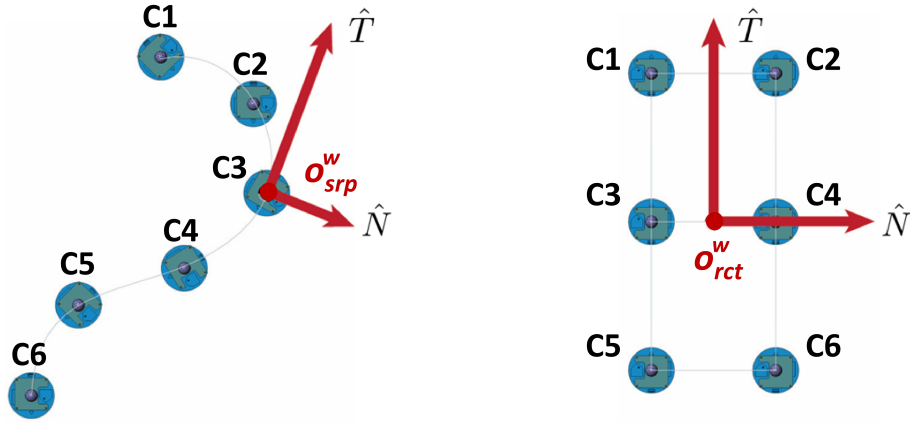
(a) The Serpentine and Rectangle configurations used in this study.
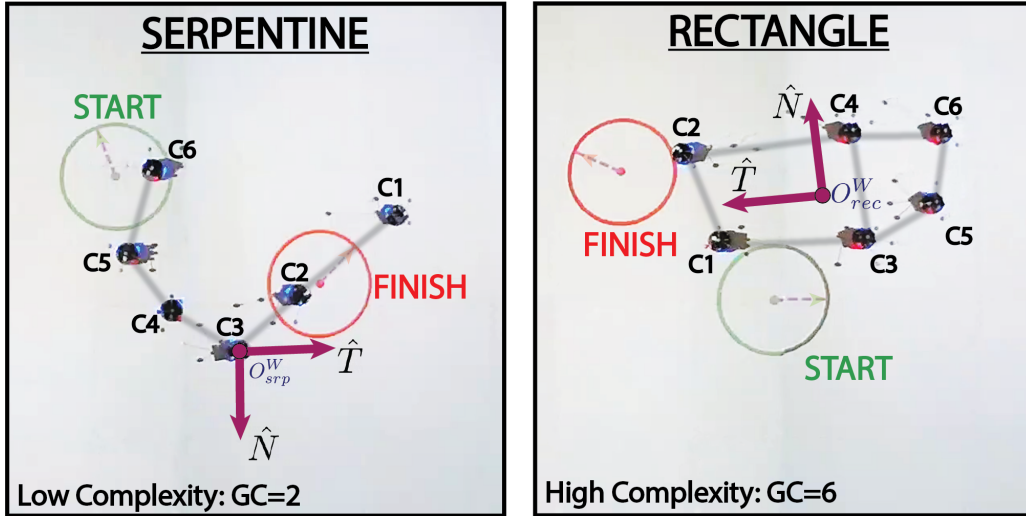
(b) Overhead screen captures of a single target attempt for the two multirobot configurations used in this study. The tangential $\hat{T}$ and normal $\hat{N}$ directions of the body frame for each configuration are labeled. The origin for the serpentine configuration O_{srp}^{W} is defined by position of the third robot in the chain, whereas the origin of the rectangular configuration O_{rct}^{W} is defined by its centroid. Both the position and heading information of the target are displayed. A subject must pilot the configuration of robots from an initial target (START) to a final target (FINISH). The distortion of the rectangular configuration is evident.

2.2.3 Task Design

During each trial, subjects were presented with targets projected onto the floor. The first target of each trial was located in the direct center of the task space. All subsequent targets were selected from predetermined sequences. Subjects had no a-priori knowledge of the sequences and consequently, target generation was random from their perspective.

NON-AGGRESSIVE MANEUVER

AGGRESSIVE MANEUVER
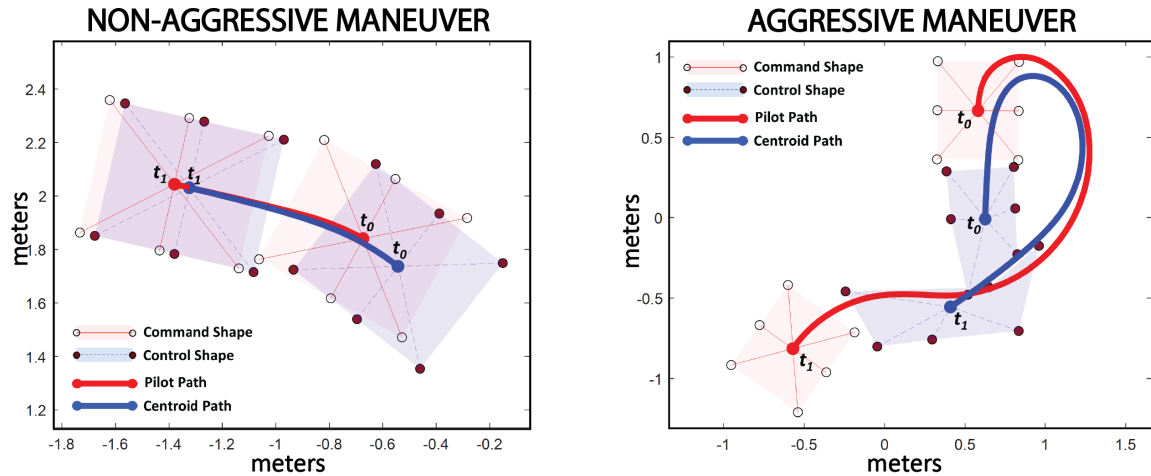
Figure 2.6: A detail of configuration distortion due to the aggressiveness of the control input. An aggressive maneuver is combination of high speed and short turn radius that will cause the robot group, shown in blue, to deviate significantly from its rigid body shape, in red. A slower and straighter non-aggressive maneuver yields little deviation from the perfect rigid body.

SERPENTINE TRAINING SESSION

RECTANGLE TRAINING SESSION
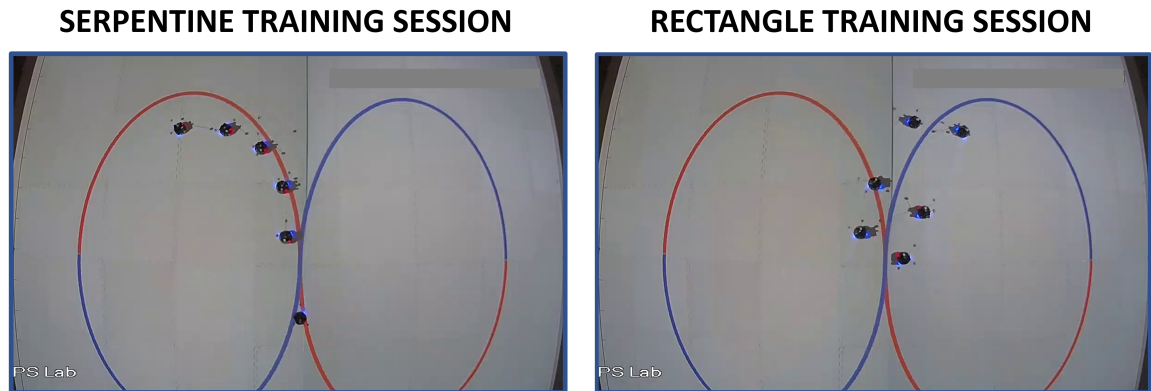
Figure 2.7: Overhead view of the training sessions for each configuration. Subjects were instructed to pilot the configurations around the figure-eight path while attempting to keep the centroid of the configuration on the path.

Each target contained heading information indicated by a line. Subjects were tasked to pilot the origin of each robotic group from one target to the next as quickly as possible. New targets were only revealed when both a minimum origin-to-target distance of 15.2 cm (6 in) and a minimum heading difference of $\pm 15°$ were met. Therefore, only two targets, a start and a finish, were visible to the subjects at any time. A detail of a target pair is shown in Figure 2.6. All target-to-target paths were designed to be feasible given the spatial constraints of the task space. Subjects were provided eight minutes to pilot each

configuration with the explicit task of acquiring as many targets as possible. Depending on the skill of the human subject, the number of targets acquired ranged from 4 to 12. There was a five minute rest phase between each trial.
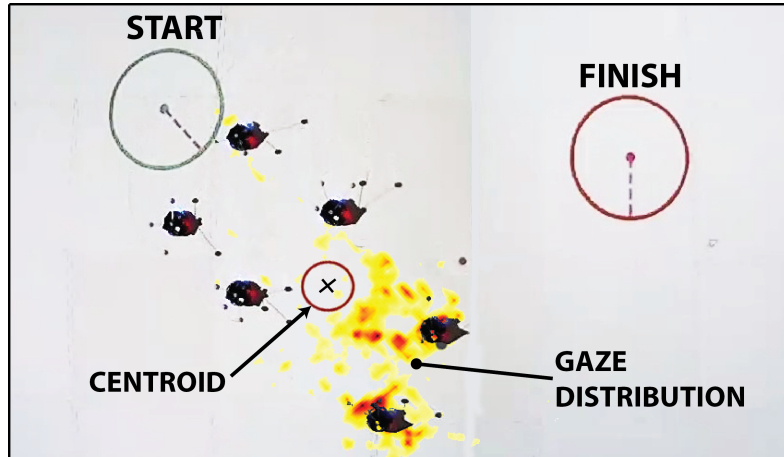
Figure 2.8: An overhead screen capture of a single target attempt. A rectangular configuration of robots is being guided from the initial target (START) to the final target (FINISH). The gaze distribution, indicated by a heat map, is noticeably leading the true centroid

2.3 Measures

In this section we discuss the methods used to prepare our data. The complete set of measures presented in this chapter is summarized in Table 2.1. For each target attempt, we examined the arrival phase: the final eight second period during which a subject attempts the acquisition of a target. It is during this phase when fine piloting corrections and visual activity, i.e., motor and sensory processes, would be collectively deployed to successfully acquire the target. The maintenance of sensory information stored withing working memory requires constant control through the attentional system [50]. Therefore, access to working memory resources, and the sensory inhibition of non-relevant stimuli should be greatest during the acquisition phase. We did not discriminate between successful and an unsuccessful target acquisition. The subjects are generally unaware of their outcome until after the configuration has passed over the target point. Therefore, regardless of success or failure, each subject intends to succeed and behaves in a manner to do so.

Three primary pipelines were established to generate the measures for our analyses: 1) extraction of the gaze data shown in Figure 2.9A; 2) determination of the joystick activity shown in Figure 2.9B; and 3) extraction of the EEG spectral powers and dynamic functional connectivity shown in Figure 2.9C. Data streams were pruned to the 8 seconds preceding the acquisition of each target, filtered, and temporally aligned for comparison.

Table 2.1: Detail of the Dependent Variables for Hypotheses I and II

Measure	Description
Spatial Gaze Distribution: G_M	Gaze distribution in the *Middle* region of the robotic configuration.
Joystick Activity: J_A	Cumulative sum of incremental joystick movement.
EEG Power: $\hat{P}_\alpha, \hat{P}_\theta$	Normalized spectral power in the α and θ bands.
Broadband Functional Connectivity: $C_\alpha^{ij}, C_\theta^{ij}$	Phase synchrony between channels i and j in the α and θ bands.

2.3.1 Gaze Data

2.3.1.1 Rotation to the Body Frame

The Optitrack motion capture system establishes a world frame W within the task space. A pose estimate of the subject's head was combined with the gaze, extracted from the eye tracking glasses (ETG), to synthesize the gaze vector in W as r_g^W. The intersection of this gaze vector with the arena floor created a heatmap of the overall distribution of gaze points, as shown in Figure 2.10.

All data were transformed into a body centered coordinate system B, determined for each configuration. In doing so, we performed an analysis independent from the specific pose of the robotic group. The system B was defined as follows: first, extract the unit vector $\hat{T}$, originating from the rigid body origin o_c^W and tangential to the direction of movement. Next, project a unit vector $\hat{N}$ perpendicular to $\hat{T}$. Finally, translate by o_c^W and multiply by the rotation matrix R_W^B from the world frame W to the body frame B to obtain $r_g^B = R_W^B(r_g^W - o_c^W)$, where r_g^B is the gaze in the body frame. We transformed the cart positions, target positions, and the gaze distributions into the new body frame B. An example of these transformations for a single target attempt is shown in Figure
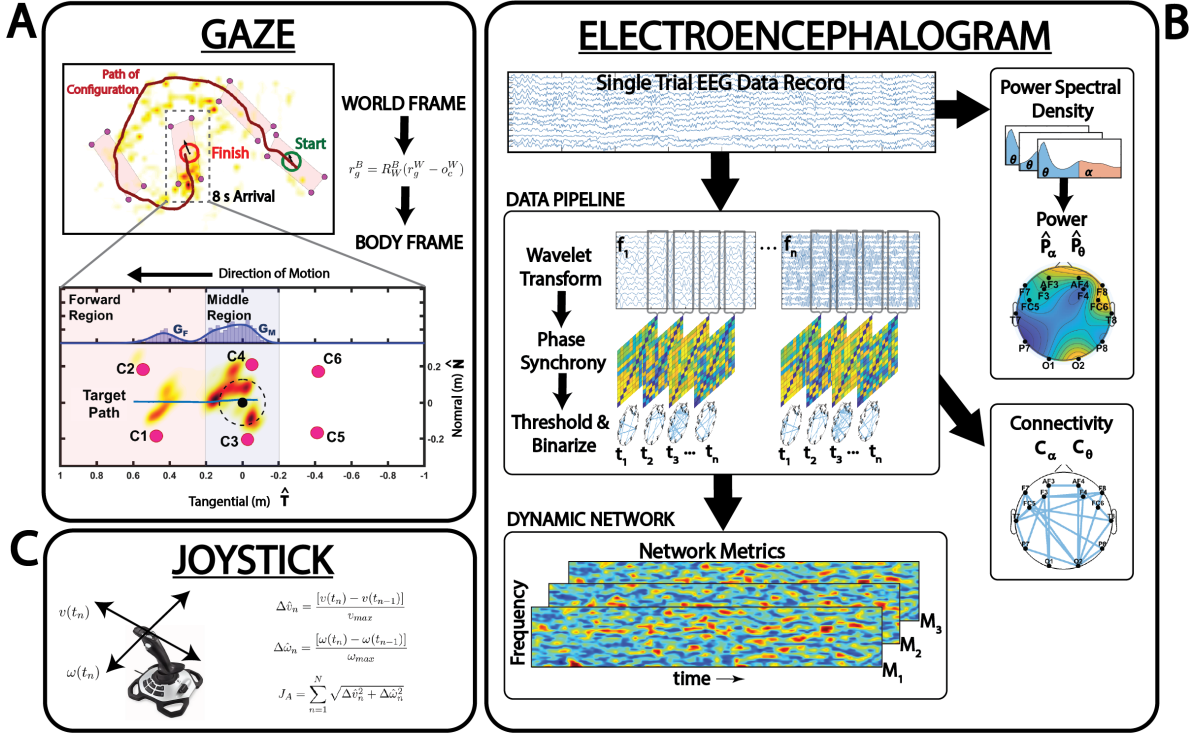
Figure 2.9: A detail of the data reduction methods used to obtain our measures. The detail of gaze data reduction, including the rotation into the moving body frame, is shown in (A). Gaze data, shown as a heat map, are projected onto the arena floor. The gaze regions and their associated histograms are delimited by vertical lines. Average cart positions are marked as $C1$ through $C6$. The group origin (centroid) along with the 30.5 cm diameter threshold region is shown by a black dot and circle, respectively. Note the deviation of the cart positions from a true rectangular distribution. The methods for obtaining the spectral data, connectivities, and temporal metrics are outlined in (B). Each 8 second EEG time trace is transformed via complex morlet wavelets. Connectivity matrices derived from the phase synchrony calculated over a sliding window are used to generate the temporal sequence of EEG networks. Network metrics determined at each time step trace out the evolution of network properties. The methods to extract joystick activity are shown in (C). Joystick activity is defined as the cumulative sum of incremental changes in normalized linear and angular joystick commands.

2.9A.

2.3.1.2 Estimating Gaze Distributions

The wider dispersion of carts in the rectangular configuration naturally induces increased gaze activity in the direction of $\hat{N}$. We examined differences in gaze distributions along the $\hat{T}$ direction. One area was selected for comparison: the *Middle* region denoted by M and defined between ± 20.3 cm from the centroid.
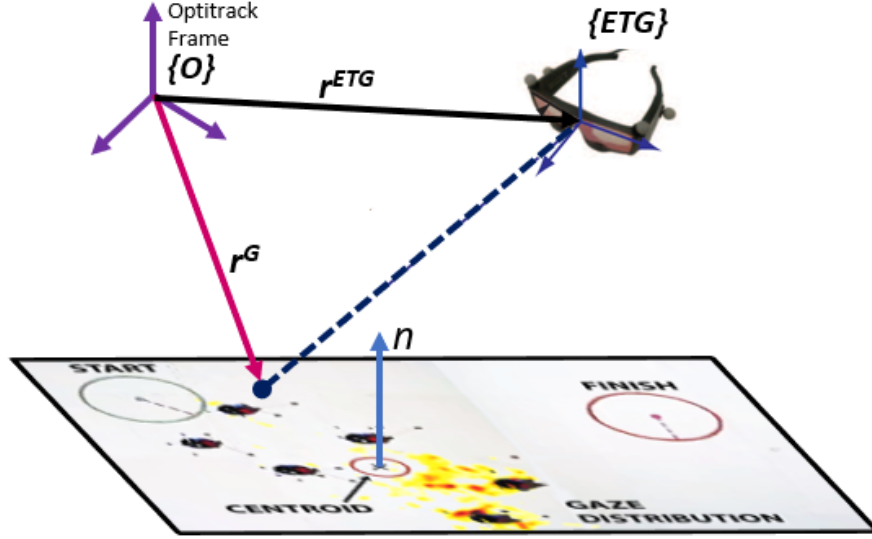
Figure 2.10: Detail of gaze projection onto the floor. The gaze vector from the ETG device is extrapolated onto the floor of the task space.

The sample probability of gaze within a given region was determined as the sum of all gaze points r_g^B falling in the middle region M divided by the N total gaze samples contained in each 8 s target period. We denote the estimate of this probability as

$$G_M = \frac{1}{N} \sum_M r_g^B$$

where $N{=}240$ for a 30 Hz sample rate. One such distribution is also illustrated in Figure 2.9A.

2.3.2 Joystick Activity

We defined a measure of *joystick activity* (J_A) for each 8 second acquisition period. The J_A is a unitless quantity meant to capture the amount of pilot input from each subject as the cumulative sum of incremental changes in normalized joystick commands for the linear

$$\Delta \hat{v}_n = \frac{v(t_n) - v(t_{n-1})}{v_{max}}$$

and angular

$$\Delta \hat{\omega}_n = \frac{\omega(t_n) - \omega(t_{n-1})}{\omega_{max}}$$

velocities,

$$J_A = \sum_{n=1}^{N} \sqrt{\Delta \hat{v}_n^2 + \Delta \hat{\omega}_n^2}$$

where again N=240. A greater value of J_A implies a larger amount of differential control inputs as the subjects attempt speed/slow or steer the robotic group.

2.3.3 EEG Spectral Power

EEG data were filtered with a zero lag 4th-order bandpass filter (2-36Hz). Electromyographic artifacts arising from blinks and lateral eye movements were identified via an independent component analysis (ICA) [51] using the FastICA algorithm [52]. No more than two ICA artifacts were removed from any data set. The 14 channel EEG data was reconstructed from the remaining independent components.

Power spectral densities (PSD) of each reconstructed channel i were calculated over the 8 s target period using a fast Fourier transform. The specific band powers (in units of μV^2) were determined by numeric integration of the PSD over the frequencies in the θ (4-8Hz) and α (8-12Hz) band. The powers were then normalized using baseline data by

$$\hat{P}_\alpha^i = \frac{B_\alpha^i - P_\alpha^i}{B_\alpha^i}$$

and

$$\hat{P}_\theta^i = \frac{P_\theta^i}{B_\theta^i}$$

where B_θ^i and B_α^i were obtained from the human subject at the start of each test [17].

The full set of EEG data were arranged into a matrix $X \in \mathbb{R}^{14 \times 176}$ for the 176 target observations accumulated by all 10 subjects. The percent of channels that were linearly correlated ($r > 0.5$) was 11% and 45% in the θ and α bands respectively. We removed linear interrelationships by rotating the data into a coordinate frame of principal components determined via diagonaliztion of the covariance matrix: $\Sigma = (X - \bar{X})(X - \bar{X})^T$. The 14 unit eigenvectors w_i of Σ formed a basis set for the spatial distribution of spectral power. These principal components were arranged to form the columns of an orthonormal matrix $W \in \mathbb{R}^{14 \times 14}$. Multiplying the mean centered EEG data by W produced a new, nearly uncorrelated ($r < 10^{-15}$) data set K, expressed as $K = W(X - \bar{X})$.

Our statistical testing proceeded on the data K. By enumerating the total set of principal components as $\mathcal{W} = \{1, 2, \cdots, 14\}$ and the subset of K whose differences were statistically significant be given as $\mathcal{A} \subseteq \mathcal{W}$, we reconstructed differences in the spatial distribution of power X^{B-A} between the factors A and B as $X^{B-A} = \sum_{i \in \mathcal{A}} w_i(\bar{k}_i^B - \bar{k}_i^A)$, where w_i is the principal component, and $\bar{k}_i$ is the average value of k_i extracted from the statistical test. Only components with $p < 0.05$ were selected for comparison.

2.3.4 EEG Functional Connectivity

A wide array of functional connectivity measures are commonly use in EEG analysis [53]. However, frequency specific phase locking is readily captured using phase synchrony (PS) [54]. In the remainder of this chapter, references to connectivity between channels specifically refers to the PS values between them. The determination of inter-channel PS values is outlined in Figure 2.9B. First, we pruned and filtered the data as described earlier. Using a surface Laplacian [16], we transformed the data to current source density in $\mu V/m^2$. Next, we performed a time-frequency decomposition via convolution with complex Morlet wavelets to separate the data into 32 discrete frequency bands. Finally, we calculated the PS value between all channels i and j over moving windows of 250 ms in duration and 7.8 ms in step size

Connectivity in the α and θ bands (C_α, C_θ) were selected from discrete frequencies in time-frequency decomposition. These values corresponded to the central frequency of each band: 6Hz for the θ band, and 10Hz for the α band. Synchronization between brain regions is indicated by PS values close to unity [55]. Consequently, PS values below a threshold of 0.80 were disregarded.

2.3.5 Dynamic Networks

The functional connectivity between EEG channels (AF3, F3, FC5, F7, T7, P7, O1, O2, P8, T8, F8, FC6, F4, AF4) can be represented by a fully connected undirected weighted graph possessing an adjacency matrix $A \in \mathbb{R}^{14 \times 14}$, where A_{ij} is the PS value between nodes i and j. We can define such graphs from the sequence of PS values. The resulting temporal sequence of graphs captures the dynamic changes in functional connectivity as

the task evolves.

We used network metrics [56] to quantify the global topological attributes of functional connectivity. The six metrics used in this study are listed in Table 2.2. Before a calculation of each metric, all graphs were reduced to binary unweighted representations by thresholding the PS values above 0.92. As shown in Figure 2.9, the six metrics were calculated at each of the 32 frequencies in the time-frequency decomposition yielding a set of 224 elements.

2.3.5.1 Dynamic Network-Based Features

The temporal features used to discriminate gaze behaviors were defined as the average value of the network metrics over a period of 250 ms. Therefore, the temporal sequence of features values were determined by the moving average of the network-based-metrics over a 250 ms window.

Table 2.2: Detail of Network Metrics

Metric	Description
Transitivity	The degree to which adjacent nodes are commonly connected to a third node, revealing the existence of tightly connected communities.
Efficiency	The average inverse shortest path length between any two nodes in the network.
Density	Proportion of total possible edges in the network
Modularity	The degree to which network nodes can be segregated into non-overlapping groups (modules) of dense within-group connections separated by sparse between-group connections.
Maximum Degree	Largest degree of any node in the network.
Component Count	Number of disconnected components in the network.

2.4 Statistical Analysis

We performed all statistical tests on the dependent variables outlined in Table 2.1. If the data passed a one sample Kolmogorov-Smirnov test, a normality assumption was used and the analysis proceeded with a single factor analysis of variance (ANOVA). The spectral power and joystick activity data were approximately normally distributed. In general, both gaze and connectivity distributions were highly skewed and a non-parametric

Kruskal-Wallis H tests were used for these data. Distributions shapes are illustrated in Figure 2.12 and Figure 2.13. The skewness of the distributions are clear from inspection. For tests that reached a significance of $p < 0.05$, we performed post-hoc paired t-tests with Bonferroni correction to estimate the differences in the means.

2.4.1 H0.5 Analysis

Our statistical tests for Hypothesis 0.5 group the performance data by the between-subject factor of geometric configuration (GC). In total, there were 99 targets acquired for the serpentine configuration and 78 targets acquired for the rectangular configuration for a total of 177 targets in the data set.

2.4.2 H1 and H2 Analysis

Our statistical tests for Hypothesis 1 group the data by the within-subject factor of Configuration with levels of *serpentine* and *rectangle*. The statistical tests for Hypothesis 2 group the data by between-subject factor of Performance with levels of *high* and *low*. High and low performance values were selected based on the average number of targets per minute between both configurations as derived from our previous work [36]. A threshold value of 1.1 targets per minute effectively divided the population into two groups of five higher, and five lower performing subjects. In total, there were 99 targets acquired for the serpentine configuration and 78 targets acquired for the rectangular configuration for a total of 177 targets in the data set. This quantity was divided between high and low performers with 93 targets acquired by high performers and 84 acquired by low performers.

2.4.3 H3 Analysis

The goal of Hypothesis 3 was to find the minimum set of EEG network-based features that will discriminate between gaze states under all conditions in this experiment. Due to the substantial number of eye blinks exhibited by one of our subjects, it became extremely difficult to sort saccades from blink data. Consequently, the data for this subject was removed in the H3 analysis, reducing the final number of subjects from 10 to 9. Assuming the different configurations elicit different gaze behaviors, the number of separate conditions is given by the 9 subjects and 2 configurations for a total of 18. The

set of 224 features used for this analysis are described in the section on Dynamic Networks. Therefore, a set of 4,032 statistical tests were performed using the within-subject factor of Gaze with two levels of *fixation* and *saccade.*

Feature values were the average of network-based metrics over a 250 ms window. The values for *saccade* were taken over the 250 ms directly preceding each saccade while the values for *fixation* were taken at the mid point between two saccades. The number of saccades varied for each condition (M=28, SD=7.45). However, the number of saccades and fixations were always equal for any given condition.

2.5   Results and Discussion

The tests for all subjects proceeded as follows: from training; to the serpentine trials; and finally the rectangular trials. If any transferable learning occurred, it would have been from the serpentine to the rectangular configuration. The training phase was designed to provide the subjects with ample experience piloting both configurations. We note that the absence of counterbalance may be a potential confound that can limit an interpretation of the results.

In the H1 and H2 analysis that follows, we have chosen to investigate the qualities of EEG power and connectivity that have been well established in the literature, namely attention, sensory selection, and working memory access. The Emotiv headset only allows primary observation of the left and right frontal regions with only two temporal channels (T7 and T8), two temporal channels (P7 and P8), and two occipital channels (O1 and O2). EEG locations in the parietal cortex associated with motor control, or decision making are outside of our range of observation. Furthermore, the role of θ connectivity is still debated in the literature. We report the θ connectivity results, but do not attempt to analyze them.

2.5.1   Data Presentation

The results for *H1* and *H2* are shown in Figure 2.12 and Figure 2.13 respectively. The power and connectivity results for the α and θ bandwidths are detailed in the subfigures *A* and *B*. Raw data are given in the top panels while the estimated differences in the means

are shown in the bottom panels. All error bars represent the 95% confidence interval on the means.

The bar plots of differences in group mean normalized power have been split into regions representing the left-frontal (LF), right-frontal (RF), and temporal-parietal-occipital (T-P-O) regions of the head. As mentioned in the section on EEG Spectral Power, differences in normalized power are reconstructed from significant values of the data derived from the principal component transformation. Head-maps illustrate the spatial distribution of the normalized power data presented in the bar plots.

Channel pairs with significant differences in mean connectivity are also illustrated with bar plots. Head-maps are used to detail the inter-channel connections: red lines indicate increases in connectivity values while blue lines indicate decreases. In addition, regions on the head maps are similarly separated between the frontal (both LF and RF) and T-P-O using colored areas.

The behavioral data are shown in subfigure *C*. Raw behavioral data are given in the horizontal distribution plots while the differences in group means are illustrated with bar plots.

2.5.2 Hypothesis 0.5: Impact of Geometric Complexity on Performance

This section presents the statistical test results between the two levels of the between-subject factor of Configuration. The significant differences in group means are given by the factor *rectangle(Rec)* minus the factor *serpentine(Srp)*: $\Delta = Rec\text{-}Srp$. The results are illustrated in Figure 2.11.

Table 2.3: H 0.5: t-test for Equality of Means

	t	*df*	*p (2-tailed)*	$\Delta Mean$	95% CI Lower	95% CI Upper
Targets Per Minute	4.624	8	0.0017	0.634	0.138	0.950
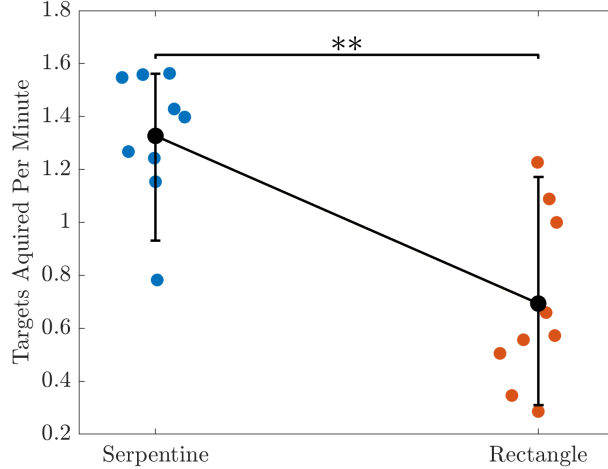
Figure 2.11: Comparing targets acquired per minute (T_{pm}) between the Rectangular and Serpentine configurations. **$p < 0.002$.

2.5.2.1 Discussion

Our results show that *GC* is statistically different for all subjects in this study. The remainder of the results rely on the conclusions from H 0.5: that the *GC* impacts performance and may therefore be used as a factor in and of itself.

2.5.3 Hypothesis 1: Impact of Geometric Complexity on Neurophysiological and Behavioral Measures

This section presents the statistical test results between the two levels of the within-subject factor of Configuration. The significant differences in group means are given by the factor *rectangle(Rec)* minus the factor *serpentine(Srp)*: $\Delta = Rec\text{-}Srp$. The results are illustrated in Figure 2.12. Details of the statistical test results including values of F, χ^2, and p values are given in Table D.1 through Table D.4 in Appendix D.1.

2.5.3.1 Spectral Power

Mean $\hat{P}_\alpha$ are given in Table 2.4 and the statistically significant differences presented in Figure 2.12A are given in the third row of the table. The greatest positive and negative changes of $\hat{P}_\alpha$ occur in the LF region. However, of the 8 channels in the frontal region (LF and RF combined) only two show decreases in power. More notably, there are increases in power in the T-P-O region at channels P7, O1, O2, and P8, ranging from 0.59% to 1.12% with only T7 and T8 showing decreases.

27

Table 2.4: Mean $\hat{P}_\alpha$ for the Factor Configuration

Channel / Factor	LF				T-P-O						RF			
	AF3	F7	F3	FC5	T7	P7	O1	O2	P8	T8	FC6	F4	F8	AF4
Rectangle	0.644	0.733	0.701	0.755	0.614	0.683	0.716	0.713	0.676	0.640	0.668	0.719	0.677	0.697
Serpentine	0.679	0.681	0.700	0.723	0.635	0.675	0.712	0.692	0.669	0.645	0.664	0.717	0.692	0.693
%Δ(Rec-Srp)	-5.29	7.73	0.11	4.40	-3.36	1.12	0.59	3.12	1.12	-0.77	0.61	0.30	-2.14	0.47

Mean $\hat{P}_\theta$ are given in Table 2.5 and the statistically significant differences presented in Figure 2.12B are given in the third row of the table. Of the 8 channels in the frontal regions, 7 show increases in $\hat{P}_\theta$ ranging from 4.72% to 34.72%. The single decrease in frontal power occurs at AF4. The differences in the T-P-O region are mostly positive with decreases occurring at T7 and O1.

Table 2.5: Mean $\hat{P}_\theta$ for the Factor Configuration

Channel / Factor	LF				T-P-O						RF			
	AF3	F7	F3	FC5	T7	P7	O1	O2	P8	T8	FC6	F4	F8	AF4
Rectangle	4.295	4.932	4.633	4.010	3.163	3.070	3.047	5.519	5.367	6.319	5.757	5.521	7.609	4.776
Serpentine	4.101	4.641	4.210	3.442	3.377	2.873	3.592	4.925	4.877	6.134	5.174	4.098	6.737	5.018
%Δ (Rec-Srp)	4.72	6.27	10.03	16.50	-6.34	6.85	-15.17	12.07	10.05	3.01	11.28	34.72	12.94	-4.83

2.5.3.2   Connectivity

Statistically significant differences in C_α are shown in Figure 2.12A while those in C_θ are shown in Figure 2.12B. Percent values indicate the percent change in connectivity from the rectangluar to the serpentine configurations. Positive differences in functional connectivity indicate greater levels of phase synchrony when subjects pilot the rectangular configuration while negative differences indicate greater phase synchrony when subjects pilot the serpentine configuration.

There are 13 significant differences in the α band. The 12 positive differences range from 0.667% to 1.04% while the single negative difference is -0.481%. Seven of these connections are between the T-P-O and frontal regions including two from O1 (O1-F3 and O1-FC5). The remaining six connections are within the frontal region with the single negative value occurring from F4-F8.

There are 11 significant differences in the θ band. Ten of these differences are positive

and one negative. The 10 positive differences range from 0.726% to 1.04% while the single negative difference is -0.507%. Six of these connections are between the T-P-O and frontal regions while the remaining 4 are located within the frontal region. The single negative connection occurs from FC6-F8.

2.5.3.3 Behavioral Characteristics

In Figure 2.12C. There is a significant effect at the $p < .05$ level of the configuration on the joystick activity $[F(1, 176)=29.86, p=1.54 \times 10^{-7}]$ between Rec (M=3.84, SD=1.79) and Srp (M=5.06, SD=1.20), or a 24.1% decrease in joystick activity from Srp to Rec. There is also a significant effect at the $p < .05$ level of the configuration on the gaze in the middle region $[\chi^2=34.11, p=5.20 \times 10^{-9}]$ between Rec (M=0.109, Q1=0.050, Q3=0.212) and Srp (M=0.035, Q1=0.008, Q3=0.083), or a 211% increase in middle region gaze from Srp to Rec.

2.5.3.4 Discussion

Examining the differences, we see that piloting the rectangular configuration produced several key results. Greater $\hat{P}_\theta$ in the frontal region indicates more access to working memory resources [21]. Furthermore, the greater $\hat{P}_\alpha$ in the occipital region is associated with the suppression of task irrelevant visual stimuli [57]. Additionally, the increase in C_α between the occipital and frontal regions, specifically O1-F3 and O1-FC5, is also indicative of top-down suppression of visual stimuli. This C_α may further imply a greater focus on internal cognitive processes due to suppression of visual stimuli [30]. Finally, subjects piloting the rectangular configuration spend more time looking in the middle region, yet they utilize less pilot input.

We can obtain insight into these results by comparing the methods for piloting the configurations. Each subject controls the serpentine configuration by piloting only the lead cart; the remaining robots follow the path established by the leader. Both the reduction of gaze in the middle region and the greater amount of joystick activity are behaviors that result from the confident and predictably deterministic control of the single lead robot. In contrast, subjects maneuver the rectangular configuration by piloting the collective motion of a virtual rigid body. Rather than a single cart, each subject must comprehend
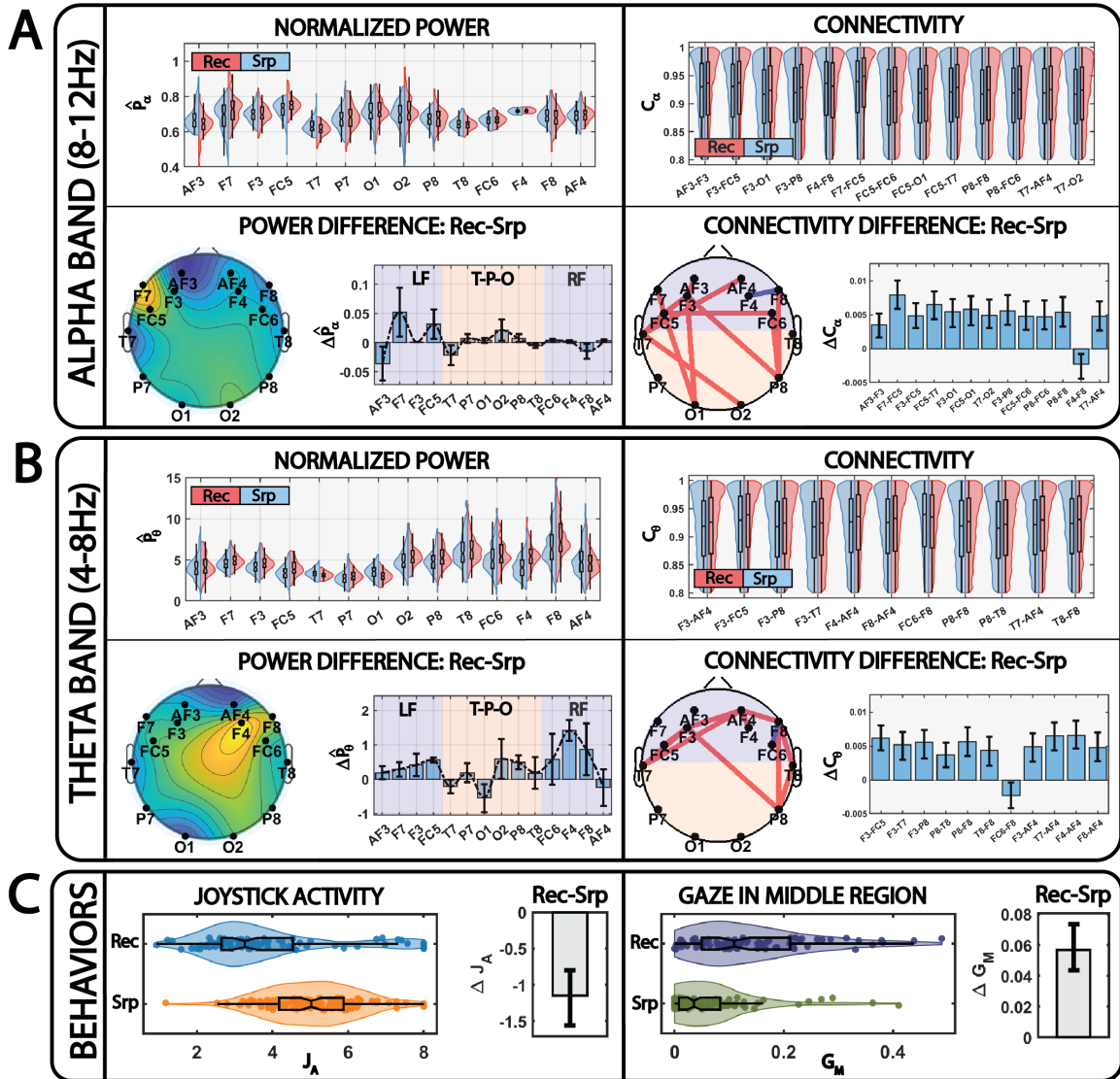
Figure 2.12: A comparison of the neurophysiological and behavioral differences associated with the factor configuration. Power and connectivity in the α band are presented in (A) while those in the θ band in (B). The serpentine configuration is labeled as *Srp* and the rectangular configuration as *Rec*. Raw data are illustrated with violin plots while the statistically significant differences are detailed in the bar plots. Behavioral results are shown in (C).

and predict the relatively fluid motion of all six robots at once. A determination of the centroid requires constant visual estimation. The focused attention that is necessary results in larger amount of gaze in the middle region, and the utilization of more working memory resources. Additionally, the indirect interface may also explain the reduction in control activity, since the subject's internal map, from pilot input to configuration

motion, requires a greater amount of mental computation to establish a similar degree of confidence. However, there is also the possibility that gross positioning of the robotic group may have already occurred and that little positional fine tuning was necessary. Regardless, the suppression of visual stimuli indicates a larger focus on internal cognitive processes. From a cognitive perspective, there is simply more internal processing required to pilot the rectangular configuration. The outcomes are generally slower speeds and more missed targets. These results are directly consistent with *Hypothesis 1*.

2.5.4 Hypothesis 2: Characteristics of High/Low Performers

This section presents the statistical test results between the two levels of the between-subject factor of Performance. The significant differences in group means are given by the factor *high(Hi)* minus the factor *low(Lo)*: ($\Delta = Hi\text{-}Lo$). The results are illustrated in Figure 2.13. Details of the statistical test results including values of F, χ^2, and p values are given in Table D.5 through Table D.8 in Appendix D.2.

2.5.4.1 Spectral Power

Mean $\hat{P}_\alpha$ are given in Table 2.6 and the statistically significant differences presented in Figure 2.13A are given in the third row of the table. Changes in $\hat{P}_\alpha$ in the frontal region are mostly positive with only AF3, F3, and F8 showing decreases. In the T-P-O region, channels P7, O1, O2, and P8 shown positive changes ranging from 1.43% to 5.10% with decreases occurring at T7 and T8.

Table 2.6: Mean $\hat{P}_\alpha$ for the Factor Performance

Channel / Factor	LF				T-P-O						RF			
	AF3	F7	F3	FC5	T7	P7	O1	O2	P8	T8	FC6	F4	F8	AF4
Hi	0.647	0.711	0.682	0.738	0.622	0.695	0.719	0.710	0.678	0.626	0.674	0.731	0.683	0.708
Lo	0.681	0.696	0.721	0.736	0.630	0.661	0.708	0.692	0.665	0.660	0.657	0.705	0.689	0.681
%Δ (Hi-Lo)	-5.03	2.06	-5.39	0.25	-1.35	5.10	1.43	2.55	1.97	-5.18	2.55	3.71	-0.89	3.92

Mean $\hat{P}_\theta$ are given in Table 2.7 and the statistically significant differences presented in Figure 2.13B are given in the third row of the table. All channels in the frontal region show increases in $\hat{P}_\theta$ from 1.66% to 18.73%. Three of the 6 channels in the T-P-O region show decreases in power at T7 and P7.

Table 2.7: Mean $\hat{P}_\theta$ for the Factor Performance

Factor \ Channel	LF				T-P-O						RF			
	AF3	F7	F3	FC5	T7	P7	O1	O2	P8	T8	FC6	F4	F8	AF4
Hi	4.504	4.916	4.624	3.885	3.273	2.827	3.488	5.681	5.184	6.528	5.872	4.759	7.584	5.239
Lo	3.838	4.608	4.145	3.479	3.295	3.104	3.206	4.643	4.991	5.873	4.946	4.681	6.610	4.554
%Δ (Hi-Lo)	17.34	6.69	11.57	11.66	-0.68	-8.93	8.81	22.35	3.86	11.16	18.73	1.66	14.75	15.05

2.5.4.2 Connectivity

Statistically significant differences in C_α are shown in Figure 2.13A while those in C_θ are shown in Figure 2.13B. Percent values indicate the percent change in connectivity from high performers to low performers. Positive differences in functional connectivity indicate greater levels of phase synchrony in higher performing subjects while negative differences indicate greater synchrony in lower performing subjects.

There are 8 significant differences in the α band. The 7 positive differences range from 0.630% to 1.32% while the single negative difference is -0.729%. Five of these connections are between the T-P-O and frontal regions with two occuring from O1-F4 and O2-FC6. The remaining three are located within the frontal regions with the single negative connection from F8-T6.

There are 7 significant differences in the θ band. The 6 negative differences range from -1.19% to -0.691% while the single positive difference is 0.892%. Five of these connections are between the T-P-O and frontal region while the remaining three are located within the frontal region. The single positive connection is from FC6-F8.

2.5.4.3 Behavioral Characteristics

In Figure 2.13C. There is a significant effect at the $p < .05$ level of the performance on the joystick activity [$F(1, 176)$=37.16, p=6.52 $\times$ 10^{-9}] between *Hi* (M=5.15, SD=1.52) and *Lo* (M=3.82, SD=1.40), or a 34.8% increase in joystick activity from low performers to high performers. In addition, there is a significant effect at the $p < .05$ level of the performance on the gaze in the middle region [χ^2=4.38, p=0.036] between *Hi* (M=0.075, Q1=0.021, Q3=0.160) and *Lo* (M=0.058, Q1=0.013, Q3=0.100), or a 29.3% increase in middle region gaze from low performers to high performers.
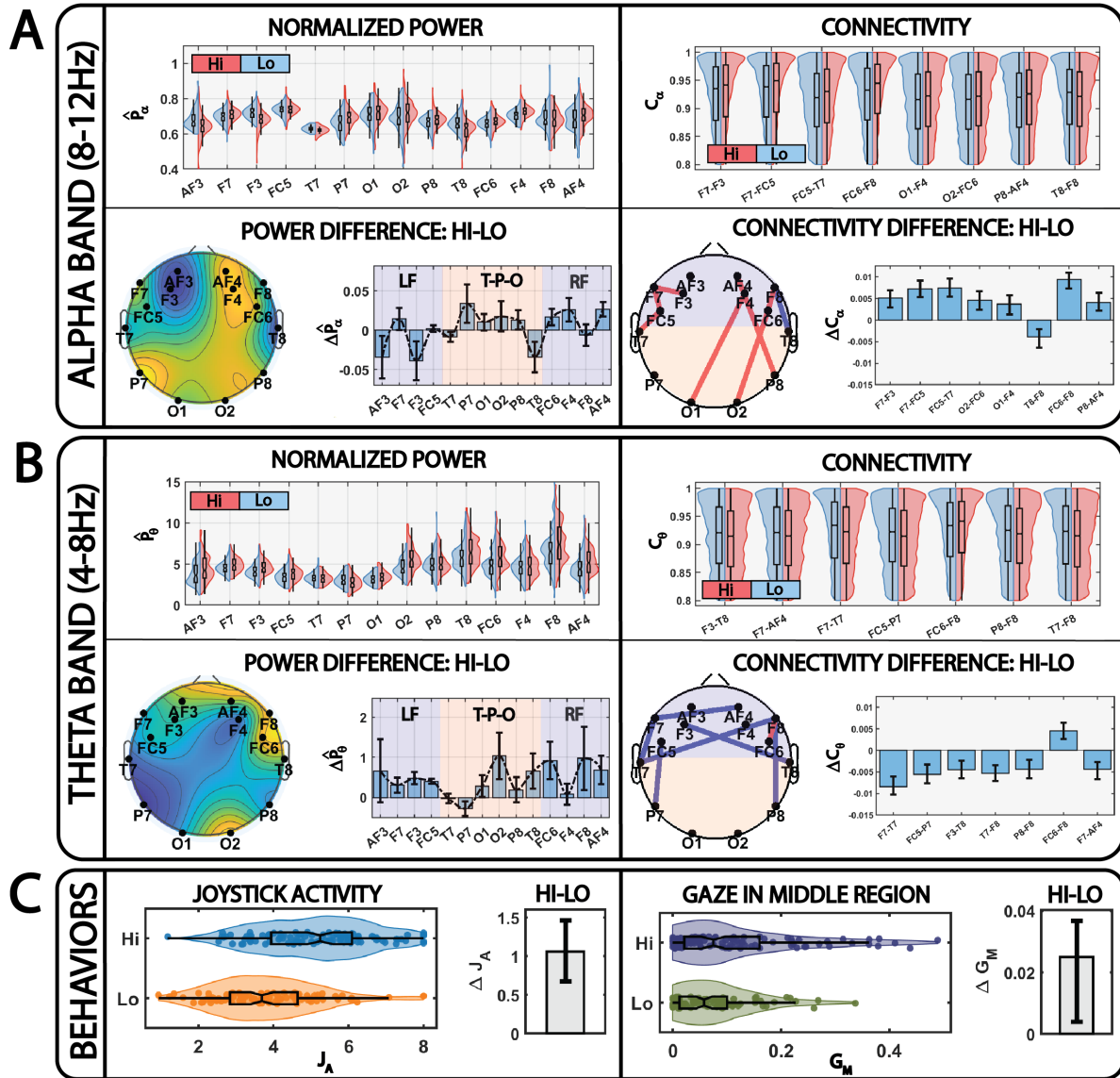
Figure 2.13: A comparison of the neurophysiological and behavioral differences associated with the factor performance. Power and connectivity in the α band are presented in (A) while those in the θ band in (B). The High performance group is labeled as *HI* and the low performance group is labeled as *LO*. Raw data are illustrated with violin plots while the statistically significant differences are detailed in the bar plots. Behavioral results are shown in (C).

2.5.4.4 Discussion

In this study, we see that the distribution of $\Delta\hat{P}_\alpha$ in the parietal and occipital channels is positive for the higher performing subjects, and in fact more so than those elicited between the different configurations. As before, the greater $\hat{P}_\alpha$ in the occipital region indicates

the suppression of sensory information from task irrelevant visual stimuli. Likewise, the increase in C_α between the occipital and frontal regions, specifically O1-F4 and O2-FC6, is also indicative of top-down suppression of visual stimuli and a greater focus on internal attention. Similarly, the higher performing subjects exhibited more $\hat{P}_\theta$ in the frontal region, which indicates a greater utilization of working memory resources. Finally, higher performing subjects spend more time looking in the middle region, and utilize a greater amount of pilot input. An important result worthy of note is the negative change in C_θ between high and low performers. This difference stands in contrast to the previous analysis in which subjects piloting the rectangular configuration show increases in both frontal $\hat{P}_\theta$ and C_θ compared to the serpentine configuration. As mentioned earlier, such results are generally difficult to interpret, and we will not do so here.

Given these observations, the differences between subject groups conforms to a predictable pattern. Higher performing subjects drive the configurations faster and miss fewer targets, but while doing so, they utilize a greater amount of visual-spatial reasoning and internal processing than lower performers. Additionally, higher performers spend a greater amount of time looking in the middle region, while simultaneously using more control input. Nevertheless, these results stand in direct contrast to *Hypothesis 2*. Interestingly, higher performing subjects are not naturally more effective with the given control interface. Our results suggest that high performers use more cognitive resources to perform at a higher level, indicating that they are more engaged in the task. In fact, it has been shown that individuals with higher working memory capacity tend to be more efficient at controlling attention by minimizing the effect of distracting information via suppression of task irrelevant stimuli [58]. The greater difference in occipital power associated with sensory suppression may therefore indicate that higher performers may control their attention more effectively, allowing them to exceed at this particular task.

2.5.5 Hypothesis 3: Minimum Set of Network-Based Features

This section presents the statistical test results between the two levels of the within-subject factor of Gaze with two levels of *fixation* and *saccade.* The results are illustrated in Figure 2.14.

2.5.5.1 Feature Selection

In this study, we were not concerned with the specific frequencies at which features occurred, but rather, the metric type(s) and total number required to distinguish gaze behaviors. The identification of a potential minimum feature set required a method to arrange results from the statistical tests. As a means of visualization, each statistical test with $p < 0.05$ is assigned a point in the space $P_{ijk} = (M_i, S_j, f_k)$ where $j \in \{1, 2, \cdots, 9\}$ is the index of subjects, and $i \in \{1, 2, \cdots, 6\}$ and $k \in \{1, 2, \cdots, 32\}$ are the indices of metrics and frequencies respectively. This space is illustrated in Figure 2.14, where *serpentine* is represented by red circles and *rectangle* by green squares. Each feature is assigned a score, from zero to 9, representing the total number of subjects whose gaze can be discriminated in a particular configuration. Scores are sorted from highest to lowest first by feature, and then by configuration. We seek to find the set of N unknown features that will span total population of 18 separate conditions (9 subjects for *serpentine*, and 9 subjects for *rectangle*). Efficient features have the highest scores and posses the greatest amount of overlap, i.e. they will cover the largest number of subjects and configurations.

For comparison, we performed an identical analysis using features derived from temporal metrics that have been used in the classification of human cognitive states [59]; specifically, channel power, channel RMS, and channel peak-to-peak. Data from each of the 14 channels were bandpass filtered into the frequency bands θ (4-8Hz), α (8-12Hz), and γ (12-32Hz) common in EEG analysis. In addition, narrow-band channel power at the 32 discrete frequencies extracted from the time-frequency decomposition were also used. We generated, statistically tested, scored, and sorted single-channel features in the same manner described above.

2.5.5.2 Discussion

Network metrics cover a range of topological properties relevant to the neural activity associated with cognitive processes. The brain is known to have distributed neurophysiological networks consisting of functionally integrated clusters of synchronized activity with sparse connections between them [26]. Metrics such as transitivity contain

average local information about the clustering of nodes, while modularity indicates the complex distribution and connections between these dense clusters. Both metrics are considered to be measures of the segregation of the network. Efficiency on the other hand is the inverse mean path length between all nodes in the network and represents a measure of integration [56]. The remaining metrics of component count, maximum node degree, and density contain basic information about the mechanical properties of the network with less regard to structure. The information contained in the metrics can overlap to varying degrees, but this is not always so. For example, a network with highly variable modularity may be comprised of a single component, or one with large span of maximum degrees can maintain a relatively stable modularity.

Our initial assumption for *Hypothesis 3* was that if a minimum set existed, it would be comprised of features from several different network-based metrics. Contrary to this expectation however, we find that minimum sets exist for each metric independently. The minimum number of features for each metric M_i is equivalent to the number of rows in each shaded plane in Figure 2.14. These results are collected in Table 2.8 where each row contains a specific metric, the minimum number of features generated by that metric, and the frequencies at which those features occur. Configurations associated with each feature are included in parentheses. Four of the network-based metric generate minimum sets of 2 features with maximum degree and component count generating 3 and 4 features respectively.

Table 2.9 presents the results of our comparative analysis using single-channel features. The subset of conditions covered by the wide-band metrics are listed in the third column of the table. Single-channel features defined within the wider θ, α, and γ bands are incapable of spanning the total population of conditions. Only narrow-band power with its finer granularity of bandwidth was able to generate a minimum set of 12 features. These 12 features are comprised of data from 7 of the 14 EEG channels: F3 (5 conditions), FC5 (2 conditions), F7 (2 conditions), T7 (1 condition), O1 (1 condition), O2 (1 condition), and F4 (3 conditions).

Comparing the performance of network-based versus single-channel features reveals

the power of using network-based methods. Single-channel features do not account for inter-channel relationships. The random loss of a single channel yields a 50% probability of losing a single condition. A loss of F3 would result in a 27% reduction of the number of conditions covered. The most important single-channel features are extracted from channels located in the frontal lobe. As we have stated, dense clusters of nodes will exist in the frontal lobe and the single loss of a frontal channel may have little effect on the final value of transitivity and modularity. Those particular metrics can be affected if the lost channel represented a network hub providing communication between different modules. Due to the shear number of statistical tests in this study, we did not examine the location of network hubs or the nodes within each module. That analysis would have provided more information about the robustness of these measures to the loss of specific nodes in the network. Nevertheless, the additional metrics provide a measure of resilience to channel failure. If for instance we lose a channel containing a network hub, then modularity could decrease. Component count however, may increase due to the disconnection of modules, and transitivity may increase due to the larger number of tightly connected nodes. A selection of several network-based features will guard against the loss of individual channels. Therefore, single EEG channels do not contain robust discriminative information, yet the inter-channel relationships captured by network-based metrics do.

In addition, there exist several network-metric based features for which a prior knowledge of the particular configuration can reduce the minimum set to a single feature. These configurations are emboldened and underlined in Table 2.8. For example, if subjects pilot the serpentine configuration, then we can distinguish gaze states using transitivity at 24.7 Hz, or maximum degree at 9.2 Hz. Likewise, if subjects pilot the rectangular configuration, then we can use density at 31.9 Hz. Modularity displays the unique property of possessing single features for each configuration independently: the serpentine at 9.2 Hz and the rectangle at 22.6 Hz. The modular structure of the brain is known to undergo changes in response to external (sensory) and internal (cognitive) drivers [60]. Dynamic network reconfiguration within the frontal lobe has been

associated with task demands [61]. Consequently, the configuration specific modularity based features supports the notion that different cognitive processes occur in relation to piloting the different configurations. This is a key result that reinforces the conclusions from H1.

Finally, these network-based features can be calculated in real time as the task progresses. Five of the metrics are determined directly from the adjacency matrix A. Only modularity requires estimation using optimization algorithms [56] and may take longer to calculate depending on the number of nodes and edges in the network. Accordingly, network-based features could be used to rapidly detect and classify cognitive states associated with changes in mental workload, situation awareness, or trust. Our future investigations will utilize an EEG device with a larger channel count. The increase in channels, particularly in the temporal and occipital regions, would allow us to observe the larger modular structure know to exist between these regions and will increase the effectiveness of our network-based methods.
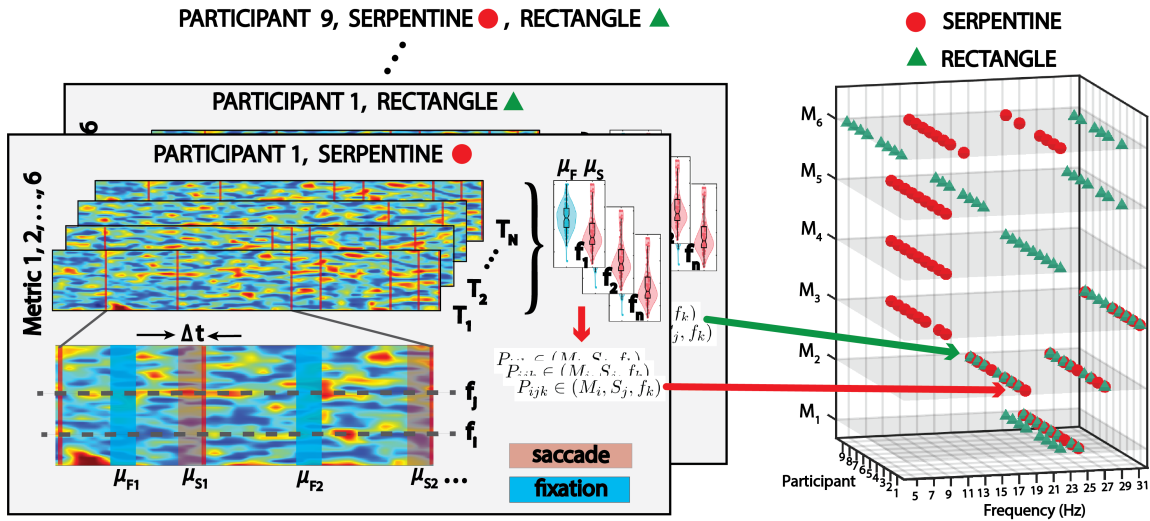
Figure 2.14: A detail of the generation and extraction of relevant features for identification of gaze states. Features comprised of average metric values during the Δt=250 ms preceding a saccades (in red), are compared against those directly between saccades (fixations, in blue). Statistical tests are performed for all conditions (subjects and configurations) in this experiment. Statistically significant differences $p < 0.05$ generate a point $P_{ijk} \in (M_i, S_j, f_k)$ in the space of metrics, frequencies, and subjects. The minimum feature set for each metric are defined by the columns of points in each shaded plane.

Table 2.8: Minimum Feature Set Using Network Metrics

Metric Type	Feature Count	Frequency(Configurations)
M_1 Transitivity	2	22.6(Rec), 24.7(**Srp**,Rec)
M_2 Efficiency	2	18.5(Srp,Rec), 27.8(Srp,Rec)
M_3 Density	2	9.2(Srp), 31.9(Srp,**<u>Rec</u>**)
M_4 Modularity	2	9.2(**<u>Srp</u>**), 22.6(**<u>Rec</u>**)
M_5 Maximum Degree	3	9.2(**<u>Srp</u>**), 14.4(Rec), 29.8(Rec)
M_6 Component Count	4	4.0(Rec), 11.3(Srp), 22.6(Srp), 29.8(Rec)

Table 2.9: Minimum Feature Set Using Single-Channel Metrics

Metric Type	Feature Count	Total Conditions	Channels
θ, α, γ Power	NA	15 out of 18	NA
θ, α, γ RMS	NA	15 out of 18	NA
θ, α, γ Peak-to-Peak	NA	14 out of 18	NA
Narrow-band Power	12	18 out of 18	F3, FC5, F7, T7, O1, O2, F4

2.6 Conclusion

In this chapter we examined whether the reduction in human-multiagent team task performance due to an increase in the geometric complexity of a robotic group is reflected in average neurophysiological and behavioral measures. Ten subjects were locally embedded in a task space. Each subject piloted six ground robots in two geometric configurations: a serpentine ($GC = 2$); and a rectangle ($GC = 6$). Our tests revealed that the use of a higher GC configuration yielded a decrease in task performance and that this reduction was accompanied by increases in spectral power and functional connectivity that indicate more internal processing, access to working memory, and suppression of visual stimuli. Complementary changes in gaze and pilot input enforce the conclusion that increasing the GC places a greater burden on the human subject's cognitive resources that detrimentally affect the outcome of a human-multiagent team task. In addition, higher performing subjects, regardless of the GC, tended to engage more actively in the task, utilizing a greater amount of visual-spatial reasoning to perform more effectively. Finally, we show that features based

on EEG dynamic-network-metrics distinguish gaze behaviors associated with the attention process more effectively than traditional single-channel metrics, indicating that single channels do not contain robust discriminative information, while the inter-channel relationships do. Network-based metrics capture the natural modular structure of the human brain as it dynamically reacts to changes in task demands. This is one of the first studies to utilize a dynamic network analysis to link cognitive processes with behaviors in a human-multiagent-team task.

2.7 Acknowledgment

Chapter 3

An EEG Network Examination of Human Trust in Autonomy

Preface

Autonomous agent teammate-likeness has been described as *"the extent to which a human operator perceives and identifies an autonomous, intelligent agent partner as a highly altruistic, benevolent, interdependent, emotive, communicative and synchronized agent and teammate, rather than simply an instrument or tool."* [62]. A key element in effective human-autonomy teaming is the establishment and maintenance of appropriate trust [63]. In this chapter, we report our results in measuring human trust in autonomy both continuously and unobtrusively using interactions between brain regions as determined from an electroencephalogram (EEG).

The major contributions of this chapter are as follows: 1) We show that human trust in an autonomous system cab be measured continuously and unobtrusively; 2) Using analysis techniques which account for interactions among brain regions shows benefits compared to more traditional methods which use only EEG signal power. To the best of our knowledge, this is one of the first studies to incorporate network based features in the prediction of trust in autonomy.

The contents of this chapter have been submitted for publication [37]

3.1 Introduction

Studies have shown that a human's miscomprehension of an autonomous system's state, decisions, or course of action can result in misuse or disuse of the agent, causing a reduction in team-task proficiency. This degradation can be mitigated if trust between the human and autonomous agent [64] is appropriately calibrated [65]. Consequently, the human and their autonomous teammate should have shared intent [33], and a similar focus of attention [5] to maximize trust. Achieving effective and efficient human-autonomy team-task performance can be significantly augmented if the autonomous agent has direct access to the internal cognitive state of the human both unobtrusively, and in real-time.

3.1.1 Trust

Trust is a complex and multifaceted construct, yet one in which all humans are inherently familiar and capable of assessing qualitatively. Nevertheless, there is no universally agreed upon definition of trust [66]. Within the context of a team-task, trust is established and maintained through the bi-directional interaction between one who evaluates the level of trust (a trustor) and one who impacts the level of trust (a trustee). As the task proceeds, each team member re-evaluates their trust in the another. Levels of trust may change due to variation of task complexity, the transparency of the teammate, or a perception of their capability [67].

The human-autonomy literature frequently defines trust as "the attitude that an agent will help achieve an individual's goals in a situation characterized by uncertainty and vulnerability" [68]. When a human (the trustor) works with an autonomous system (the trustee), the bi-directional interaction is effectively severed. Human trust in the autonomy is initialized by their predisposition to trust, and is continuously impacted by the perception of competence, level of risk, fatigue, and even the self perception of their own capabilities [69]. The trustor's subjective assessment towards the trustee is changed with the behavior of the autonomous system. When the trust in autonomy is negatively impacted, it can be difficult for the human to regain it [70]. The trustor's subjective assessment towards the trustee is changed with the behavior of the autonomous system. Trust is commonly conceptualized as a latent variable that cannot be directly observed but

rather must be inferred. Trust is dependent on the interplay between analytic, analogical, and affective processes, especially emotional responses to violations or confirmations of expectations [68]. The evaluation of capabilities, the perception of risk, and thereby the decision to trust are inherently cognitive in nature. Just as it is critical for the human to comprehend and predict the behaviors of an autonomous agent, it is equally critical for the autonomous agent to understand the cognitive state of the human in order to determine when, or potentially how, to communicate their own intentions or clarify their behavior.

In a human-autonomy team, the human must be able to adequately trust the autonomous agent in order to yield the appropriate amount of agency [64]. Low levels of trust prevent the human from utilizing the autonomy to its full potential while higher levels of trust encourage the human to relay on the autonomy beyond its capabilities. In a well integrated human-autonomy team, the human must have an adequate estimate of the agents capabilities and trust that it will perform optimally. This concept is known as trust calibration [68]. It is outlined in Figure 3.1.
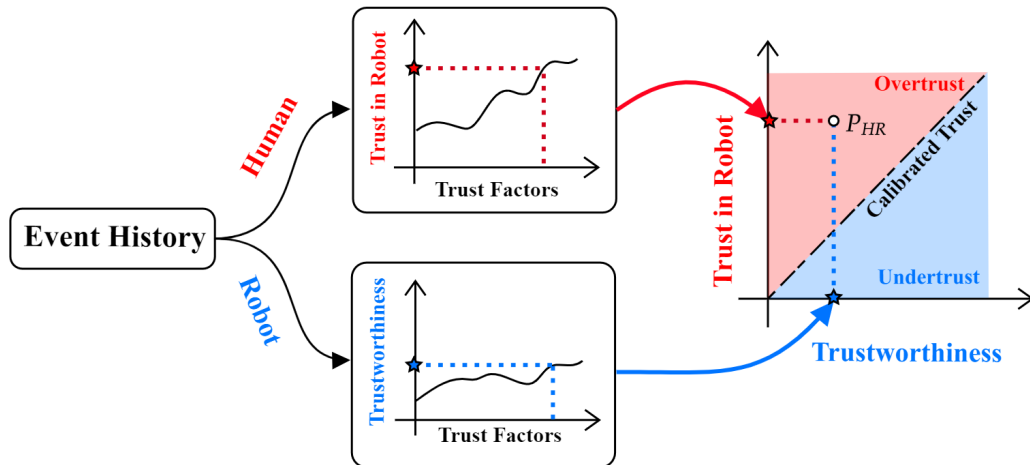
Figure 3.1: Illustrating the concept of trust calibration. The human must properly understand the capabilities of the autonomous agent, and trust that it will perform to the benefit of the shared team goal.

3.1.2 Measuring Trust in Autonomy

As there is no universally agreed upon definition of trust, there is also no universal way of measuring it. Much like a human-human interaction, it is assumed that the actual state of

trust the human has in the autonomy is continuous. Trust measures are categorized as self report, behavioral, and physiological indices [71]. Typical methods of trust measurement are performed using surveys that are applied at various intervals [72, 73]. These methods cannot adequately capture the continuous nature of trust. The human must remove themselves from the task and attend to the survey itself. Depending on the specific scenario, attending to a survey can range from inconvenient to absolutely detrimental to task performance which in turn can have substantial impacts on trust. Similarly, surveys administered at the end of the task may only capture the human's net evaluation of trust over the length of the interaction. These methods lack the ability to measure trust both dynamically and unobtrusively. There has also been substantial work to measure trust continuously or semi-continuously through the use of physiological signals such as skin conductivity and behaviors such as gaze [74]. Additional studies have also examined EEG channel power as it relates to changes in trust [75].

3.1.3 EEG and Network Science

Neurophysiological correlates of human cognitive state have been studied using the electrical signals recorded directly from the surface of the scalp, known as an electroencephalogram (EEG) [76] EEG is a common, non-invasive measure of brain activity. An EEG system is comprised of an ensemble of electrodes placed directly onto the scalp. Voltage measurements, on the order of $100\mu V$, correspond to the average neural activity in the brain area located directly beneath the electrode. Historical studies using EEG primarily investigate the magnitude and spatial distribution of signal power within well established bandwidths θ (4-8Hz), α (8-12Hz), β (12-30Hz), and γ (>31Hz). However, it is widely believed that cognition manifests through interactions between brain regions over a variety of spatial scales [29]. Synchronization of brain oscillations have been proposed as a key concept in neural processes underlying cognition [77]. Regions of the brain that exhibit statistical interactions in the absence of established neural pathways are known as "functionally connected regions". A spatial distribution of such brain regions along with the statistical correlations establishes a topological network that can be described succinctly using elements of graph theory.

Descriptive measures of global features of network topology have been widely applied to EEG data. These analyses reveal nonrandom topological aspects, such as high clustering or short path length [78], and metrics of dynamic functional connectivity may indicate changes in macroscopic neural activity patterns underlying critical aspects of cognition [79, 80].

3.1.4 Experimental Hypotheses

Our study investigates methods to determine dynamic changes in human trust in autonomy as reflected in EEG measures using methods derived from network science with the aim to improve human-autonomy interaction in team-task scenarios. We view the dynamic trust process as event-centric [81], and changes of human trust in autonomy are decision points that can be elicited through discrete events or actions. Temporal changes in both EEG power and inter-channel functional connectivity indicate cognitive activity which may correlate with changes in trust. Our investigation has been divided into two separate hypotheses.

H1: *A properly selected set of global network-metric features derived from EEG measurements predicts human trust with a higher accuracy than that of single-channel features.* This study analyzed models of trust prediction using features derived from the full compliment of electrodes in our EEG headset and represents the limit of what our specific instrument can tell us about the global inter-connectivity of all brain regions.

H2: *A properly selected set of local, network-metric features derived from EEG measurements predicts human trust with a higher accuracy than that of local single-channel features.* In this study, we analyzed models using features derived from subsets of electrodes located above specific sets of brain lobes. We explore the inter-connectivities of more granular local regions that may show a stronger tendency to integrate with changing levels of trust.

To evaluate these hypotheses, we designed an experiment to evoke changes in a

human's trust in an autonomous system as they perform a team-task. Participants were instructed to self report their state of trust whenever they wish. We assume that changes in the internal state of trust occur when the human self-reports. The self report of trust allows us to focus on the potential relevant cognitive processes that may occur during the decision event. This method contrasts with existing studies in three ways: 1) The participant is allowed to guide us when to look for potential relevant changes in trust; 2) The participant is not disengaged from the task to fill out specific trust surveys at discrete times; 3) There is no aggregate evaluation of trust upon completion of the task.

3.2   Experiment

3.2.1   Participants

This experiment was approved by the University of California, Davis Institutional Review Board. Informed consent was obtained from 3 participants: all male graduate students between the ages of 24 to 29 years old. All completed the full experiment of 16 trials as described in Section 3.2.2. Each participant was briefed on the function of the instrumentation and testing procedure. Prior to the experiment, participants filled out a demographics survey which included questions regarding previous night's amount of sleep, consumption of caffeine, prior experience with robot/autonomous systems, and video gaming experience.

3.2.2   Task

This experiment investigated how changing levels of human trust in autonomous systems are reflected in brain activity, specifically, scalp voltages measured with an electroencephalogram (EEG) headset. We designed our human subject experiment using a ROS-based simulation shown in Figure 3.2. Our screen based experiment consisted of a human participant remotely overseeing the placement of stowage onto an equipment rack by a UR5e robotic arm, ostensibly located on the International Space Station. The participant worked in collaboration with the robot to ensure the proper placement of stowage required for the onboard crew to perform the repair/maintenance task.

Participants were instructed that the proper placement of stowage onto the rack as commanded by the offline planner was critical to the effective performance of the maintenance task.

Within the simulation, specific articles of stowage were represented as colored cubes. Participants were informed that an automated planner would determine the sequence of cubes to be placed onto a rack. The sequence was communicated to the participant through the *Placement Request* panel. Using a mouse, the participant would sort the cubes from a *Tool Bin* by selecting the proper colored cube and placing it into the *Robot Command* queue. Once the queue was full, the participant clicked a button to start the robot placement sequence. The participant was informed that a planning algorithm decided how the cubes would be picked and placed onto the rack. As a means to elicit changes in the participant's trust, the capability of proper stowage placement was modulated between two levels of placement accuracy: 90% and 30%. These levels were randomized and unknown to the participant. As the robot performed the placement task, the participant was instructed to self report their trust in the robot via a horizontal slider located directly under the *On Board Camera* panel. High trust was reported by positioning the slider to the right, whereas low trust was reported by positioning to the left. Trust values vary from 0 (no trust) to 1 (complete trust). Each participant was allowed to determine when, and by how much they decided to report their level of trust. Once the robot was finished placing the 4 cubes, the window was reset and a new sequence of cubes was displayed in the *Placement Request* panel. The following text was read to the participants prior to the experiment.

> You are a member of the ground crew in support of a maintenance task on the International Space Station. An additional support group within the ground control structure has developed a plan on how the onboard crew will perform a specific maintenance task. This plan will require tools to be placed in a specific order onto several shelves of a rack. While the plan is being reviewed by the crew, you and the robot are responsible for selecting tools from a stowed package and placing them onto the rack. After the tool placement

REMOTE HUMAN-ROBOT INTERACTION PANEL
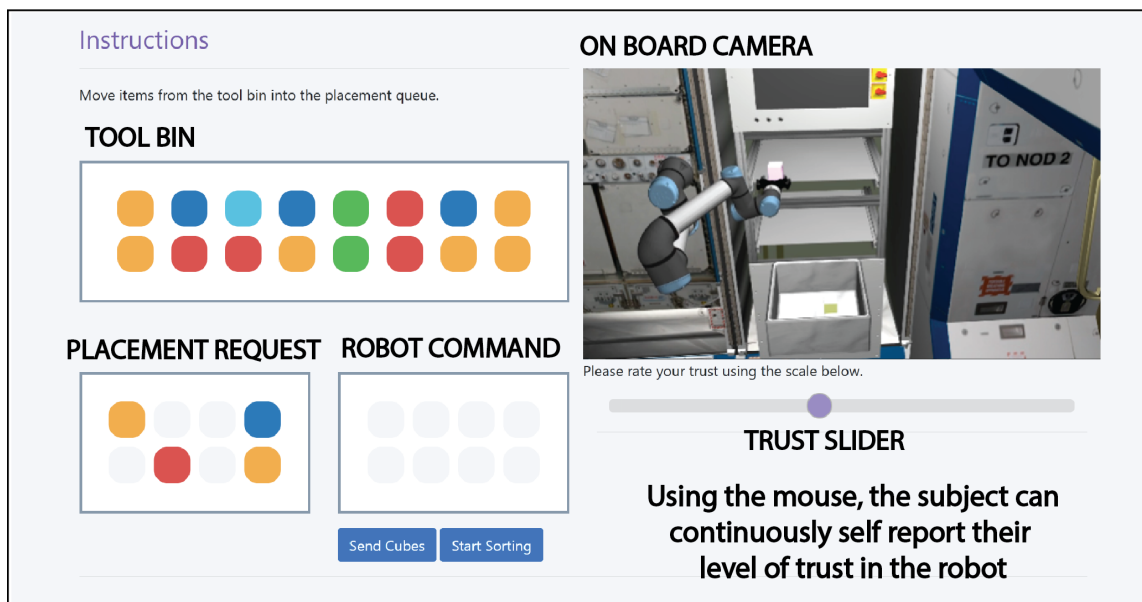
Figure 3.2: A detail of the remote test panel used in this study. Each participant interacts with the system via the *Tool Bin, Placement Request*, and *Robot Command* panels. Cube placement is viewed through the *On Board Camera panel*. The participant signals changes in their level of trust using the *Trust Slider*.

has occurred, an onboard crew member will be required to pick up the tools in the requested sequence in order to perform the maintenance task according to the prescribed plan. When you select the tools, and place them into the queue, they will monitor the robot to ensure that the tools are placed properly.

In this experiment, we are evaluating several planning algorithms that are used by the robot controller to place the parts onto the rack. It is imperative that you and the robot are able to collaborate together effectively to perform this task. Therefore, we wish to evaluate your trust in the robot as it performs the part placement. You can signal your trust throughout the experiment using the horizontal slider that is provided. There is no right or wrong value of trust—we wish to understand when and how much your trust changes throughout the performance of the task.

3.2.3 Apparatus

A detail of the experimental setup is shown in Figure 3.3. Electrophysiological data were collected from each participant using a EEG recording suite manufactured by g.tec. The system is comprised of the g.HIamp amplifier and 62 channels of active electrodes mounted into a single flexible cap. Gaze position and pupil diameter were measured using a Tobii Nano Pro screen based gaze tracker. The gaze tracker captured pixel position of gaze, pupil diameter and blinks at a sample rate of 60Hz and is optimized for screen based experiments. In addition, mouse position and button clicks were recorded. All data were synchronized and recorded using Lab Streaming Layer at their native sample rates.
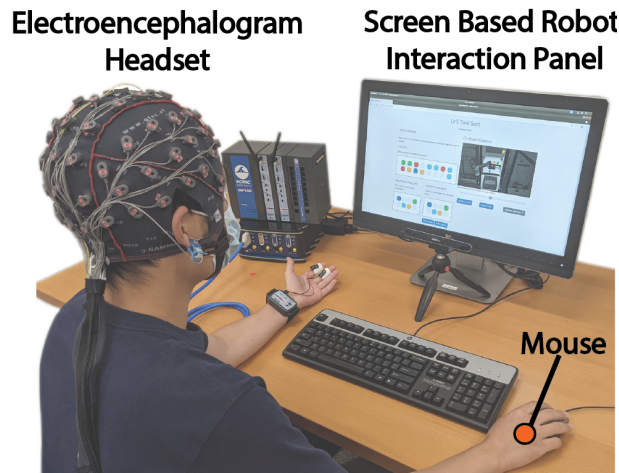
Figure 3.3: Detail of the experimental setup. Each participant was seated in front of a screen displaying the remote interaction panel. Brain activity was measured using an EEG device. In addition, gaze and mouse clicks were recorded.

3.2.4 Procedure

Prior to an experiment, each participant was outfitted with the 62 channel EEG headset. The active electrodes were filled with conductive gel and electrode impedance was verified to be below 10kΩ using the g.tec data acquisition software. Next, the eye tracking device was calibrated for the particular participant. Participants were instructed on how to perform the human-robot team task using the interaction panel shown in Fig 3.2. A complete experiment consisted of 4 GROUPs[1] of 4 trials for a total of 16 placement trials

---

[1]Capitalization is used to specify a 4 trial section. A GROUP is shown by horizontal bars in Figure 3.5

as shown in Figure 3.5. After each GROUP, a trust survey was administered and a five minute rest period was provided. The total experiment lasted approximately one hour. A short video of a single trial is available at https://www.youtube.com/watch?v=V8t-Vu7sehw.
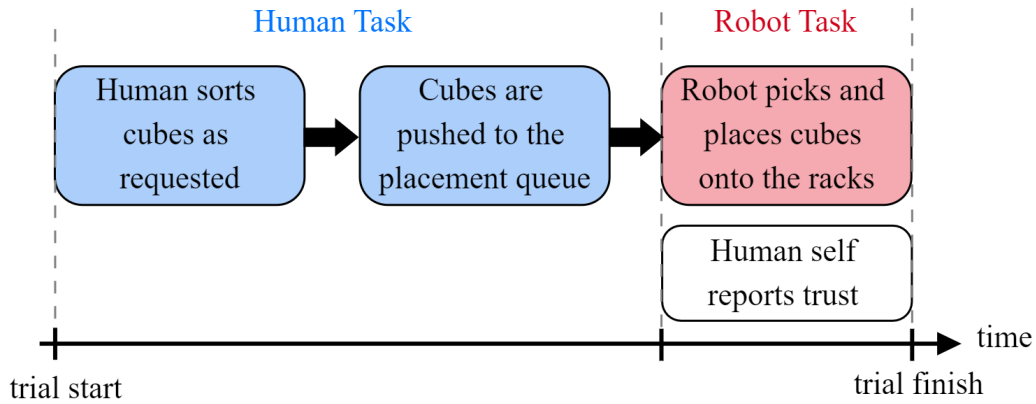
Figure 3.4: Detail of human-robot team task for a single trial. Each trial consists of the sort and placement of 4 cubes.
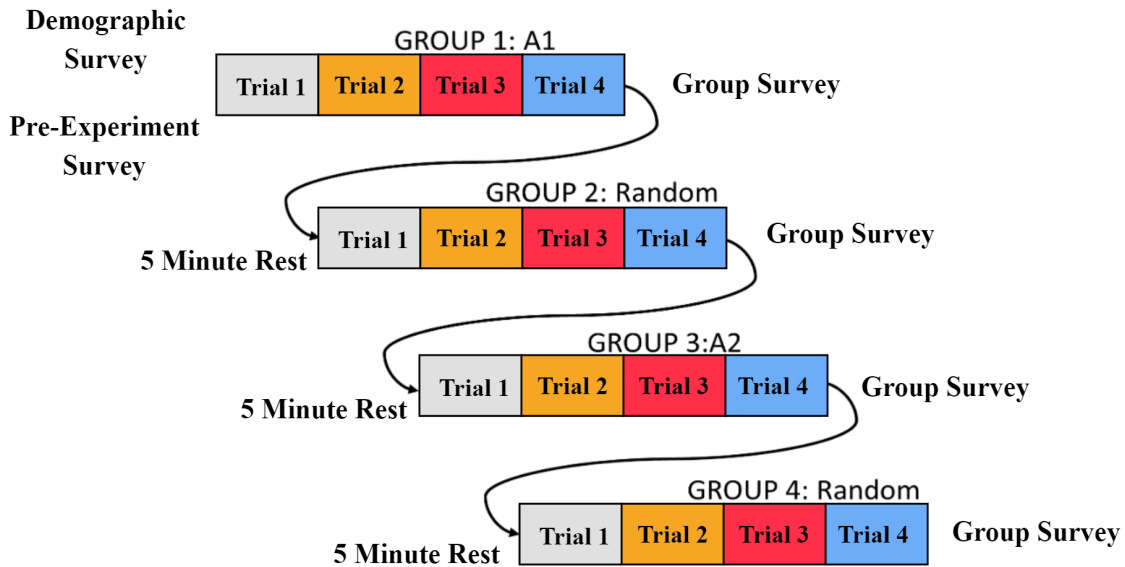
Figure 3.5: Detail of the trials performed by each participant during the experiment. Each participant began with 2 surveys then moved through 4 GROUPs of 4 block placements. After each GROUP, participants filled out a short trust survey and took a 5 minute rest. The total experiment lasted approximately one hour.
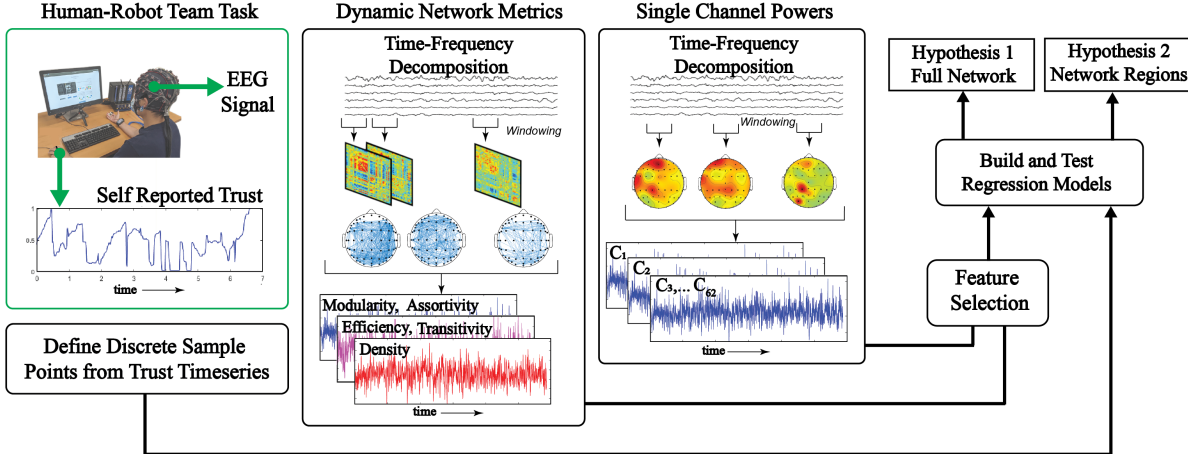
Figure 3.6: Data conditioning pipeline. EEG data are recorded along with self reported trust. Features derived from network-metrics and single channel powers are selected as regressors. Linear models are constructed from the regressor sets and the results are compared.

3.3 Methods

We tested our hypotheses by comparing the performance of linear models built from regressors selected from two separate feature types: 1) Single-channel (SC) powers; 2) Network-metrics (NM). In this section, we describe the methods used to generate our data and prepare it for analysis. The data analysis pipeline is shown in Figure 3.6.

3.3.1 EEG Features

Our EEG headset recorded 62 channels of scalp voltages (μV) at a sample rate of 1.1 kHz. The EEG data were filtered with a zero lag 4th-order bandpass filter (2-50Hz). We performed a time-frequency decomposition using Morlet wavelets [82, 83] over a set Ω of 30 equally spaced frequencies between 3 and 50 Hz. The time-frequency transform yielded a temporal sequence of complex values given by:

$$W(t, \omega_i) = A(t, \omega_i)e^{j\phi(t,\omega_i)} \tag{3.1}$$

where $\omega_i \in \Omega$. We extracted frequency dependent power, $P = A^2$ (μV^2), and phase ϕ (rad) directly from Equation 3.1 for each of the 62 channels in the EEG headset.

3.3.1.1 Functional Connectivity

In this study, we used phase synchrony as the measure of interaction between EEG electrode pairs [84]. We calculated this quantity from the instantaneous phase difference between electrode pairs l and m as follows:

$$\Delta\phi^{lm} = \phi^l - \phi^m \tag{3.2}$$

where ϕ is given by Equation 3.1. Two electrodes are considered synchronized over a time period $\Delta t = t_2 - t_1$ if $|\Delta\phi_{t_2}^{lm} - \Delta\phi_{t_1}^{lm}| < C$ for an angular threshold C. Rather than using a radian measure of $\Delta\phi$, we described synchronous behavior using phase synchrony (PS) ψ_{lm}, formally defined as follows:

$$\psi_{lm} = \frac{1}{N_T}\left\|\sum_{i=1}^{N} e^{j\Delta\phi_i^{lm}}\right\| \tag{3.3}$$

where N_T is the number of discrete time points within a period Δt. PS values vary from 0 to 1.

3.3.1.2 Dynamic Network Metrics

A network is defined as a binary undirected graph $G = (V, E)$ comprised of a set of nodes $V \in (1, 2, \ldots, N_C)$ with N_C total nodes, and an edge set $E \subseteq \left\{(x, y) \mid (x, y) \in V, x \neq y\right\}$. Each network node is mapped directly to an EEG electrode. For the remained of this chapter, each electrode/node will be referred to as a channel[2]. Hence, inter-channel connectivity refers to the PS values between electrode/node pairs. The network can be described via a symmetric square adjacency matrix $A \in \mathbb{R}^{N_C \times N_C}$. The elements of A are given as

$$A_{lm} = \begin{cases} 1 & \psi_{lm} > \delta_{PS} \\ 0 & otherwise \end{cases} \tag{3.4}$$

where ψ_{lm} is the PS between channels l and m as described in Equation 3.3, and the parameter δ_{PS} encodes the maximum allowable phase difference. PS values between individual EEG channels were calculated over a sliding temporal window of Δt=0.4 s [85].

---

[2]The term channel is derived from the use of the 10-20 International Standard for EEG electrode placement and is commonly used for EEG recording systems. The 10-20 International Standard is detailed in Figure A.2

PS values were thresholded at $\delta_{PS} = 0.9$, yielding the adjacency matrix as shown by Equation 3.4.

Network metrics of modularity, transitivity, efficiency, density, and assortativity were calculated using the Brain Connectivity Toolbox [86] in MATLAB. The properties of each individual metric are outlined in Table 3.1. The resulting time series represented the dynamic changes in network properties throughout the human-robot team task.

Table 3.1: Regression Features

Network Metrics		
Feature	**Description**	**Range**
Modularity M_N	A global measure of how well the network forms separate, non-overlapping clusters compared to a null network model with the same connection density.	[0,1]
Transitivity T_N	A measure of the average tendency for nodes to group together into triangular (or higher order) clusters.	[0,1]
Efficiency E_N	A measure of the inter-connectivity between different regions defined as the inverse average distance between nodes in the network.	[0,1]
Assortativity A_N	Usually taken as a measure of network resiliency [87]. A positive value of assortativity indicates that the network generally consists of mutually coupled high degree nodes while negative assortativity implies that the network has vulnerable nodes.	[-1,1]
Density D_N	The number of existing network edges as a fraction of the total number of possible edges.	[0,1]

Single Channels		
Feature	**Description**	**Range**
Power P_C	Signal power of an individual EEG channel in μV^2.	[0,∞)

3.3.1.3 EEG Power

As described in Section 3.3.1, the channel powers were extracted directly from the time-frequency transform.

3.3.2 Network Sub-Regions

The use of the 62 channel EEG system provided an opportunity to explore complex interconnections between distant brain regions. However, values of network metrics do

not have unique one-to-one associations with specific distributions of network edges. Rather, they capture average properties of the network as a whole. Regional networks were comprised of channel subsets located over particular brain areas that are know to functionally interact. In addition to the full 62 channel ensemble, we analyzed six sub-regions as shown in Figure 3.7. Table 3.2 lists the names of the network sub-regions detailed in Figure 3.7 along with the abbreviations that will used for the remainder of this chapter.

3.3.2.1 Feature Counts

Each network sub-region k was comprised of N_C^k channels. With the exception of the full network, all sub-regions contained less than 62 channels. There were 30 frequencies in the time-frequency transform as described in Section 3.3.1, and the number of SC features generated for each sub-region was $F_{SC}^k = 30 \times N_C^k$. In contrast, the NM feature set for each sub-region k was comprised of the five metrics listed in Table 3.1, also evaluated at 30 frequencies. All sub-regions have $F_{NM}^k = 30 \times 5 = 150$ total NM features. Consequently, there are large differences in the number of SC versus NM features that are available for model construction. The ratio of NM to SC features, $FC_R = 150/F_{SC}^k$ for each sub-region k is also given in Table 3.2.

Table 3.2: Network Regions

Network Sub-Region	Sub-Region Acronym	Channel Count N_C	Feature Count F_{SC}	$FC_R = 150/F_{SC}$
Full	*none*	62	1860	0.08
Frontal-Central	FC	25	750	0.20
Central-Parietal-Occipital	CPO	38	1140	0.13
Temporal-Parietal-Occipital	TPO	23	690	0.22
Frontal-Parietal-Occipital	FPO	35	1050	0.14
Frontal-Temporal-Parietal-Occipital	FTPO	41	1230	0.12
Anterior-Frontal-Central	AFC	32	960	0.16
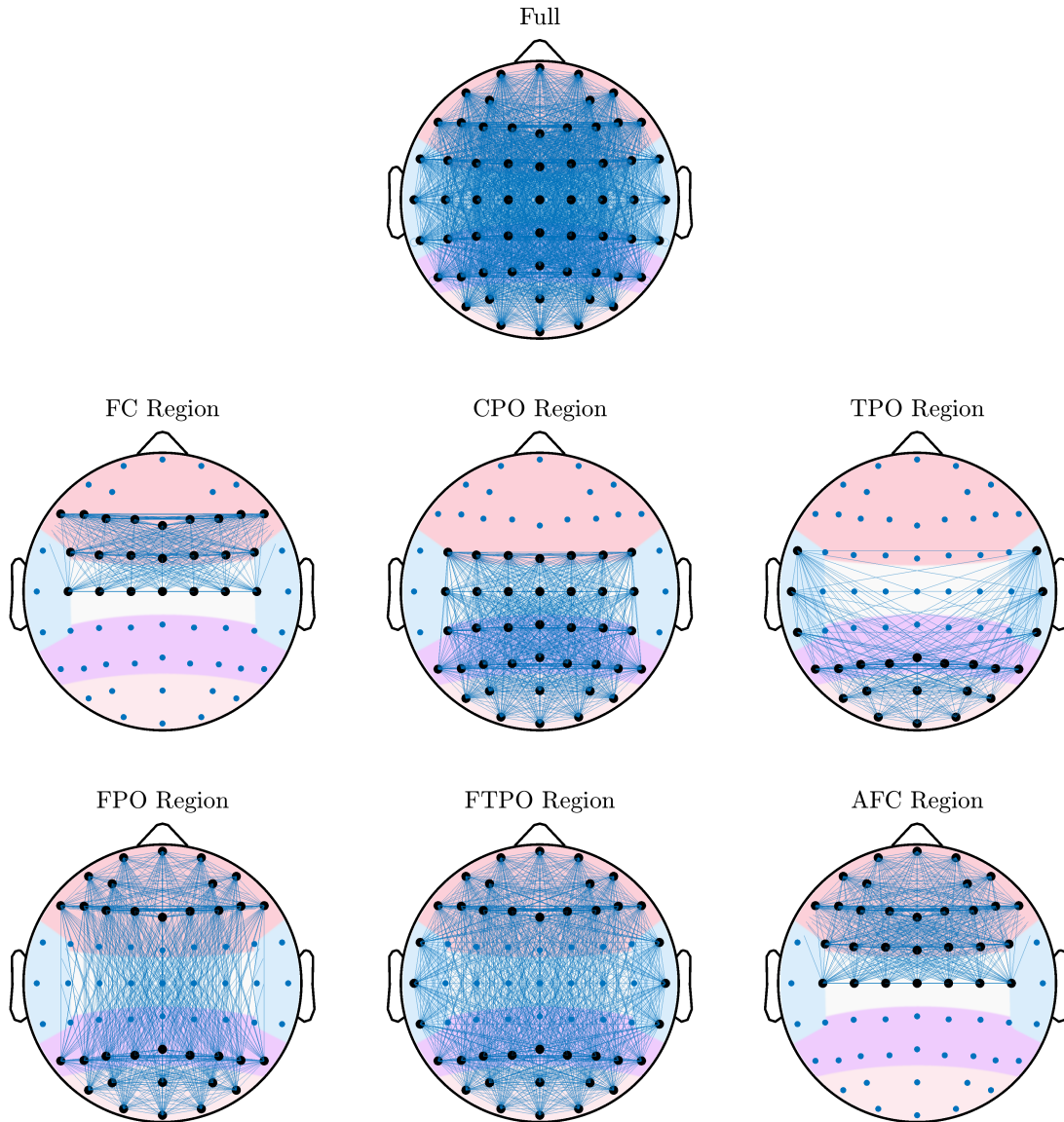
Figure 3.7: Detail of the seven networks analyzed in this study. The set of electrodes in the EEG ensemble are denoted with small markers. Network nodes are shown with larger markers while network edges are indicated by lines. Each headmap represent the total possible number of edges that can exist in the particular region. Brain lobes are highlighted using varying shades.

3.3.3 Dynamic Modeling of Trust Using EEG Measures

As outlined in Chapter 1, neural measures can capture variations in cognitive processes that relate to trust attitude. If successful, a neurological measure of trust would be the most sensitive, real-time capture possible for this latent variable. However, there is a lack of work that explores time variations in EEG functional connectivity as it relates

to changes in trust. In this study, we assume that the actual trust a human has in the autonomy is a cognitive stance, or an attitude that exists during the interaction [71]. We can model the dynamic state of trust as the discrete process shown in Figure 3.8. The internal state of trust is shown in the red circles. Observable variables of external self report of trust and EEG measures are shown in yellow. The blue circles describe the relationship between human actions, robot (autonomous system) actions, and situational factors. Situational factors can include changes in risk, increase or decrease of mental/physical demands, changes in uncertainty, or other external influences that impact the dynamics of the interaction.

Prior to the interaction each participant comes to the task with an a-priori notion of an autonomous system's trustworthiness [88]. This predispositional trust is noted as T_0^{in}, and is the result of antecedent experiences, values, and beliefs. Additionally, the type of task can impact initial trust since each person may weigh risk and reward differently for given operational contexts. Once the human-autonomy team task begins, situational factors (SF) and human actions (H^A) give rise to robot actions (R^A), all of which impact trust, T^{in}. In our experiment, we attempt to elicit changes in T^{in} via robot actions: specifically by varying the capability of the robot to place blocks onto the shelf.

Let there be an internal state of trust that the human has in the autonomous system given by T^{in}. The observation, T^{ex} human's self report of their perceived value of trust. If we regard the internal state of trust as $T^{in} \in \mathbb{R}$, and the external report of trust as $T^{ex} \in \mathbb{R}$, we claim that there is map

$$\varphi : T^{in} \mapsto T^{ex}.$$

We may also assume that there is a map from EEG features, $x \in \mathbb{R}^n$ and the state of internal trust. We posit that such correlations are due changes is internal cognitive state of the participant. Therefore, we additionally claim there is a map

$$\gamma : x \mapsto T^{in}.$$

Consequently, we can write the relationship between x and T^{ex} as the composition of φ

56
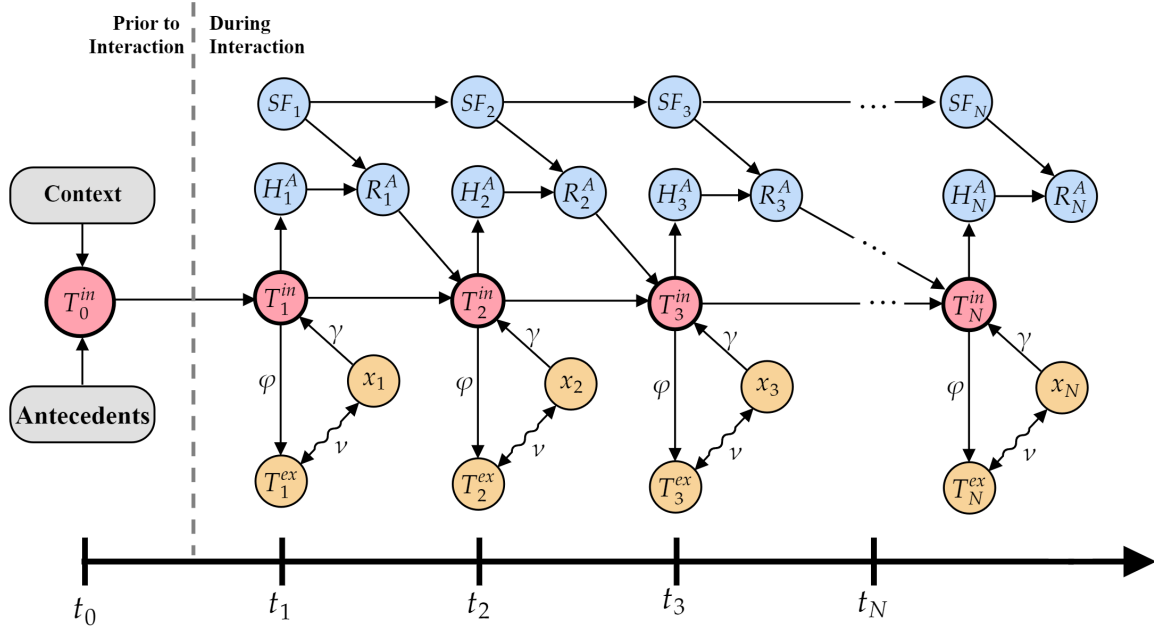
Figure 3.8: A graphical model of human trust dynamics throughout the performance of a human-robot team task.

and γ, which we note as $\varphi \circ \gamma = \nu$

$$\nu(x) = T^{ex}.$$

In this study, we evaluated the conditional probability

$$P(T^{ex} \mid x).$$

via the construction of a regression model. We assumed that the state of trust was elicited by the human participant's perception of the robot's capability. Furthermore, we assume that both trust and EEG features were continuous. For our conditional model, we select a first order, linear approximation of trust as function of EEG features given by

$$T_{est}^{mk} = a_0 + \sum_{i=1}^{m} a_i x_i^k + \epsilon_0 \tag{3.5}$$

where T_{est}^{mk} is the trust estimate using features from the kth sub-region, m is the total number of regressors, a_0 is a bias term, and a_i are the coefficients of each regressor x_i^k and ϵ_0 is an uncertainty in both the measurement and model. We additionally assumed that interactions between features were negligible. We generated linear models for each of the seven sub-regions using both the SC and NM feature sets for a total of 14 models.

We assume that changes in the internal state of trust occur when the human self-reports. If there is no report, we cannot assume a link between the internal state and the EEG signals that may correspond to it. This situation presents two problems: 1) it is possible that valid changes in trust occur, but are not reported; 2) it is possible that valid changes in trust occur over periods that are not self-reported. Each of these situations will increase signal to noise. There is little that we can do to mitigate these issues.

3.3.4 Feature Selection

We performed feature selection using a greedy feed-forward search approach implemented using the MATLAB function sequentialfs.m with root mean squared (RMS) estimation error as the loss function [89]. The algorithm begins with a constant term and constructs models from all remaining available features. Regressors are added sequentially until the relative reduction in RMS error meets a selected threshold [90]. The final number of regressors used for all models in this study was 20 as shown in Figure 3.9 for each of the seven sub-regions.

3.3.5 Participant Trust Levels

A major assumption in this study was that changes in trust occurred over large timescales such they may be captured by examining average EEG properties at discrete points in time. Our participants self reported their trust from 0 (no trust) to 1 (complete trust), $T_m \in [0, 1]$. We use the temporal characteristics of T_m to define a discrete set of time points t_r, from which to build our models. Each participant's self reported trust over the entire experiment was collected into a single ensemble. We then selected sample points as follows:

1. Discretization: The continuous trust is broken into 50 discrete levels between 0 to 1

$$T_i^p = 0.02i, \qquad i \in \{1, 2, \ldots, 50\}$$

2. Derivative Threshold: Exclude time points where the trust changes too slowly

$$\left| \frac{T_m[n] - T_m[n-1]}{\Delta t} \right| \leq \delta_d.$$
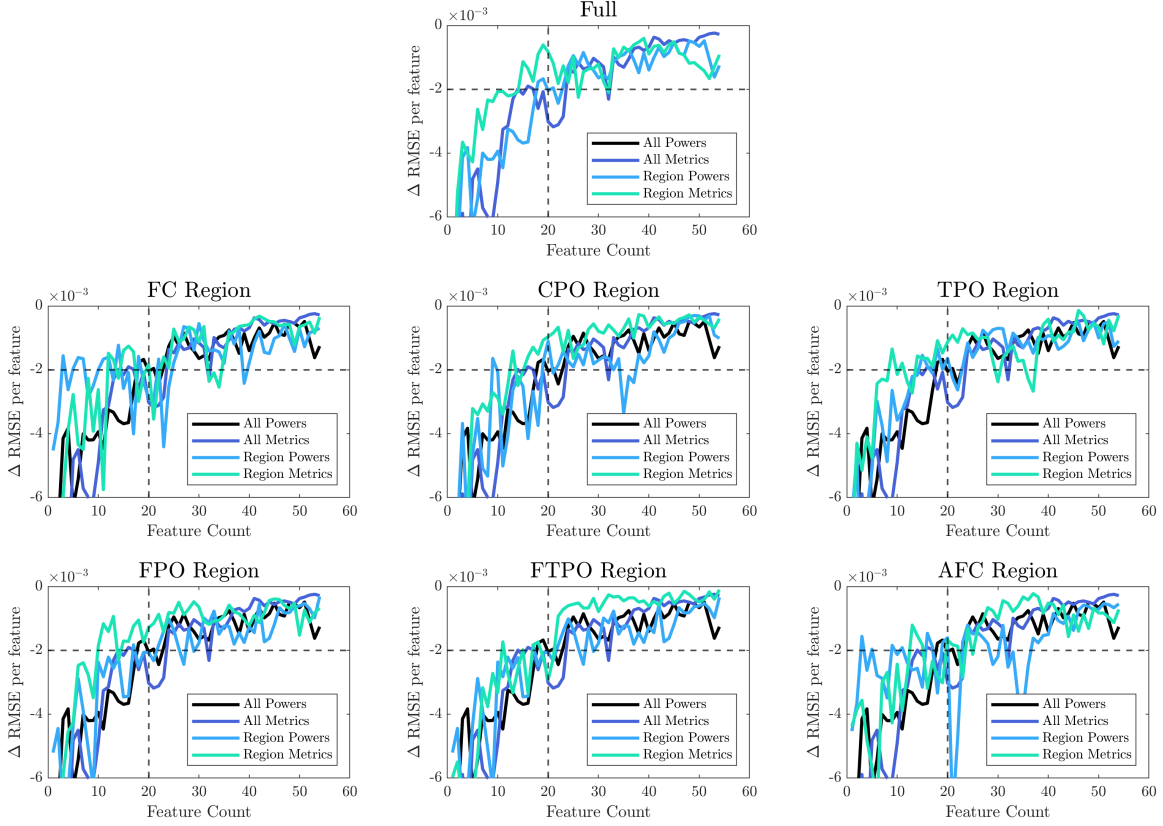
Figure 3.9: Detail of feature selection cutoff for each of the seven sub-regions in this study. The total number of regressors was set to 20.

3. Displacement Threshold: Select time points within a certain distance of the measured trust T_m

$$\left| T_m[n] - T_i^p \right| \leq \delta_T.$$

Finally, we combined the set of time points for each of discrete levels of trust to obtain the complete of discrete time points t^r:

$$t^r = \bigcup_{i=1}^{50} t_i^p$$

3.3.6   Model Generation

Our method of building and testing the performance of linear models was based on N-fold cross validation. We began by randomly assigning all sampled points to one of ten bins: $S = \{s_1, s_2, s_3, \ldots, s_{10}\}$. Each bin contained the same number of elements ± 1. We selected a 10% holdout, S_{test}, of data for testing while saving 90% S_{train} for model building. We
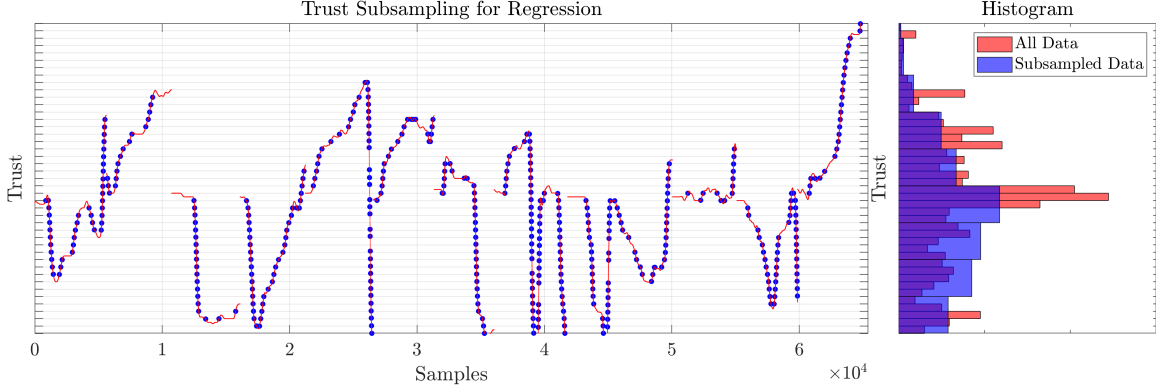
Figure 3.10: Sampling of the continuous trust for model construction. The ensemble of trust measures was separated into 50 discrete levels. Only points for which the trust was changing were used regression as described in Section 3.3.3.

built and evaluated each of the 14 models using the set $B = \{b_1, b_2, b_3, \ldots, b_n\}$ where $b_i = \{S^i_{train}, S^i_{test}\}$. Once a build and test sequence was completed, the results were tabulated, we defined a new set of 90% build and 10% test, then ran the process again. For a trust sample set of m total points, there are $n = \binom{m}{\frac{m}{10}}$ unique elements in B. We selected a subset of 1000 build and test sequences for our statistical analysis.

Models were built using the MATLAB function fitlm.m, and evaluated using the test and train sets in B for each of set of regressors. Prior to model construction, all trust and EEG data were temporally aligned and re-sampled to a frequency of 128 Hz using timeseries object functions in MATLAB.

3.3.7 Statistical Analysis

We compared model performance between the SC and NM feature types directly by subtracting the RMS trust prediction errors for each of the six sub-regions. Therefore, our test distributions were $\Delta E^k = rmse^k_{SC} - rmse^k_{NM}$ for each of the sub-regions k. Our hypothesis tests reduced to

$$H_0 : \mu_{\Delta E^k} = 0$$

$$H_1 : \mu_{\Delta E^k} \neq 0.$$

These hypotheses were evaluated using 2 sided t-tests.

3.3.8 Null Model Comparison

We created null network models to establish a baseline for comparative network behavior. The network densities were a direct result of the threshold we selected when binarizing our phase synchrony values as described in Section 3.3.1.1. Network density is given as the ratio of existing edges to the total number of possible edges, $d = \frac{e}{e_{max}}$. Consequently, we calculated the number of edges as $e = d\frac{N(N-1)}{2}$. We then constructed Erdős-Rényi [91] random graphs with the same node and edge count. Network metrics were calculated from the set of null graphs for comparison. Figure 3.11 illustrates such a random graph construction. Each row of the figure shows the adjacency matrix, approximate degree distribution, and edge locations on a head plot. The data graph contains clusters of high degree connections between frontal, parietal, and central regions. By comparison, the random graph has little noticeable structure, while still maintaining the same density as the data graph. The metrics calculated from both the data and random graphs are shown in the bottom plot. We can see the density values are approximately the same, as we would expect by construction, while the other metrics take on different values for each graph type.

Therefore, our test distributions were $\Delta M_i^k = m_{data}^k - m_{null}^k$ for each of the five metrics m_i and six sub-regions k.

$$H_0 : \mu_{\Delta M_i^k} = 0$$

$$H_1 : \mu_{\Delta M_i^k} \neq 0.$$

Statistical tests (2 sided t-tests) were performed to determine significance.

3.4 Results

3.4.1 Model Performance

We evaluated model predictive power between the SC and NM feature types using RMS trust prediction errors. Model parsimony and relative fit were evaluated using the adjusted R^2 [90]. RMS trust prediction errors are shown in Table 3.3. Adjusted R^2 values are shown in Table 3.4. Table 3.4 gives the ΔR^2 values for Hypothesis 1 as the R^2 of the Full
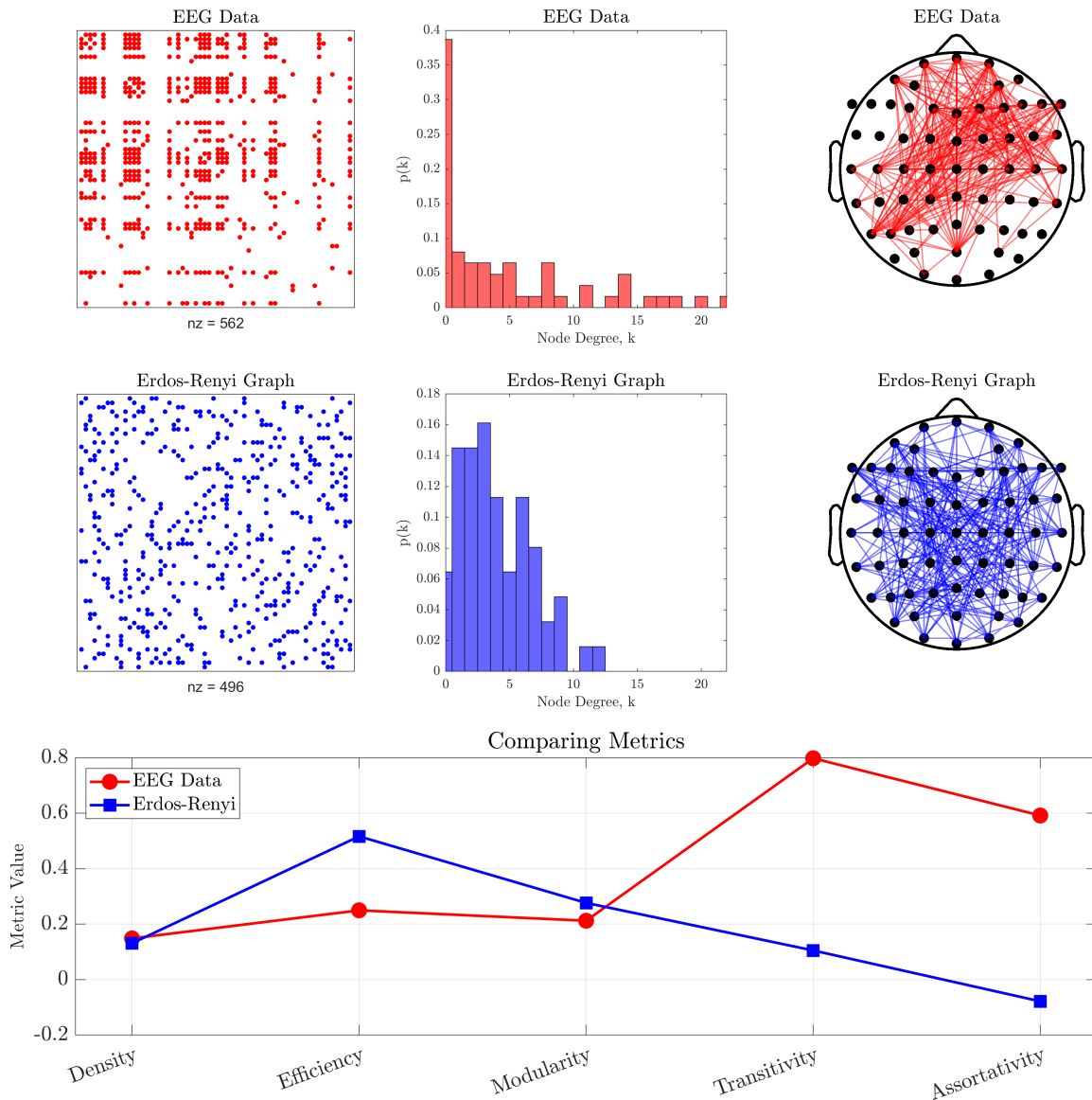
Figure 3.11: Generation of the Erdős-Rényi null network from data networks. Adjacency matrices and degree distributions illustrate the difference in null model topology. Network metrics determined from the null model diverge from those of the data network.

sub-region SC model minus the R^2 of each of the six remaining sub-region NM models. Therefore, $\Delta R_k^2 = R_{Full\_SC}^2 - R_{k\_NM}^2$ for each sub-region k. Details of the statistical tests are summarized in Tables 3.5 and 3.6. Difference in model error between feature types were given as $\Delta E^k = rmse_{SC}^k - rmse_{NM}^k$ for each of the 7 sub-regions. Therefore, negative values of ΔE^k indicated larger RMS errors for NM based models. As described in Section 3.3.5, measured trust ranged from 0 (no trust) to 1 (complete trust), $T_m \in [0, 1]$.

3.4.1.1 Adjusted R^2

All models using both SC and NM based regressors had adjusted R^2 values greater than 0.5 ($M = 0.667$, $SD = 0.071$). The largest value of adjusted R^2, 0.769, occurred with SC models built from the Full sub-region feature set. The next largest adjusted R^2, 0.735, was produced with NM features from the FTPO sub-region.

3.4.1.2 H1 RMS Error

Linear models using SC features showed lower RMS errors than models built using NM features for all seven sub-regions. The TPO sub-region yielded the greatest mean difference in RMS error with a value of -0.027, whereas the smallest mean difference was produced by the FTPO sub-region with a value of -0.005.

3.4.1.3 H2 RMS Error

Linear models using SC features generated lower RMS errors than models using NM features for three of the seven sub-regions investigated. The greatest positive mean difference in RMS error was produced by the FC sub-region at 0.079, whereas the lowest mean difference in RMS error was produced by the FTPO sub-region with a value of 0.004. The greatest negative mean difference in RMS error was produced by the TPO sub-region at -0.0148, whereas the lowest mean difference in RMS error was produced by the FPO sub-region with a value of -0.006.

Table 3.3: RMS Prediction Errors for Each of the SC and NM Regression Models

Sub-Region	Single-Channel		Network-Metric	
	μ_{SC}	σ_{SC}	μ_{NM}	σ_{NM}
Full Network	0.086	0.011	0.111	0.013
Frontal-Central	0.121	0.015	0.102	0.013
Central-Parietal-Occipital	0.088	0.011	0.101	0.012
Temporal-Parietal-Occipital	0.098	0.011	0.113	0.012
Frontal-Parietal-Occipital	0.095	0.011	0.101	0.011
Frontal-Temporal-Parietal-Occipital	0.095	0.011	0.091	0.009
Anterior-Frontal-Central	0.112	0.015	0.105	0.013

Table 3.4: Adjusted R^2 for Each of the SC and NM Regression Models

	R^2		ΔR^2	
	Single-Channel	Network-Metric	*H1*	*H2*
Region				
Full Network	0.769	0.607	0	0.162
Frontal-Central	0.530	0.670	0.099	-0.140
Central-Parietal-Occipital	0.753	0.676	0.093	0.078
Temporal-Parietal-Occipital	0.695	0.592	0.177	0.103
Frontal-Parietal-Occipital	0.714	0.671	0.098	0.043
Frontal-Temporal-Parietal-Occipital	0.714	0.735	0.034	-0.021
Anterior-Frontal-Central	0.566	0.650	0.119	-0.084
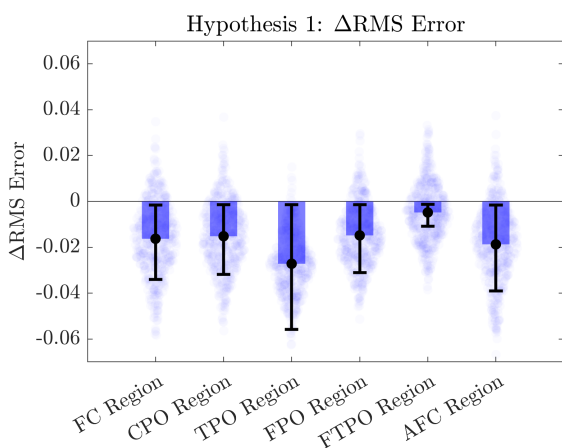
(a) ΔRMS Result for Hypothesis 1
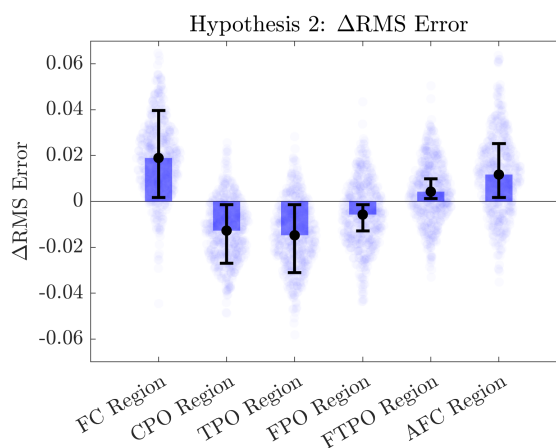
(b) ΔRMS Result for Hypothesis 2

Table 3.5: Statistical Results for Hypothesis 1

	H1: t-test for Equality of Means				95% CI	
Region	*t*	*df*	*p (2-tailed)*	$\Delta Mean$	*Lower*	*Upper*
Full	-32.80	998	1.10×10^{-160}	-0.0226	-0.027	-0.024
Frontal-Central	-21.17	998	1.78×10^{-82}	-0.016	-0.018	-0.015
Central-Parietal-Occipital	-20.51	998	2.78×10^{-78}	-0.015	-0.017	-0.014
Temporal-Parietal-Occipital	-36.90	998	1.10×10^{-188}	-0.027	-0.029	-0.026
Frontal-Parietal-Occipital	-21.17	998	2.02×10^{-82}	-0.015	-0.016	-0.013
Frontal-Temporal-Parietal-Occipital	-7.33	998	4.65×10^{-13}	-0.005	-0.006	-0.004
Anterior-Frontal-Central	-24.16	998	6.29×10^{-102}	-0.019	-0.020	-0.017

Table 3.6: Statistical Results for Hypothesis 2

	H2: t-test for Equality of Means				95% CI	
Region	*t*	*df*	*p (2-tailed)*	$\Delta Mean$	*Lower*	*Upper*
Frontal-Central	21.30	998	2.81×10^{-83}	0.079	0.017	0.021
Central-Parietal-Occipital	-17.50	998	5.48×10^{-60}	-0.0127	-0.0142	-0.0113
Temporal-Parietal-Occipital	-19.93	998	1.11×10^{-74}	-0.0148	-0.0162	-0.0133
Frontal-Parietal-Occipital	-8.125	998	1.31×10^{-15}	-0.006	-0.007	-0.004
Frontal-Temporal-Parietal-Occipital	6.47	998	1.54×10^{-10}	0.004	0.003	0.005
Anterior-Frontal-Central	13.01	998	2.77×10^{-36}	0.012	0.010	0.013

3.4.2 Feature Details

Figure 3.13 shows the details of all SC and NM features selected for the models in our studies. The headmaps illustrate the location of channels that generate SC features. Each plot describes the distribution of the particular features within the θ, α, β and γ frequency bands. The regions are differentiated by the shade of each bar, while their height indicates the number of features in the given band.

3.4.2.1 Single-Channel Powers

When selecting from the full compliment of 62 channels, the greatest number of features, 9 of the 20, were derived from channels positioned over the junction between the left temporal and parietal lobes. In addition, 5 channels were located over the frontal cortex, 2 were over the temporal lobes, one on the right, and the other on the left. There were 3 channels over the parietal lobe and two channels over the occipital lobe. SC features were distributed relatively evenly about the frequency bands. There were 5 features in both the θ and α bands. The β and γ bands contained 6 and 4 features respectively.

Channel selection for the remaining sub-regions were constrained to their particular channel subsets. We see that channels positioned over the right frontal lobe contributed the greatest number of SC features for the FC and AFC sub-regions. Feature sets for both the FTPO and FPO sub-regions were identical. Both the TPO and CPO sub-regions had a balance of channels between the left and right sides of the head. The four sub-regions that included channels over the frontal lobe had the greatest number of SC features in
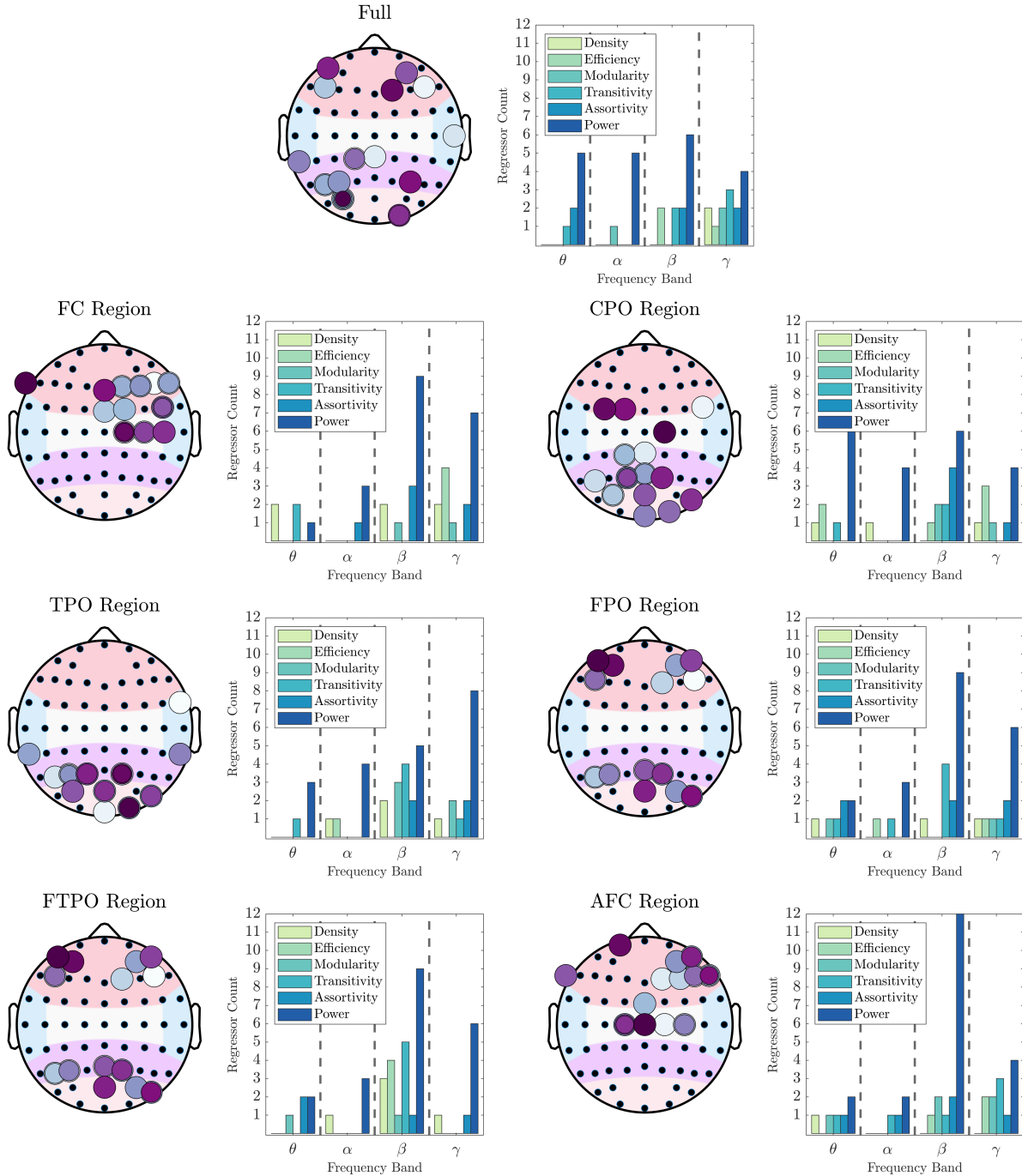
Figure 3.13: Detailed properties of the 20 features selected for our regression models. The location of single-channels are shown in the headmaps using colored circles. The distribution of regressors over traditional θ, α, β, and γ EEG analysis bands are located next to the headmaps for each of the 7 sub-regions.

the β frequency band. The CPO sub-region had the largest number of features located in the θ band while the TPO sub-region had the greatest number of features in the β band.

3.4.2.2 Network-Metrics

The frequency distribution of NM features were more uniform, with a tendency for a greater number of features located in the β band.

3.4.3 Network-Metric Values

The mean values of the 5 network metrics are summarized in Figure 3.14. Unlike Figure 3.13, features are lumped together by metric type. We see that the feature densities were approximately 0.1, efficiencies were 0.1 to 0.3, transitivities were 0.05 to 0.10, modularities were 0.4 to 0.6, and assortativities were -0.1 to -0.2. NM features derived from the Full sub-region had the highest values of efficiency, yet the lowest values of modularity when compared to the six other sub-regions.
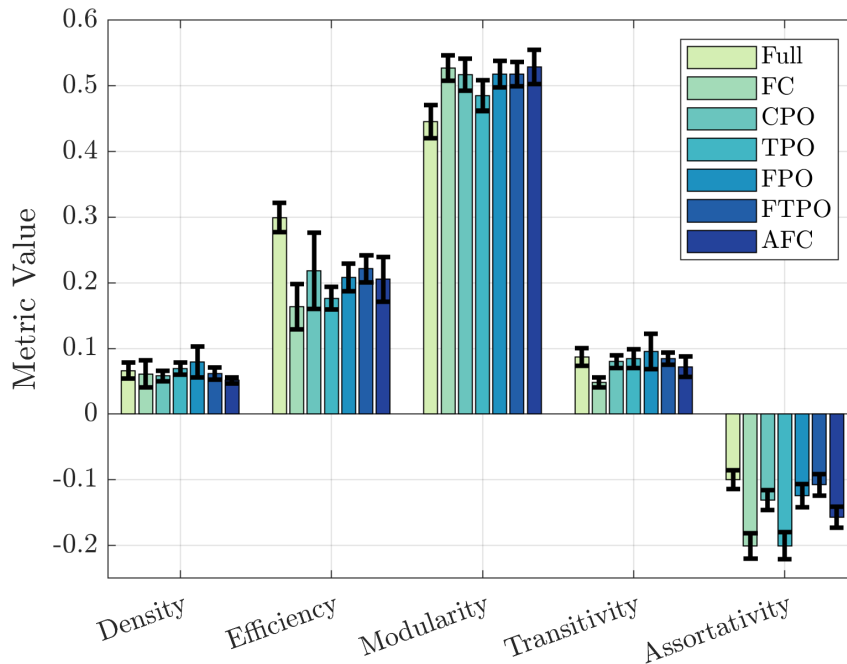
Figure 3.14: Comparison of the mean network-metric value for all seven sub-regions investigated. Value ranges for each metric type are described in Table 3.1

Details of the null model comparisons are shown in Figure 3.15. For brevity, we will refer to the networks derived from the EEG data as the data-networks and the corresponding random models as the null-networks. Each timeseries of data-networks has a corresponding sequence of null-networks. Network density and modularity are not included in the figure. By definition, the null-networks have the same number of edges and

nodes as the data-networks and hence, the same density values. Modularity is calculated by defining non-overlapping modules whose vertex allegiance differs the most from an equivalent Erdős-Rényi graph. The values in Figure 3.15 are given as $M_{null} - M_{data}$ where the metric M is either efficiency, transitivity, or assortativity. Figure 3.15 shows that differences in metric values between data and null networks were statistically significant for all seven sub-regions. Efficiency values were greater for null-networks, whereas the transitivity and assortativity values were greater for data-networks.
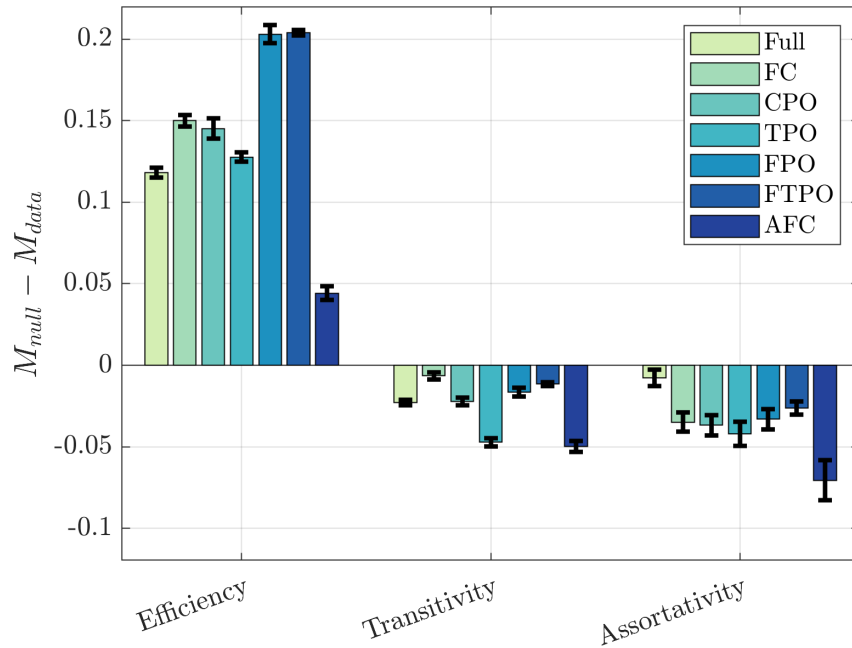
Figure 3.15: Difference in metric data versus null networks. Random networks are Erdős-Rényi graphs generated using the same node and edge count as the corresponding data network. Density and modularity are omitted in the comparison.

3.5   Discussion

EEG signal levels are indicative of neural activity. As described in Section 3.3.1.2, graph edges that form our networks are defined by the PS between channel pairs. Differences in relative phase that are stable over time is evidence of coherent interaction between brain regions. Brain regions that share the same power levels may still have random phase relationships that do not generate phase coherence. In our investigation, we do not examine the magnitudes of EEG power, but rather their correlation with changes in

trust. This differs slightly from a bulk of the existing literature that explore the activation and interaction of brain regions to relatively stable stimuli. Here we examine a dynamic process and select features based upon their ability to increase prediction in the dynamic changes in trust.

The network metrics selected for this study are neurophysiologically meaningful. However, their interpretation will vary based on the general topology of the specific networks. For example, in densely connected graphs, all nodes are topologically close and have a high degree of transitive closure. Consequently, the metrics of transitivity and efficiency become linearly proportional to density beyond a critical threshold [92].

3.5.1 Hypothesis 1

In this study we explore the question: "Are there sub-regions whose NM features contain more predictive information than all of the available SC features in the 62 channel EEG ensemble?" To evaluate this, we compare the performance of linear models constructed using regressors selected from the following feature sets: 1) single-channel powers from the complete 62 channel EEG headset, and 2) network-metrics defined for each of the seven sub-regions.

As shown in Table 3.5, models constructed using NM features from all seven sub-regions cannot outperform the models using SC features. However, our feedforward feature selection algorithm only adds regressors to the model that minimize the RMS error of the trust prediction. As described in Section 3.3.3, there are 1860 SC features but only 150 NM features. As shown in Table 3.2, the full compliment of available NM features spans only 8% of the SC feature space. The addition or subtraction of an channel changes the SC feature count by 30, one for each frequency in the time-frequency transform, yet has no impact on the number of NM features. There are simply not an adequate amount of NM features to build comparative models.

From Figure 3.13 we see the greatest number of channels are located in the temporal-parietal junction, a region that has been associated with changes in trust [93]. Additionally, 5 channels are located in the frontal cortex, a region primarily associated with working memory, executive planning, concentration, and emotion. The distribution

of the SC features in each frequency band is relatively uniform indicating that the particular position of the channels is more important that the frequency of the signal.

Of particular note is the FTPO sub-region which shows the lowest difference in RMS error and the highest adjusted R^2 among all NM models. This will be discussed in following sections.

3.5.2 Hypothesis 2

In this study we explore the question: "Do NM features defined on specific sub-regions contain more predictive information than SC features within that same sub-region?" To evaluate this, we compare the performance of linear models constructed using regressors selected from: 1) single-channel powers from the channels located within the seven sub-regions, and 2) network-metrics determined from each of those same sub-regions. In contrast with the previous study, the SC features in this study are only selected from the channels that make up the specific sub-regions. The number of channels for each sub-region is given in Table 3.2, and more importantly, the ratio of NM features to SC features.

There are three sub-regions that show statistically significant decreases in RMS error when using NM over SC features: FC, FTPO, and AFC. Each of those three sub-regions contain channels located over the frontal cortex. The FTPO sub-region also contains channels over the right and left temporal lobes, and the parietal and occipital lobes.

The FPO sub-region contains all of the channels within the FTPO sub-region with the exception of six additional channels located on the right and left temporal lobes. FTPO NM models outperform the SC models, whereas the FPO NM models do not, demonstrating that additional network connections from the temporal lobes to the frontal, parietal and occipital lobes increases trust prediction. However, the SC features for both the FPO and FTPO are identical. Therefore, the addition of the extra channels, while having no impact on their number, generates NM features that have better predictive power. Similarly, the FC sub-region contains all of the channels within the AFC sub-region with the exception of seven additional channels located over the anterior-frontal lobe. Both the AFC and FC NM models outperform SC models. Interactions within the

frontal lobe are known to contribute to cognitive activity.

3.5.3   Network-Metric Analysis

In Figure 3.14 we can see that the values of density, efficiency, modularity, and transitivity are relatively consistent between the six sub-regions. The assortativity values on the other hand show a much wider variation between sub-regions. The Full sub-region has the highest value of efficiency and assortativity as well as the lowest value of modularity. However, each of the metric values can be put into a comparative context when examining Figure 3.15. A comparison with the null-network metrics illustrates two key points. First, there are statistically significant differences between the metric values calculated on the data versus those calculated on random graphs for all seven of the regions in this investigation. Second, the direction of change illustrates how the topology of the data-networks deviates from that of a null-networks.

From Figure 3.15 we see that the efficiency of the null-networks is substantially higher, indicating that the mean path length of the data-networks is greater than that of the null-networks. The transitivity of the null-networks is lower, which indicates that the data-networks are more clustered than null-networks. The assortativity of the null-networks is also lower. Nevertheless, the assortativity values are negative in both the null and data networks. Negative values of assortativity imply that nodes of a low degree are more likely to connect to nodes with a high degree. This means that high degree nodes do not have a tendency to connect to other high degree nodes. A network that is relatively disassortative may or may not be less clustered, however, the removal of a single node is likely to have a greater impact the network topology.

The efficiency of the Full sub-region is most likely a consequence of the number of potential connections. A greater number of connections will reduce the mean path length between nodes substantially.

The greatest difference between the network efficiencies is seen in the FPO and FTPO sub-regions. This indicates that the mean path length between network nodes is larger. Both sub-regions have greater transitivity and assortativity than null-networks, but in relatively equal amounts.

The AFC sub-region has the smallest difference in efficiency. It also has greater transitivity and assortativity than the other sub-regions. This indicates that it has a higher tendency to cluster with a larger number of short connections between clusters. The FC sub-region on the other hand shows almost the opposite behavior.

3.5.4 The Impact of Feature Selection Method

In Section 3.3.3 we made the assumption that interactions between EEG features were negligible. Figure 3.16 shows the correlations between features for all of the sub-regions used in this study. The correlations between NM features for all sub-regions are zero mean with standard deviations of approximately 0.25 to 0.4. By comparison, SC features are predominately positively correlated with roughly 33% greater than 0.5, indicating that the are substantially more correlated than NM features.
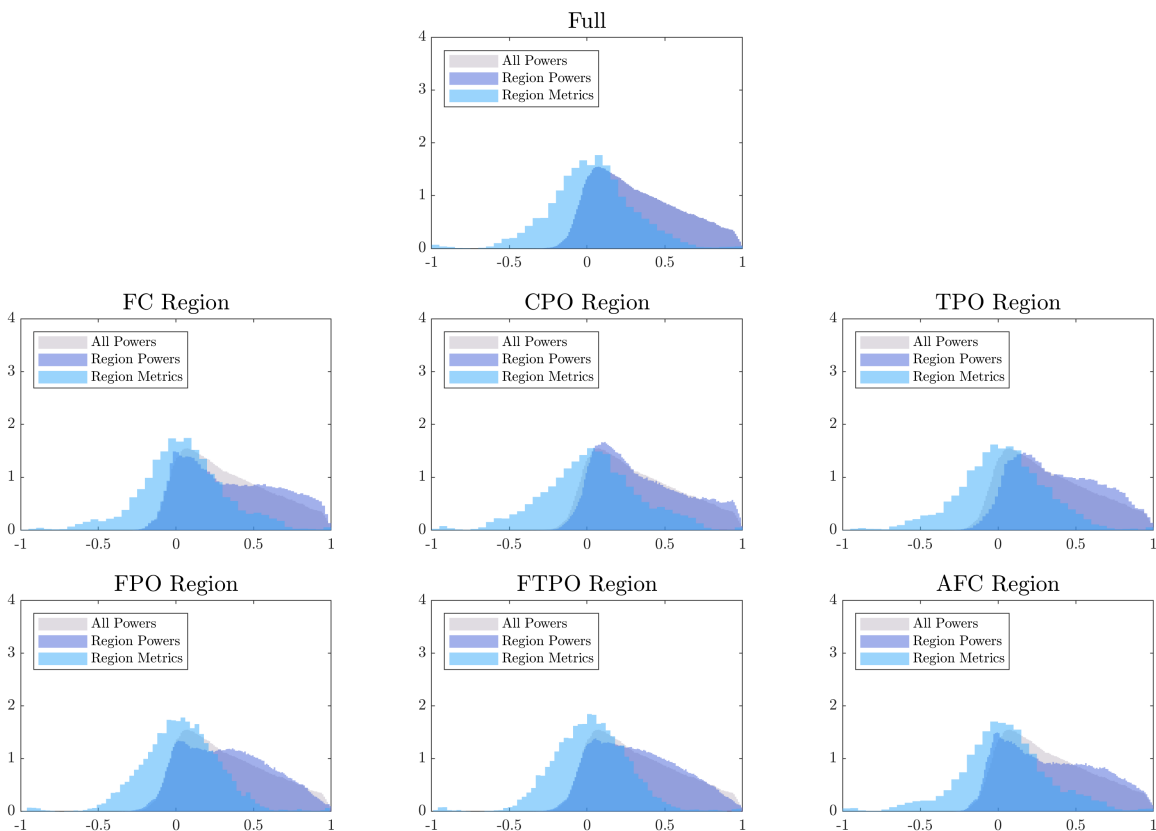
Figure 3.16: Detail of correlations between features. Single channel-features are shown to be significantly more correlated than network-metric features.

We utilized a greedy feedforward feature selection algorithm as mentioned in Section

3.3.4. This particular type of method yields some of the lowest RMS errors for given feature sets. However, it can do so at the cost of selecting features that are substantially parallel (highly correlated) to one another. A linear model with no interaction terms that is comprised of relatively correlated features can generate very unstable results if one or more of the features is removed or corrupted with noise. This may imply that NM based models can be more robust to channel loss.

3.5.5 Summary of Findings

The FTPO sub-region has the lowest change in RMS error among all of the region types. According to Table 3.4, the FC sub-region has the greatest decrease in adjusted R^2. FTPO adjusted R^2 is 0.735, whereas that of the Full sub-region is 0.769. In addition, FTPO RMS error is 0.091, relatively close to the Full sub-region RMS error of 0.086. Despite the greater relative performances of the FC and AFC sub-regions, NM features from the FTPO sub-region predict trust nearly as well as the single-channel features from the Full sub-region feature set. Again, there are significantly more regressors to choose from when using SC features, so it is impactful that the two feature types yield similar results. These results have been highlighted and emphasized in Table 3.7.

In summary, the FC and AFC sub-regions both outperform SC models with 20% and 16% of the number of potential features respectively, but they do so with different relative (to null model) values of transitivity, efficiency, and assortativity. The FTPO (12% feature ratio) also outperforms SC models, whereas the FPO (14% feature ratio) does not. However, both sub-regions have similar measures of transitivity, efficiency, and assortativity. These results have been highlighted and emphasized in Figures 3.17 and 3.18.

Whatever the cause of this difference, it is most likely not the quantity of extra channels but rather their location over the brain. Our results indicate that long range synchronous activity between the frontal and, occipital and parietal lobes may be indicative of changes in trust.

Table 3.7: Summary of Differences in Regional Performance

	R^2		ΔR^2		RMS Error		Δ RMS Error
	Single-Channel	Network-Metric			Single-Channel	Network-Metric	
Region							
Frontal-Central (FC)	0.530	0.670	-0.140		0.121	0.102	0.019
Frontal-Parietal-Occipital (FPO)	0.714	0.671	0.043		0.094	0.101	-0.006
Frontal-Temporal-Parietal-Occipital (FTPO)	0.714	0.735	-0.021		0.094	0.091	0.004
Anterior-Frontal-Central (AFC)	0.566	0.650	-0.084		0.116	0.105	0.012
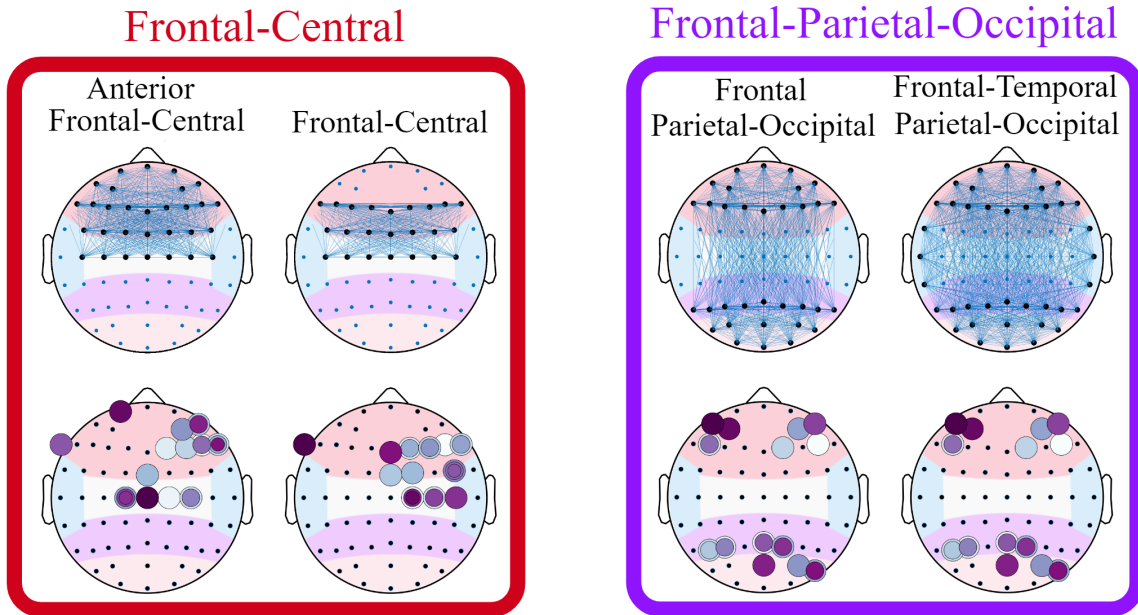
Figure 3.17: Frontal-Central sub-regions and Frontal-Parietal-Occipital sub-regions for direct comparison of single-channel locations and topological distributions of network edges.

3.5.6 Implications and Future Work

We have shown that meaningful patterns may be found within the elicited responses of a small number of participants, and support the proposition that EEG features can capture cognitive activities that correlate with trust. However, we did not set out to determine if a specific metric, bandwidth, or combination of metrics would generalize as a robust trust measure for a wider cohort, which would require a significantly broader study. A wider investigation could also explore the trade-off between feature stability and model performance. The removal of certain nodes could have a significant impact on metric values dependent upon their relative importance within the network topology. This type
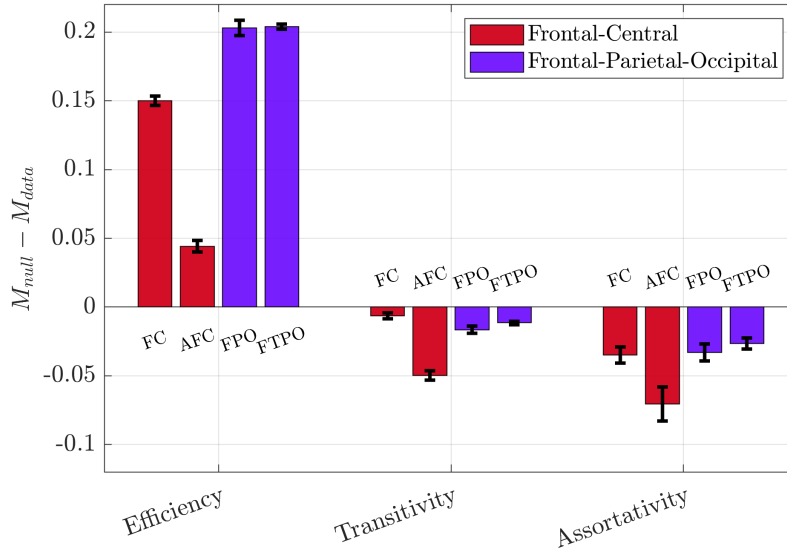
Figure 3.18: Direct comparison of the difference in null centered metrics as previously shown in Figure 3.15. The values for the Frontal-Central regions, shown in red, are rather close, while the values for the Frontal-Parietal-Occipital regions, shown in purple, are rather separate.

of investigation could only be performed by studying the topological significance of specific nodes using granular measures such as centrality or local efficiency [92].

Our results indicate that the topology of interactions not only within the frontal network, but also between the frontal, temporal and parietal regions are effective at predicting trust in autonomy during human-autonomy team tasks. In addition, research in the field of cognitive neuroscience has found evidence to suggest that cognitive control capacity may be supported by whole-brain network properties and that dynamic network features may contribute to differences in goal-directed behavior [29]. Consequently, the use of network metrics can provide neuroscientific insight into the nature trust in human-autonomy team tasks.

3.6 Conclusion

In this chapter we describe the results from our experiment in human-autonomy trust. We elicited changes in human trust in a simulated autonomous system while recording cognitive activity using an EEG measurement system. Human subjects were instructed to report changes in trust throughout the experimental trials. We constructed linear

regression models to predict changes trust using two types of features derived from the EEG timeseries: 1) Single-electrode signal powers; 2) EEG inter-electrode functional connectivity network-metrics derived from signal phase synchrony.

Our results indicate that the two types of EEG features can capture cognitive activities that correlate with trust. A comparison of model performance between single channel powers versus network metrics, both defined from specific brain regions, shows that network metrics outperform the single-channel powers for three of the seven sub-regions investigated. Both single-channel powers and network-metric that incorporate the frontal, parietal, and occipital lobes of the brain have the greatest impact on trust prediction.

3.7 Acknowledgment

Chapter 4

Investigating Human Behaviors in a Manual Grinding Task

Preface

In this chapter I present our experiment involving human behaviors of skilled practitioners in a manual grinding task. In Chapter 1 we explained that human's are required to be "in-the-loop" for many human-autonomy team tasks because they can apply their knowledge and expertise. The types of expertise depend entirely on the specific task. This experiment was performed in concert with Jayanti Das of the UC Davis Manufacturing and Sustainable Technologies Research (MASTeR) Laboratory overseen by Dr. Barbara Linke. The study was motivated by the fact that human manual expertise is not well digitalized for many applications. This particular study examines the behaviors that differentiate individuals of different skill levels when performing a manual task. When this experiment was conducted, we did not have access to an EEG device. Consequently, the variations in human cognitive state associated with task performance were not available for analysis. Nevertheless, goal directed behavior can be a key measure of cognitive state as mentioned in Chapters 1 through 3. If EEG data had been recorded, our analysis would have included the correlation of EEG measures with behaviors and performance: an excellent prologue study to the experiment presented in Chapter 2. Nevertheless, the results from this experiment are novel in their own right, and have been included in this dissertation.

The major contributions of this chapter are as follows: 1) We quantitatively characterize manual behaviors by comparing joint gaze-motor data. To our knowledge,

this chapter presents one of the first instances in which visual attention has been studied in manufacturing scenarios; 2) We examine the relationships between applied grinding forces and surface integrity with respect to these behaviors, and the experience level of the practitioner. We are able to show that there are distinct behavioral and performance differences between subjects of different experience levels. Adept hand eye coordination is key to the performance of a number of manufacturing processes. Due to the importance of gaze-motor behavior, our results can be generalized to gain insight into a wide range of industrial activities such as welding, repairing machinery, grinding and polishing during abrasive finishing process, or everyday activities like driving.

The contents of this chapter have been previously published in [38], [39], and [40].

4.1 Introduction

In the age of cyber-manufacturing, research has increasingly focused on establishing intelligent processes which will enable the effective communication between humans, machines, and products in complex production environments. Within this new infrastructure, an understanding of human performance is critical if they are directly involved in product generation. For example, the quality of manual abrasive finishing operations such as grinding, polishing, and engraving are heavily dependent upon the performance of the individual operator. These manual sectors represent a growing market, from foundry shops to the aerospace industry. The skills involved in these manual tasks are largely procedural rather than declarative, meaning that they cannot be easily articulated by the individuals [94]. Furthermore, a lack of understanding of these manual skills may prolong the transfer of this knowledge from one generation to the next. It may also impede the development of efficient collaboration between humans and smart machines [95] which can greatly impact the product outcome [96, 97]. If we wish to integrate humans into the manufacturing network and effectively train them, we need to digitalize their behavior/performance. A first step in this process is the

development of a formal models which capture the process properties, behavioral characteristics and techniques of the practitioners. Such models would allow the optimization and integration between person to person, person to machine, and person to tool within the manufacturing network [98].

A crucial issue for manual grinding operation is a critical understanding of fundamental cutting mechanisms. Manual grinding operations are effectively force controlled processes rather than automated path controlled operations. The applied forces are influenced by several factors, which include the gripping force of the user, personal skill level, and cutting tool feed rate [99]. Extensive research has focused on different automated grinding processes and has characterized the influence of process control parameters such as material removal rate, grinding force, wheel structure topography, etc. [100, 101]. Unfortunately, very little work has been carried out to investigate manual grinding operations and process optimization, and to correlate the experience level of the worker to asses process performance quality. Kyle et al. [102] described the input-output streams of a manual grinding process, reviewed sustainability aspects of the energy sources of abrasive power and grinding tools, and discussed concerns related to the safety and health aspects of manual operations. Along with other process parameters such as feed rate, cutting speed, and workpiece materials, the skill level of the practitioner plays a critical role in product performance and process optimization.

It has been stated that the resultant tangential and normal forces from manual grinding operations have an impact on process parameters such as material removal rate (MRR), surface integrity (e.g. average roughness), and control process performance [103]. Thus the efficiency of manual grinding operations are largely dependent on judicious control of applied forces and become a function of the experience level of the practitioner, MRR, average roughness etc. However, little work has been done to investigate the impact of manual grinding forces on process performance (i.e. in terms of MRR and surface roughness) based on experience level. We shall explore the performance of manual grinding operations by examining normal and tangential forces, the experience of the user, material

removal rate, and surface integrity in addition to visual-attention-motor behavior.

Visual attention is a remarkable human capability of reducing the huge amount of visual data entering our eyes into a manageable level. It is widely accepted that visual attention is not decoupled from motor system in natural behavior [104–107]. In the majority of studies concerned with visual attention and the motor system, actions are discrete, e.g., "remove the lid of the kettle" and "select a peanut butter jar" [104, 106], and manually labeled by humans. Such a representation fails to capture the complex nature of gaze-motor behavior. Data on motor dynamics, such as the changes in forces, were not collected and subsequently studied. A analysis that captures the dynamic nature of motor behavior is needed, similar to those developed in [108, 109].

4.2   Experiment

In this section, we describe the setup and procedure of our manual grinding experiment.

4.2.1   Setup

For the purpose of studying manual skills involved in grinding tasks, we recruited four students from the Department of Mechanical and Aerospace Engineering at the University of California, Davis. All subjects were between 20 to 25 years of age. The subjects were chosen based on their differing levels of experience. For this study we have subjectively defined experience as the amount of time each subject has spent with grinding tools. In the subsequent sections, the "experienced" subject shall be referred to as Subject 1, the "intermediate" subjects as Subject 2 and Subject 3, and the "novice" subject as Subject 4. Each subject performed ten trials in which they were asked to use an abrasive wheel to grind a metal sample. As shown in Figure 4.1, three streams of data were collected. First, we measured the direction of gaze with a head mounted eye tracking system. Second, the grinding forces were measured with a triaxial load cell mounted beneath the grinding sample. Lastly, the 6 DOF kinematic state of the grinding tool and the eye tracking glasses were recorded using an optical motion tracking system.

We measured gaze using a wearable eye tracking system manufactured by SensoMotoric Instruments (SMI). The SMI ETG 2w system is integrated into a set of
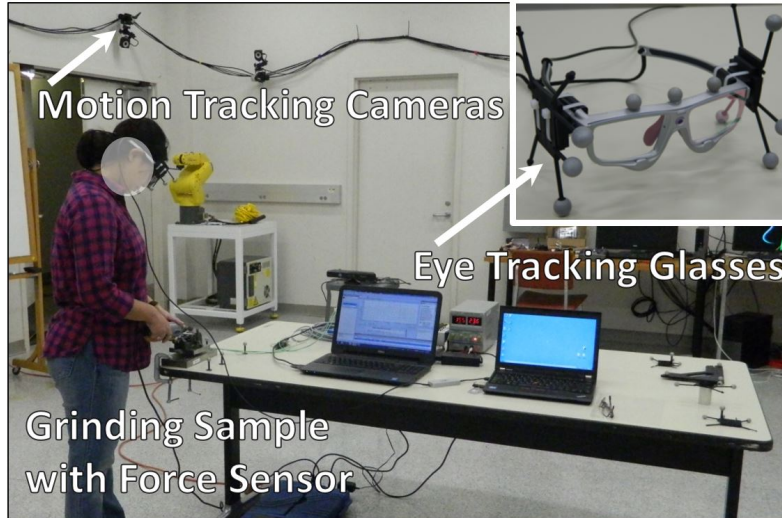
Figure 4.1: Setup of our grinding experiment. Data were collected from three separate modules: 1) gaze tracking consisting of SMI eye-tracking glasses and a computer running iView recording software; 2) force measurement consisting of a triaxial load cell and a computer running LabVIEW; 3) motion capture system by Optitrack, which can determine the position and orientation of selected objects. The data collected from these three modules were synchronized and analyzed using the methods described in Section 4.3.

glasses which can extract binocular gaze, while simultaneously recording a video of the visual point of view. Pupil images and corneal reflections are used to determine the vertical and horizontal angular orientation of each individual eye, which in turn are used to calculate the gaze. True gaze direction requires a vector to describe its full nature. In our analysis, the gaze data were represented as binocular points of regard (BPOR). These points describe where the binocular gaze vector pierces the gaze plane, a hypothetical projection plane located 1450 mm in front of the glasses. The BPOR were sampled at 60 Hz, and the gaze was presented as their pixel positions within the video image. Videos were recorded at 60 frames per second at a resolution of 1280 pixels horizontally and 960 pixels vertically.

The material used in this study was 6061 aluminum in the form of test coupons with dimensions of 5.0 cm in length, by 2.5 cm in width, by 2.5 cm in height. Each grinding experiment was conducted with a Dremel 4000 hand held power tool using alumina sanding bands of 60 grit sizes (mesh number). The power tool was running at a constant
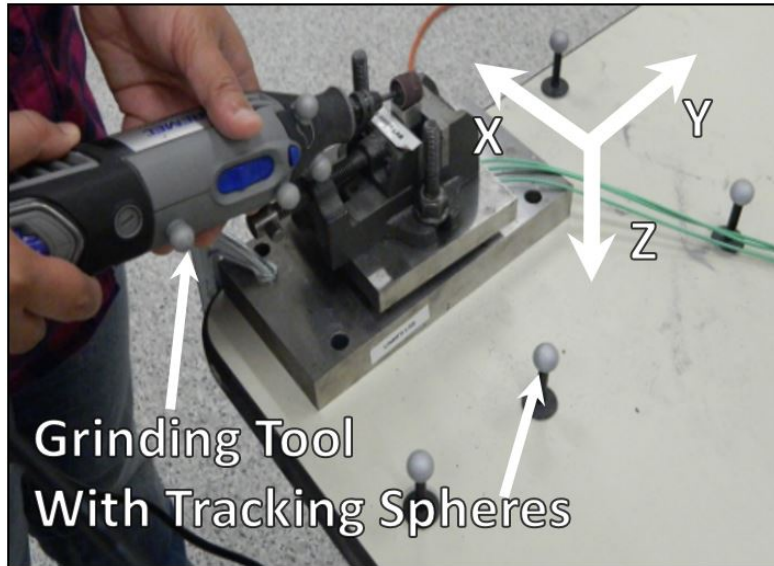
Figure 4.2: Detail of the grinding sample and force data collection module. Forces in three directions were measured, tangential (x-axis), normal (z-axis) and axial (y-axis). The reflective spheres are used by the motion tracking system.

speed of 5000 rpm. All grinding operations were performed under dry cutting conditions. The grinding force was varied manually which produced force variations in the tangential, normal, and axial directions as shown in Figure 4.2. A piezo-electric transducer based load cell (Kistler 9252A) was mounted under the workpiece to measure these grinding forces during machining. A vise was used to fasten the workpiece to the sensor. Force data were sampled at 1000 Hz using a National Instruments DAQ and Labview software.

Finally, we obtained the kinematic data using a motion capture system by Optitrack. This system consists of twelve cameras mounted circumferentially along the walls of our lab. These camera modules each contain a ring of infrared (IR) light emitting diodes which project a cone of IR light into the lab space. The eye tracking glasses, and the grinding tool were each defined as a rigid body by marking them with a series of reflective spheres as shown in Figure 4.1 and Figure 4.2. The overlap of the IR cones establish a tracking volume in which the position of these markers are determined at <1mm accuracy. From these marker positions, the Optitrack software can extract the 6 DOF pose estimation of each rigid body. Data was sampled at 120Hz.

4.2.2 Procedure

The experiment proceeded in the following manner:

1. Before each grinding trial, a calibration step was carried out in order to collect the particular ocular behaviors of the subject using a method is described in [110].

2. Light touched crosshatched marks were made on top of workpiece surfaces. The subjects were asked to grind the surfaces until the marks were no longer visible.

3. The gaze, force, and kinematic data were collected and saved separately for each trial, and each subject.

4. Both the grinding wheel and the grinding sample were replaced after each trial.

5. The mass of the sample was recorded before and after each grinding trial to determine the amount of mass removed.

6. Average surface roughness was measured and recorded after each grinding trial.

7. Each subject performed ten trials.

4.3 Data Processing Methods

In this section we describe our basic data processing methods.

4.3.1 Time Alignment and Filtering

All data from the three individual streams had to be temporally aligned, buffered, and filtered for a comparative analysis. The data analysis was performed in Matlab.

The force and kinematic data were post-processed with a 8t h order Butterworth low pass filter at a corner frequency of 20Hz. Normal and axial force data were particularly noisy necessitating the use of such an aggressive filter to extract characteristics at the lower frequencies. Filtering was accomplished using a bidirectional, zero lag implementation of digital filters.

4.3.2 Scanpath

Gaze can be characterized macroscopically by two unique states: fixation, and saccade [111]. Visual information is extracted during fixations, which are periods of relatively small angular movement of the eye. Transitions between fixations take place

through the rapid eye movements known as a saccades. A scanpath is the trace of eye movements in space and time [112–116]. It is a locus of fixation points (x, y, t) which describe when and where the subject attends to a particular visual stimulus. Each scanpath is a distillation of true eye movement, which is complex and continuous. The particular choice of presentation of this data varies by the type of analysis. Among these presentations, the most common consists of plotting the x and y coordinates of each fixation point onto an image of the visual stimulus [116]. The duration of the fixation is illustrated using a circle with a diameter proportional to the amount of time. An example scanpath of one subject and one trial is shown in Figure 4.3.
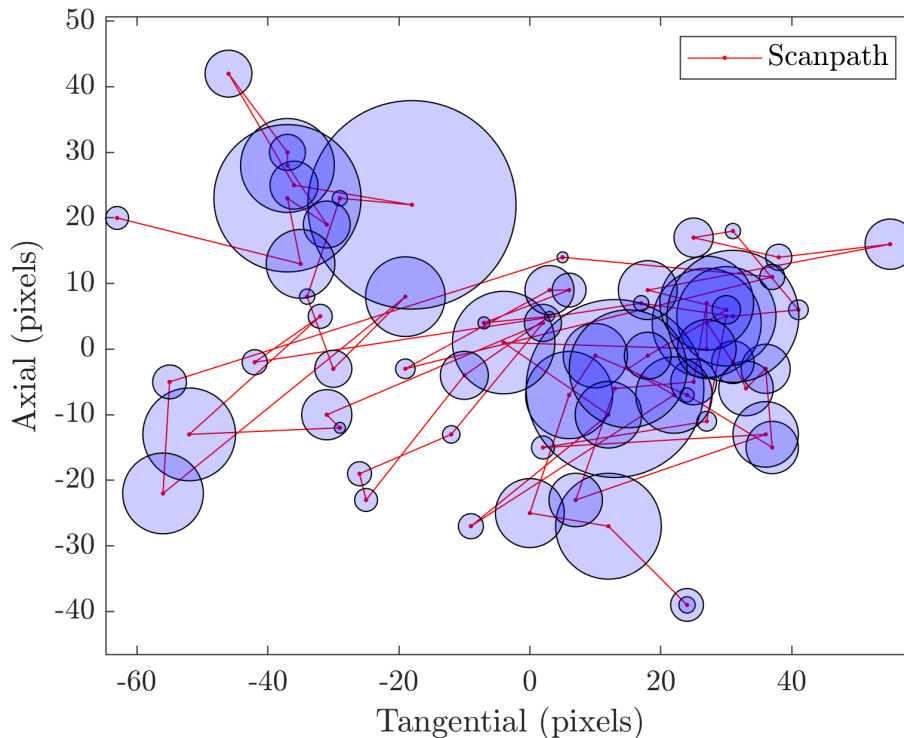
Figure 4.3: An example scanpath. The centers of fixations are denoted by points. The durations of fixations are represented by the diameters of the circles. The fixation centers are connected by straight lines according to their temporal order. Each straight line corresponds to a saccade.

There are several techniques used to generate the scanpath, each of which depend on the particular method to identify and label fixations and saccades. Many popular methods are outlined in [117]. The methods can generally be broken down into two main types; area/dispersion based methods which rely on the spatial distribution of the BPOR onto

an image of the visual stimulus, and velocity based methods which utilize the angular velocity of the eye. Area/dispersion based methods are widely used in print based studies to compare regions of visual interest, especially in test scenarios in which the subject's head is fixed, or nearly fixed. Velocity based methods analyze the distribution of the angular motion of the eye itself. It is generally accepted that the eyes cannot move faster than a given speed; usually $900°$ per second. It is also generally accepted that saccades are defined by shifts that occur above certain speeds. Furthermore, the human attention system cannot interpret complex visual stimuli lasting for a duration of less than 100-200ms [116]. This makes the velocity based methods more attractive as they can be made to adhere to such physiological constraints. In addition, our subjects are free to move their heads as they chose, making a velocity based method the only viable option.

In order to generate our scanpaths, we extracted fixations from the time history of the BPOR using a methodology outlined in [118]. We have found this method to be flexible enough to work well at our sampling rate of 60 Hz, yet robust enough to extract saccades even in the presence of noise. It estimates a saccade as a peak in the angular velocity of the eye which occurs above a threshold determined from the statistics of the data. These data may have measurement noise from periodic occlusions of the pupil, or more often, may represent eye movements that are naturally more jittery.

Before calculating our scanpaths, we first condition the raw gaze data using a Savitzky-Golay filter to calculate the angular velocities eye $\dot{\theta}$, and remove points with unusually high velocity ($>900°$/sec). These points are most likely due to the inability of the eye tracking system to properly image the pupil. Next, we remove any remaining points located at the origin (as a result of blinks or loss of pupil tracking) and those points located outside the data window. Approximately 1-5% of the BPOR data must be removed for these reasons. Finally, we interpolate between the removed points.

We prime the estimation algorithm by choosing some initial peak velocity threshold $\dot{\theta}_{init}^{PT}$ that is greater than the maximum velocity in the data, and define the set used in the first estimation as $\omega_1 = \{\omega \in \dot{\theta} \mid \omega < \dot{\theta}_{init}^{PT}\}$. Next, the estimation process iterates until the exit threshold is reached (Step 4). The ith iteration is described below.

1. Calculate the mean and standard deviation of ω_i, as μ^{ω_i} and σ^{ω_i}.

2. Define a new peak velocity threshold $\dot{\theta}_{i+1}^{PT} = \mu^{\omega_i} + 6\sigma^{\omega_i}$

3. Define the new set $\omega_{i+1} = \{\omega \in \dot{\theta} \mid \omega < \dot{\theta}_{i+1}^{PT}\}$.

4. If $\mid \dot{\theta}_{i+1}^{PT} - \dot{\theta}_i^{PT} \mid < 1°/\text{sec}$, then the final threshold is $\dot{\theta}_F^{PT} = \dot{\theta}_{i+1}^{PT}$ and the angular velocity of the onset and offset as $\dot{\theta}^o = \mu^{\omega_{i+1}} + 3\sigma^{\omega_{i+1}}$, else return to step 1.

Once we have determined the velocity threshold, we extract the peaks in angular velocity data, which is essentially the set that satisfies $\omega_{peak} = \{\omega \in \dot{\theta} \mid \ddot{\theta} = 0\}$. Saccades are defined in the angular velocity data as $\dot{\theta}_{sac} = \{\omega \in \dot{\theta} \mid \omega_{peak} > \dot{\theta}_F^{PT}, \omega_{peak} - \dot{\theta}^o \leq \omega \leq \omega_{peak} + \dot{\theta}^o\}$. Any part of the signal that is not a saccade is categorized as a fixation. Depending upon the subject, approximately 5-8% of fixations are less than 100 ms, and must be discarded. Finally, we calculate the mean value of the position of the eye (in pixels) for each fixation. The resulting vector tuple is the (x, y, t) elements of the fixation.

The objective comparison of scanpaths depends heavily on both the task, and the visual stimulus. A detailed review of many of these comparison methods are outlined in [116]. In our particular study however, the comparison is vastly simplified. We included the vertical marks on the test sample to force a visual engagement with the workpiece. As a result, the scanpaths evolve in a manner analogous to a reading task in which the visual stimuli, the words, are generally examined serially from left to right. We know that a subject is likely to attend to the words on the page and in a specific order. Similarly, since our grinding task is limited to the surface of the small test coupon, we can assume that the subjects are likely to spend the majority of time searching vertically and horizontally. Therefore, the difference in gaze behavior becomes how often, and at what magnitude does their gaze shift across the test sample.

4.3.3   Process Parameters

In order to determine process parameters for direct comparison of product performance, material removal and average surface roughness were measured. A white light interferometer confocal microscope CSM 700 from Zeiss was used to measure all 2D and 3D surface roughness parameters with a cut-off length of 0.8 mm and an evaluation

length of 4 mm (in accordance with ISO 4287:1997). A weighing scale was used to measure mass of workpieces before and after each grinding for each subject.

4.4 Results and Discussion

In this section, we compare the behavioral characteristics between subjects. We examine the duration of fixations, the variance of fixation positions, the characteristics of the applied forces, and identify general relationships between the eye movement, grinding forces, and tool velocity. We then compare process performance variables (MMR) and part quality (average surface roughness) resulting from the grinding operation. Finally, we discuss how the differences in gaze-sensorimotor behavior, are related to process performance and part quality via technique, which is a crucial element of the experience level of the subject.

As noted earlier, we shall refer to the experienced subject as Subject 1, the intermediates as Subject 2 and Subject 3, and the novice as Subject 4. Furthermore, for the purpose of direction consistency, we will refer to the x direction of the gaze as tangential and the y direction as axial.

4.4.1 Tool Velocity

For this particular study, the addition of the motion tracking system allowed us to directly measure the position and orientation of the tool. Figure 4.2 provides a detail of the Dremel tool with the tracking spheres attached. Velocities were calculated by a simple numeric differentiation of the filtered position measurements. The velocity vector was decomposed into the relevant axes: tangential (x), normal (z), and axial (y) as shown in Figure 4.2.

In order to directly compare the velocity characteristics of each subject, the absolute value of the signals were binned and normalized. These results are shown in Figure 4.4. Despite the fact that this grinding task was primarily tangential in nature, several of the subjects displayed interesting variations in their axial motion. A close examination of the curves in Figure 4.4 shows that Subject 2 and Subject 4 show a large tangential response between .06 to .1 m/s, as we might expect. However, Subjects 1 and 3 have low variance in both the axial and tangential directions indicating that their hand motions contained

(a) Subject 1

(b) Subject 2

(c) Subject 3
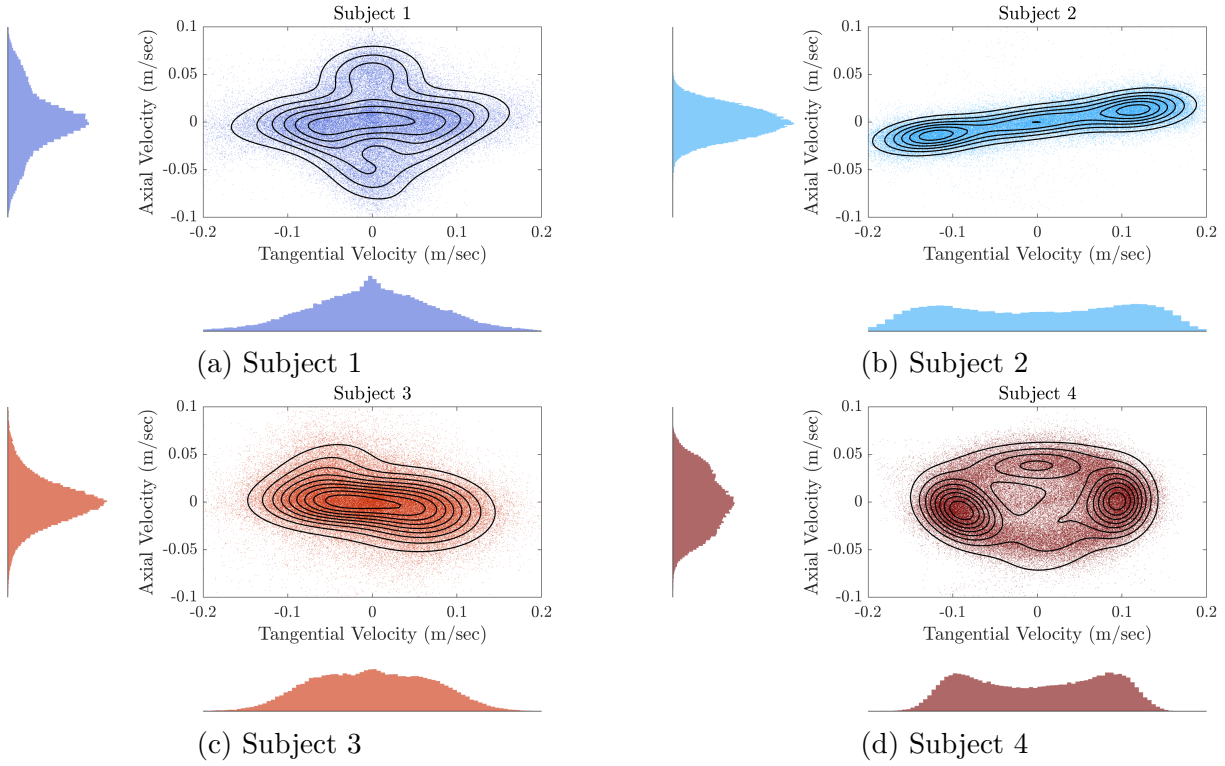
(d) Subject 4

Figure 4.4: Normalized histogram of the tangential and axial tool velocities for all subjects. Contour lines highlight the structure of each distribution.

a fair amount of axial motion. In fact, both of these subjects tended to utilize a swirling motion over the workpiece rather than a standard back and forth sweeping of the tool. These differences in technique are embodied in the remainder of the behavior data.

4.4.2 Gaze Analysis

Fixation duration is simply measured as the time lapse, in seconds, between two saccades. A two sample t-test and a chi-squared test were performed on the fixation data. These tests both indicate that trials between subjects are statistically different ($p < 0.03$), while the data within each subject are not. This is plausible as we may guess that the fixational characteristics are an inherent property of the individual subjects. As a result, we pooled the data for each subject across all ten trials.

The pooled distributions as illustrated in Figure 4.5 are highly skewed. A direct comparison between the subjects shows that Subject 1 and Subject 3 have much shorter
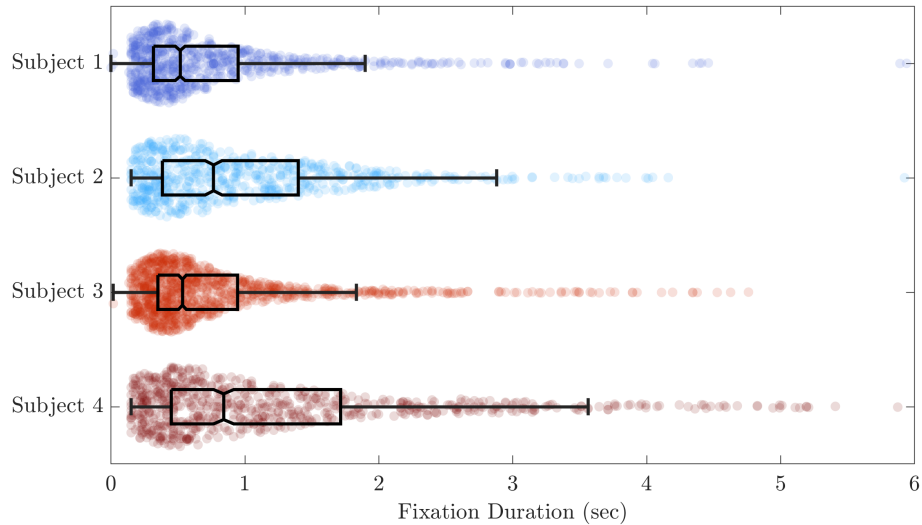
Figure 4.5: Comparison of fixation distributions between subjects. Whiskers extend out to the 90th percentiles.

durations than Subject 2 and Subject 4, which indicates that their eyes are moving about the workpiece more frequently. Furthermore, Subject 1 shows the smallest variance, with few durations lasting longer than 2 seconds. By comparison, Subject 4 has the largest variance of the all subjects with some fixations lasting as long as 4 seconds, more than twice that of Subject 1.

We can invert these fixation duration data in order to obtain a distribution of fixation frequency as shown in Figure 4.9. This method to effectively display the data for comparison with the spectral distribution of the tangential forces and velocities.

A typical set of fixations for a single grinding trial are illustrated in Figure 4.6. We determine the variations as follows: First, the mean for each trial is calculated. The variation is defined as the square root of the squared difference of the gaze position from the mean for each fixation. Thus it is not the variance of a distribution, but the absolute value of the distance of each fixational point of regard from the mean of each particular trial. These data are presented as pixels in the image frame (1280 horizontal by 960 vertical). These data are binned and the distribution of each subject for each trial is plotted in Figure 4.7. Since this particular task is performed by moving the tool from side to side, we would expect that the fixational shifts would be larger in the horizontal (x) direction than the vertical (y). This appears to be true with Subjects 2 and 4, with

the novice subject exhibiting the largest horizontal shifts. Interestingly, Subject 1 and Subject 3 both have tendencies to look vertically more than horizontally corresponding to a shifts in attention in that direction. This corresponds to the more complex motions that were exhibited by these subjects.
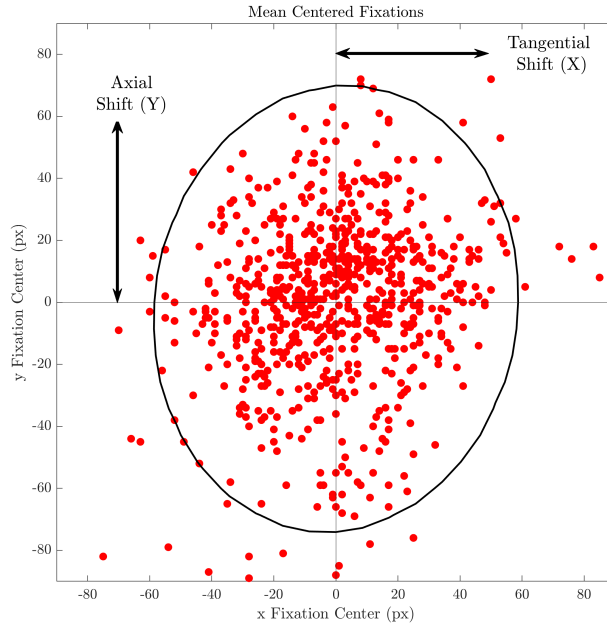
Figure 4.6: Sample of fixation points for a single subject. Positions are reported in pixels on the original 1280 by 960 pixel field of view. Notice the asymmetric dispersion of shifts.
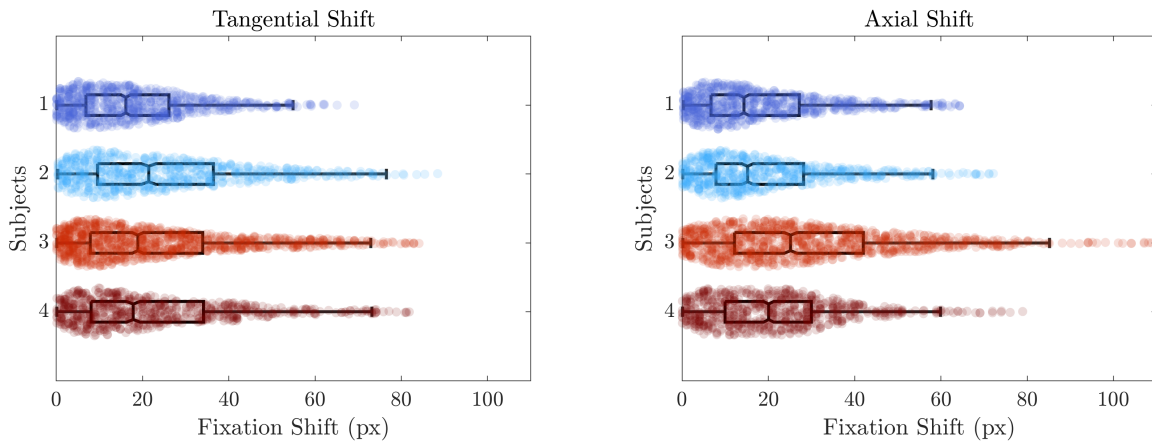
Figure 4.7: Distributions of the fixational variations for all the trials. The whiskers extend to the 90th percentile of the distribution.

4.4.3 Grinding Forces

Figure 4.8 illustrates the normal versus the tangential forces for a single trial of each of the four subjects. While the normal forces might be considered those that are directly applied by the subject, we can see that there is a strong correlation between the tangential and normal forces (r^2 between .65 and 0.85 for all subjects). Furthermore, the tangential force is an indication of grinding power as the greater the magnitude, the more energy involved in the material removal [102] and therefore more relevant to process performance. Finally, the variability in the distributions of the tangential forces between subjects were large enough to analyze statistically. Therefore, we chose to include the tangential rather than normal forces in our comparative analysis.

While the different subjects operated in different force regimes, it is clear from Figure 4.8 that the mean value of the forces produced by Subject 2 were the highest, while those from Subject 1 were the lowest. More importantly however, the mean and variance in both the normal and tangential forces for both Subject 2 and Subject 4 are very large compared to the others, indicated a general tendency to push the tool harder into the workpiece.
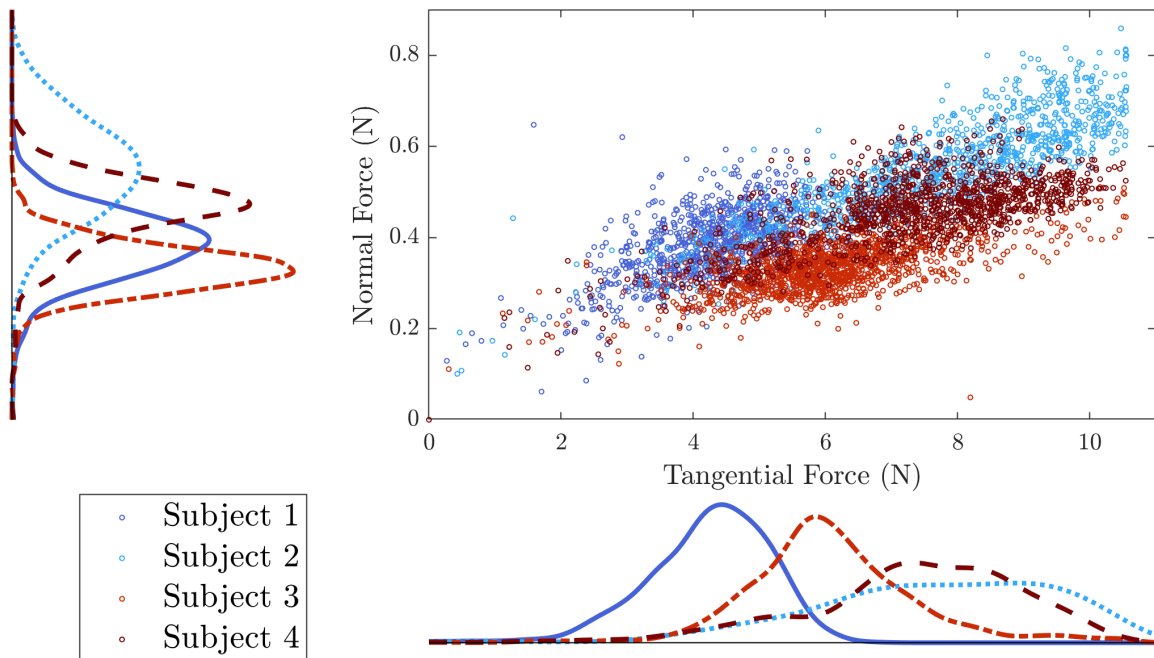
Figure 4.8: Plot of normal and tangential forces for all subjects.

4.4.4 Relationship Between Gaze, Tool Velocity, and Applied Forces

In this section, we examine the relationships between a subject's shifts in gaze and the corresponding changes in applied force and tool velocity. Our experimental setup cannot measure where in space a force was applied, only its components along the principle axes of the triaxial load cell. However, we can track how the tangential forces change, and correspondingly, how the eye movements and tool positions change in the same direction.

As a means of comparing the frequency characteristics of the gaze, tangential force, and the axial and tangential velocity properties of each subject, we have overlaid the frequency distributions of the fixations along with the power spectral densities of the forces and tool velocities onto a single plot. These plots are shown in Figure 4.9. We see that collective responses of each of the subjects exhibits a modal shape. These modes arise through the proprioceptive interaction of the human subjects with the natural dynamics of the mechanical system. We cannot say for certain which regime may predominate in this particular frequency band. However, the clamped test article is extremely stiff, and the grinding wheel was rotating at 5000 rpm. Mechanical resonances are most likely absent at such frequencies. Therefore it is likely that the force response in the 0 to 10Hz bandwidth is dominated by the characteristics of the gaze-motor system. The modes in these spectra are located at: Subject 1: 3Hz; Subject 2: 2.1Hz; Subject 3: 3.1Hz; Subject 4: 2.5Hz.

These modes encapsulate the behavioral characteristics of the subject as they perform the manual grinding task. It is clear that the peaks tool velocities similarly occur with peaks in tangential forces. These are the applied hand motions and the applied tool forces respectively. Likewise, Subjects 1, 3, and 4 all display a rolloff in their fixational response at frequencies corresponding to the force and velocity peaks. Hand motion and applied force occur together indicating purposeful movement, and similar changes in gaze behavior indicate a shift in attention corresponding to this movement. The coexistence of these modes show that, for this manual grinding task, visual attention is coupled to the motor system in a sensory feedback loop, and that we observe this to be so. The impact

of this observation will be discussed in Section 4.5.1.

Going further, if we refer back to Figures 4.4 through 4.9, the difference in the behavior of each of the subjects becomes more clear. Subject 1 and Subject 3 perform the task in a precise manner by moving the tool in complex paths, both axially and tangentially, with lower applied forces and velocities, and short fixations. By contrast, Subject 2 and Subject 4 move the tool primarily tangentially, with higher tangential forces and longer fixations. There is a clear contrast in the behaviors between these two groups of subjects.
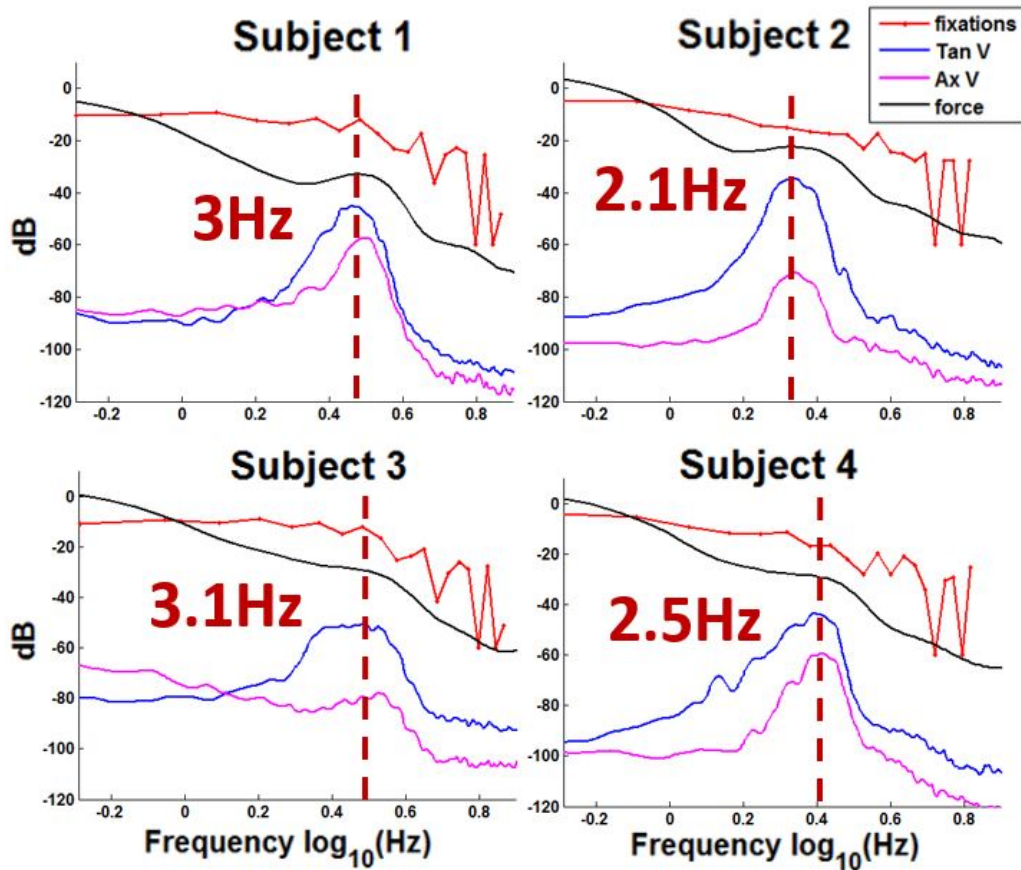
Figure 4.9: Comparison of modal responses in the gaze-motor behavior of all subjects

4.5 Tool Paths

The motion tracking system allowed to measure the position of the tool to track the tool path. Figure 4.10 shows the basic grinding techniques for all subjects for a single trace but with only 75% of the trial time period for better visualization purpose. This method

helped to capture the tacit knowledge of trajectories of a surface finishing tool operated by different skill leveled operators.
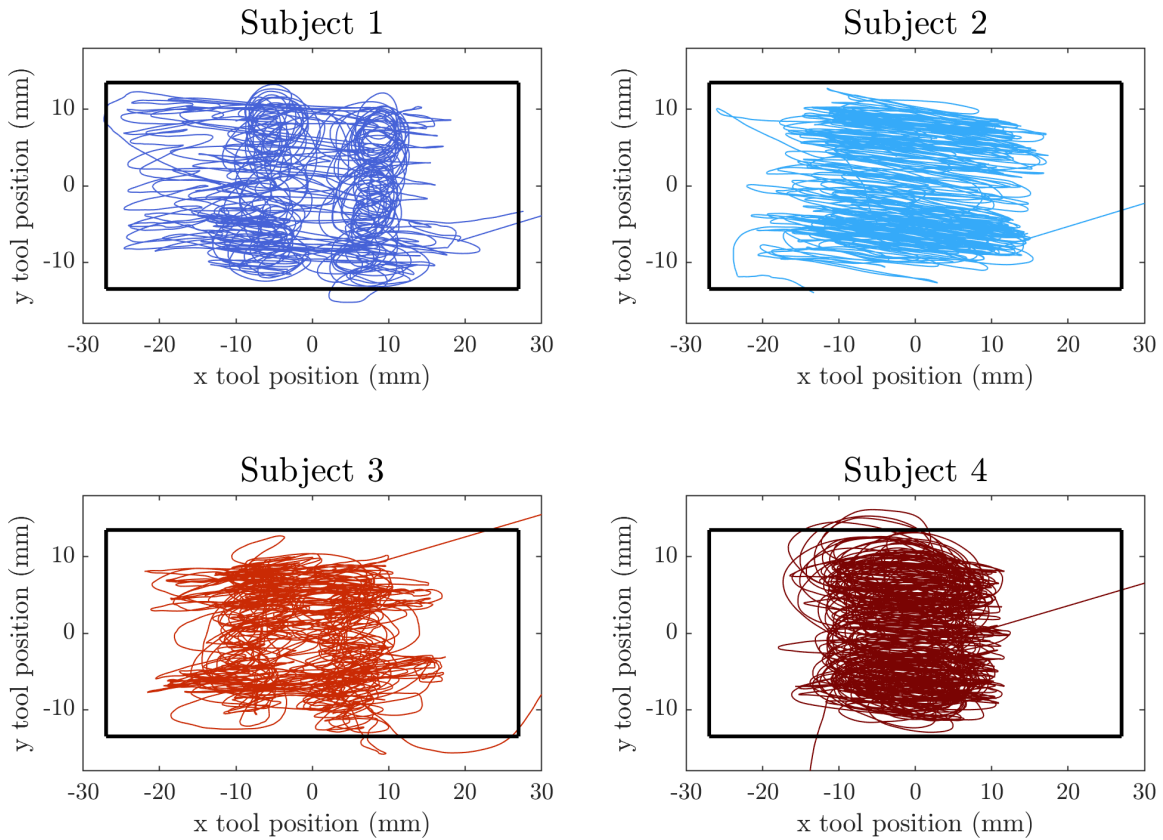
Figure 4.10: Detail of tool paths for all subjects

The x and y-axes represent the tool position over the samples surfaces. All four subjects have shown unique tool path behavior. Subject 1 and Subject 3 have moved the tool in the complex path, which was a combination of side-to-side and swirling motion. Subject 2 and Subject 4 have shown simple side-to-side motion. However, Subject 4 only covered a certain portion of workpieces while remaining parts are untouched.

We describe our method of analyzing the tool path data with the purpose of examining motion characteristics that arise from the techniques utilized by the individual subjects. The Optitrack motion capture system allows us to extract these behaviors directly from the tool path data. These behaviors can change abruptly or slowly as the task progresses, so we cannot assume that the time series is stationary over the course of a single grinding trial. Therefore, it is reasonable to assume that there are minimal changes in their motor

behaviors over relatively short timescales. Consequently, we have sectioned the time series data into sequential segments over which we do assume stationarity. Given the spectral responses, we have defined segment lengths of $\Delta t = 1$ second during which would expect to see roughly two to three sweeps of the tool.

Each subject has the ability to maneuver the tool in the axial and tangential directions independently. The separate degrees of freedom are only linked via purposeful movement, and any detectable coupling between the two would be an indication of a deliberate technique. In order to capture this relationship, we use a first order, multivariable autoregressive model, AR(1). The general expression for an AR(1) system is given by

$$x_i = Ax_{i-1} + b + \epsilon_i$$

where $x_i \in \mathbb{R}^N$ is a vector of measurements at the ith time step, $A \in \mathbb{R}^{N \times N}$ is the coefficient matrix for the AR(1) model, $b \in \mathbb{R}^N$ is the intercept vector or bias, and $\epsilon_i \in \mathbb{R}^N$ are independent identically distributed (iid) gaussian white noise terms $\mathcal{N}(0, \sigma^2)$. If we center each of the segments about its mean, the bias term is effectively zero. Thus, we can reduce our AR(1) model for our two degree of freedom system to

$$\begin{bmatrix} X_i^T \\ X_i^A \end{bmatrix} = \begin{bmatrix} a_{11} & a_{12} \\ a_{21} & a_{22} \end{bmatrix} \begin{bmatrix} X_{i-1}^T \\ X_{i-1}^A \end{bmatrix} + \begin{bmatrix} \epsilon_{i-1}^T \\ \epsilon_{i-1}^A \end{bmatrix}$$

where X_i^T is the tangential position and X_i^A is the axial position. Given the iid noise terms, we can approximate the A matrix using stepwise least-squares estimation. Next, we can solve this system for the current axial position X_i^A as a function of the past X_{i-1}^A and X_{i-1}^T as

$$X_i^A = \left(\frac{a_{21}}{a_{11}} \right) X_{i-1}^T + det(A) X_{i-1}^A.$$

If we let $\alpha = \left(\frac{a_{21}}{a_{11}} \right)$ and $\beta = det(A)$. we have an expression which captures the joint nature of the axial and tangential motion in the two parameters α and β for each time segment of $\Delta t = 1$ second. The parameter α is effectively the coupling constant between the axial and tangential tool positions. The tool path behavior of each subject can now be compared by plotting these points in the parameter space.

Figure 4.11a displays the α and β values for each of the four subjects. We can see that the data is concentrated tightly about $\beta = 1$. The AR model assumes that the system is causal and stable, comprised of an independent and a dependent variable. In this framework, we would expect that the current value of the axial position would depend little upon its past value and a β value of 1 would enforce that notion. In contrast, the α values indicate how much the current value of the axial position depends on the past value of the tangential position. In the case of our data, it describes how much counterclockwise swirling of the tool is present. Large negative values of α correspond to very tall (axial) oval shaped tool paths where small values correspond to wide (tangentially) ones.

Figure 4.11b plots the normalized histogram of only the α parameter for all four subjects. This is effectively a probability distribution over α, and a clear indication of how each of the subjects utilize the swirling technique. From the Figure 8 it is clear that Subject 2 performs the task primarily with sweeping, tangential motions, and very slow vertical motions across the sample. By contrast, Subjects 2 and 4 both utilize more circular motions, each with different eccentricities; Subject 4 exhibiting taller (axial) orbits than the Subject 4. Finally, while Subject 1 spends much of the time performing motions very similar to Subject 2, the tail of the distribution moves far to the left indicating the use of a very wide range of orbital eccentricities, both wide and tall. In fact, Subject 1 displayed an exceptionally wide range of tool motions, from primarily axial, to primarily tangential, and everything in between. This could not be said of the other three subjects whose techniques were very clearly dominated by a sweeping tangential motion.

4.5.1 Practical Implications and Impact

From performance analysis, Subject 1 and Subject 3 produced better surface quality compared to Subject 2 and Subject 4 and there was also a contrast on processing performance between these two sets of operators. These behavioral differences come from inherent techniques related to individual operator, which are expected to have a direct association with product output. We have referred to these sets of behavioral pattern as the exhibition of technique. For ease of syntax, since Subject 1 and Subject 3 showed a more complex tool path behavior, we have referred this set as Technique A,
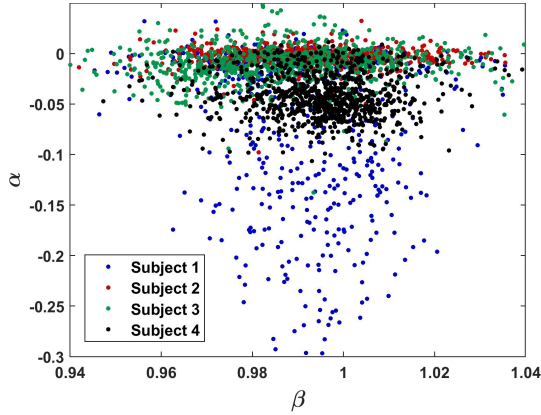
(a) Autoregressive parameters α and β for each subject over all 10 trials.
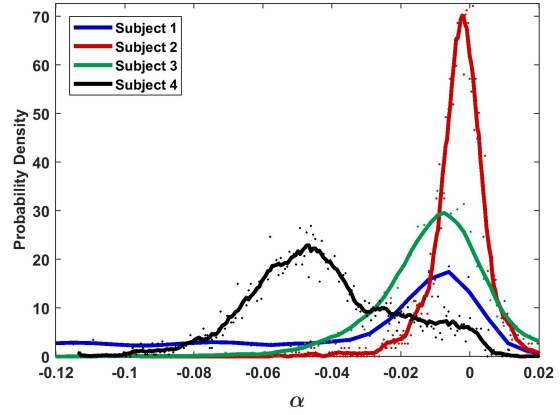
(b) Normalized histogram of α for each subject over all 10 trials.

and Subject 2 and Subject 4 set as Technique B. The behaviors associated with these techniques have been summarized in Table 4.1. Table 4.1 shows that Subject 1 and Subject 3 were able to remove more mass while utilizing lower normal and tangential forces, lower processing time, lower gaze frequency, and lower gaze shifts compared to Subject 2 and Subject 4. Furthermore, Subject 1 and Subject 3 have greater axial tool velocity, lower isotropy, which results in higher average surface roughness.

Table 4.1: Summary of Behaviors Exhibited Between the Two Techniques

Behavior	Technique A	Technique B
Tool Velocity	greater axial	less axial
Frequency of Gaze Shifts	more often	less often
Direction of Gaze Shifts	more axial	more tangential
Tangential Grinding Force	lower	higher

The quantitative information of these behavioral differences is shown in Table 4.2:

The findings from Table 4.2 can be summarized as follows:

- The tangential RMS tool velocity is lower for Technique A than for Technique B.

- The gaze frequency is higher for Technique A than for Technique B.

- The Axial RMS Gaze Shifts are higher for Technique A than for Technique B.

- The tangential Force is lower for Technique A than for Technique B.

- Machined surface isotropy is lower for Technique A than for Technique B.

- Processing time is lower for Technique A than for Technique B.

97

Table 4.2: Quantitative Analysis of Behavioral Difference of the Operators

Behavior	Technique A		Technique B	
Tool Velocity (m/sec)	Axial (RMS)	Tangential (RMS)	Axial (RMS)	Tangential (RMS)
	0.029	0.071	0.025	0.094
Gaze Shifts (pixels)	Axial (RMS)	Tangential (RMS)	Axial (RMS)	Tangential (RMS)
	41.808	31.318	33.141	34.637
Gaze Frequency (Hz)	mean=1.269 SD=1.309		mean=0.858 SD=0.930	
Tangential Force (N)	mean=5.174 SD=1.060		mean=7.076 SD=1.365	
Processing Time (sec)	mean=70.68 SD=7.75		mean=81.50 SD=20.68	

We also examined process parameters and discovered that Subject 1 and Subject 3 are able to remove more mass while utilizing lower tangential, and lower normal forces, indicating a more efficient grinding process. Furthermore, both Subject 1 and Subject 3 have low variation in applied forces and material removed implying a much more consistent process output. While Subject 1 shows larger average surface roughness than the other three subjects, the variation in this from trial to trial is extremely low, again indicating consistency. Of all the subjects, Subject 1 produced a product consistently and efficiently, followed closely by Subject 3. While Subject 2 was both less consistent and efficient, the subject does display characteristics of one who has experience with the grinding tool. By contrast, the performance of Subject 4 is highly random. This subject is able to perform the task, but shows little ability to produce in a repeatable fashion.

We can now summarize the relationships that we have discovered. Technique A was comprised of complex tool paths and low forces. This technique was exhibited by Subject 1 and Subject 3. These subjects also produced a more consistent product, more efficiently. Technique B, which included simple tangential tool paths and higher grinding forces was exhibited by Subject 2 and Subject 4. It resulted in a less consistent and less efficient output. Therefore, we have observed a relationship between manual grinding techniques which are displayed by practitioners of different levels of experience. The sensorimotor behaviors embedded in these techniques are observable and distinguishable. Finally, these techniques result in in different product outputs observed in the process parameters. Therefore, we can conclude that manual operation is not only an experience-based service but also depends on behavioral techniques of individuals. Because of similar behavioral

technique, Subject 1 and Subject 3 showed a similar pattern of complex tool path including processing characteristics. And due to experience impact, Subject 1 produced a product consistently and efficiently compared to Subject 3. On the contrary, Subject 4 was highly random, showed little ability to produce the part in a repeatable fashion due to limited expertise on the task.

In order to digitalize human performance, we would like to be able to join the behavioral and process parameter properties together in a formal model. The findings from this study show that this may be viable. Certainly an experiment with a larger cohort of subjects representing each experience level would be required in future work. A recognition of sensorimotor behaviors and their effects on the process outputs can be used to interrogate the manner in which each subject performs the task beyond their own internal perception. This in turn can be used to inform a personalized teaching regime. Furthermore, the design of a more thorough experiment could examine the eye and hand movements for a wider range of tasks (possibly two dimensional grinding) and how the forces and velocities change between "important" saccades. The possible rule for quantifying the importance of a saccade can be a function of the experience of the practitioner.

4.6 Conclusion

In this chapter, we have examined the visual-attention-motor behavioral characteristics involved in a manual grinding task. Four subjects of various experience levels were used in this pilot study. We were able to show that there were observable and distinguishable sensorimotor behaviors associated with two distinct techniques utilized by the individual subjects, and that task performance is affected by these techniques. Different cutting forces, and tool velocities are some of the very critical factors among a vast amount of other considerations, which have a direct impact on machined surface quality and material removal. Unlike automated processes, we see that in manual operations a user's skillset influences the process performance and consistency. Moreover, we can distinguish between the behavioral characteristics associated with observed techniques which can aid

in digitalization of manual performance and inform personalized training regimes. In our future work, we will continue to analyze product performance associated with processing parameters and the unique behaviors of the operators.

4.7 Acknowledgment

Chapter 5

Conclusion

5.1 Summary

In this dissertation, I have explored methods for interrogating human cognitive states while engaged in team tasks with two different forms of autonomy: a co-located robotic group of unicycle robots, and a remotely located robotic arm. I use methods from cognitive science, EEG measurements, and dynamic network theory to investigate correlations between EEG related neurological features, elicited human behavior, and self-reported trust in autonomy. This work establishes EEG network techniques as sound methods for estimating human cognitive state, and can be used to model more sophisticated interrelationships between humans and autonomous systems. In addition, I have compared human behaviors exhibited during a manual grinding task to differentiate behaviors among practitioners of different skill levels. The results of this work are critical if we wish to join behavioral and process parameter properties together in a formal model. Finding the right balance between process parameters and product performance is important for maximizing process efficiency.

The results of each experiment are summarized below.

5.1.1 EEG Network Examination of Human Robot Tasks

This chapter we examined external behaviors in concert with neurophysiological measures acquired via electroencephalography (EEG), to probe the interactions between cognitive processes, behaviors, and performance in a human-multiagent team task. We showed that changes in the α (8-12Hz) and θ (4-8Hz) bands of EEG indicate a higher

burden on the cognitive resources associated with visual-spatial reasoning required to estimate a more complex kinematic state of robotic agents. These results were reinforced by complementary behavioral shifts in gaze and pilot inputs. Additionally, higher performing subjects tended to engage more actively in the task by utilizing greater amounts of visual-spatial reasoning. Finally, we showed that features based on EEG dynamic-network-metrics distinguished gaze behaviors associated with the attention process more effectively than traditional single-channel metrics, indicating that single channels do not contain robust discriminative information, while the inter-channel relationships do.

5.1.2   EEG Network Examination of Human Trust in Autonomy

In this chapter, we ascertained a human's trust in an autonomous system via electroencephalogram (EEG) measurements. We showed that trust can be measured continuously and unobtrusively, and that using analysis techniques which account for interactions among brain regions shows benefits compared to more traditional methods which use only EEG signal power. Inter-channel connectivity network metrics, which measure dynamic changes in synchronous behavior between distant brain regions, appear to better capture cognitive activities that correlate with a human's trust in an autonomous system. Both single-channel powers and network-metrics that incorporate the frontal, parietal, and occipital lobes of the brain had the greatest impact on trust prediction.

5.1.3   Human Behaviors in a Manual Grinding Task

In this chapter we presented new techniques to analyze and understand the sensorimotor characteristics of manual operations such as grinding, and linked their influence on process performance. A grinding task, though simple, requires the practitioner to combine elements from the large repertoire of his or her skillset. Based on the joint gaze, force, and velocity data collected from a series of manual grinding experiments, we compared operators with different levels of experience and quantitatively described characteristics of human manual skill and their effects on manufacturing process

parameters such as material removal rate. For instance, we found that an experienced subject performed the task in a precise manner by moving the tool in complex paths, with lower applied forces and velocities, and short fixations compared to a novice. A detailed understanding of gaze-motor behavior broadens our knowledge of how a manual task is executed. Our results help to provide this extra insight, and impact future efforts in workforce training as well as the digitalization of manual expertise, thereby facilitating the transformation of raw data into product-specific knowledge.

5.2   Future Work

There are several key efforts that would yield valuable insights into some of the research questions posed in this dissertation. In Chapter 3, we used static linear models to predict human trust in autonomy. Moving forward, we could use regression models of a higher order, or state space models to capture the proper dynamics of the human-autonomy interaction. Second, network metrics could be incorporated into multi-modal models which include more traditional, unobtrusive psychophisiological measures such as skin conductance, electrocardiogram, and respiration. Another potential avenue would be to explore different types of brain activity measures such as those listed in Table A.2. For example, fMRI can capture neural activity at different timescales than EEG. We can also use the sub-regions from Chapter 3 as a starting point for a more sophisticated spatial and temporal investigation using machine learning methods. Such as study could yield EEG channel subsets that are both highly informative and robust, resulting in a more effective cognitive state estimation model.

Another important step would be to connect the work from Chapter 4 with the methods from Chapter 3 to investigate the neurological activity patterns exhibited by practitioners of different skill levels. Gaze data has already been used for training in manual tasks, and the use of EEG may be beneficial in focusing training effort so as to reduce necessary practice among novice learners.

5.3 Final Thoughts

The use of EEG has been shown be crucial in understanding underlying cognitive processes. Nevertheless, the implementation of existing high fidelity systems in an operational setting poses significant challenges. The devices themselves can be rather uncomfortable to wear for long periods of time, and the electrode impedance can change substantially as the conductive media, such as saline or gel, begin to dry out. Newer types of dry electrodes may be used, but these are more expensive alternatives.

Network metrics show great promise, however, it is critical to evaluate the specific properties they capture in relation to the experimental hypotheses under investigation. A failure to do so may obfuscate a proper interpretation of the results. It is far too easy use pre-existing code to generate an array of values that have no basis in the scientific question under scrutiny. For example, if synchrony between distant brain regions is the object of an investigation, then clusters of local functional interaction should be eliminated from the analysis. The use of multi-layered network comprised of integrated brain regions over different spatial distances may yield better results. Additionally, long distance synchrony between brain regions can be isolated by exploring the formation and dissolution of sympletic structures defined by the network edges. In those kinds of analyses, distance metrics such as network efficiency may be less informative due to the fact that network structures of interest are groups of mutually connected nodes.

The motivation for the work presented in this dissertation is the development of systems that can automatically support the operator in executing working tasks during human-autonomy teaming. An important step in achieving that goal is to develop accurate real-time estimates of the changes in human cognitive state. It is common in the literature to reconcile neurological or psychophisiological measures with established surveys as these have been considered the gold standard for many years. However, human-autonomy teams will be evaluated by team task effectiveness, and the human's role in the team may not necessarily be optimized by adapting the autonomy to maximize trust, or minimize cognitive load. On the contrary, it is during periods of heightened stress that humans can excel at synthesizing elements from their past

experiences into novel solutions to goal directed problems. Consequently, a model that conforms to survey measures may not generalize well when a closing the loop around a human-autonomous-system team. Future experiments must be carefully designed to explore neurological correlates that arise due to the change in human-autonomy-team task effectiveness.

References

[1] S. Bashyal and G. K. Venayagamoorthy, "Human swarm interaction for radiation source search and localization," in *2008 IEEE Swarm Intelligence Symposium*. IEEE, Nov. 2008, pp. 1–8.

[2] K. Nagatani, S. Kiribayashi, Y. Okada, K. Otake, K. Yoshida, S. Tadokoro, T. Nishimura, T. Yoshida, E. Koyanagi, M. Fukushima, and S. Kawatsuma, "Emergency response to the nuclear accident at the Fukushima Daiichi Nuclear Power Plants using mobile rescue robots: Emergency Response to the Fukushima Nuclear Accident using Rescue Robots," *Journal of Field Robotics*, vol. 30, no. 1, pp. 44–63, Jan. 2013.

[3] T. Fong, J. Rochlis Zumbado, N. Currie, A. Mishkin, and D. L. Akin, "Space Telerobotics: Unique Challenges to Human–Robot Collaboration in Space," *Reviews of Human Factors and Ergonomics*, vol. 9, no. 1, pp. 6–56, Nov. 2013.

[4] F. Gervits, D. Thurston, R. Thielstrom, T. Fong, Q. Pham, and M. Scheutz, "Toward genuine robot teammates: Improving human-robot team performance using robot shared mental models," p. 429–437, 2020.

[5] K. E. Schaefer, E. R. Straub, J. Y. Chen, J. Putney, and A. Evans, "Communicating intent to develop shared situation awareness and engender trust in human-agent teams," *Cognitive Systems Research*, vol. 46, pp. 26–39, Dec. 2017.

[6] S. Musić and S. Hirche, "Control sharing in human-robot team interaction," *Annual Reviews in Control*, vol. 44, pp. 342–354, 2017. [Online]. Available: http://linkinghub.elsevier.com/retrieve/pii/S1367578817301153

[7] A. R. Marathe, J. S. Metcalfe, B. J. Lance, J. R. Lukos, D. Jangraw, K.-T. Lai, J. Touryan, E. Stump, B. M. Sadler, W. Nothwang, and K. McDowell, "The privileged sensing framework: A principled approach to improved human-autonomy integration," *Theoretical Issues in Ergonomics Science*, vol. 19, no. 3, pp. 283–320, May 2018.

[8] M. L. Cummings and A. S. Brzezinski, "Global vs. local decision support for multiple independent uav schedule management," *International Journal of Applied Decision Sciences*, vol. 3, no. 3, pp. 188–205, Oct. 2010.

[9] G. L. Calhoun, H. A. Ruff, K. J. Behymer, and E. M. Frost, "Human-autonomy teaming interface design considerations for multi-unmanned vehicle control," *Theoretical Issues in Ergonomics Science*, vol. 19, no. 3, pp. 321–352, May 2018. [Online]. Available: https://www.tandfonline.com/doi/full/10.1080/1463922X.2017.1315751

[10] C. P. C. Chanel, R. N. Roy, F. Dehais, and N. Drougard, "Towards mixed-initiative human–robot interaction: assessment of discriminative physiological and behavioral

features for performance prediction," *Sensors*, vol. 20, no. 1, p. 296, Jan. 2020. [Online]. Available: https://www.mdpi.com/1424-8220/20/1/296

[11] H. Zhang, R. Chavarriaga, Z. Khaliliardali, L. Gheorghe, I. Iturrate, and J. d. R. Millán, "EEG-based decoding of error-related brain activity in a real-world driving task," *Journal of Neural Engineering*, vol. 12, no. 6, Dec. 2015. [Online]. Available: https://iopscience.iop.org/article/10.1088/1741-2560/12/6/066028

[12] P. Arico, G. Borghini, G. Di Flumeri, N. Sciaraffa, A. Colosimo, and F. Babiloni, "Passive BCI in Operational Environments: Insights, Recent Advances, and Future Trends," *IEEE Transactions on Biomedical Engineering*, vol. 64, no. 7, pp. 1431–1436, Jul. 2017.

[13] J. E. Thropp, T. Oron-Gilad, J. L. Szalma, and P. A. Hancock, "Calibrating Adaptable Automation to Individuals," *IEEE Transactions on Human-Machine Systems*, vol. 48, no. 6, pp. 691–701, Dec. 2018.

[14] T. Fong, C. Thorpe, and C. Baur, "Multi-robot remote driving with collaborative control," *IEEE Transactions on Industrial Electronics*, vol. 50, no. 4, pp. 699–704, Aug. 2003. [Online]. Available: http://ieeexplore.ieee.org/document/1215473/

[15] J. Li, A. Bezerianos, and N. Thakor, "Cognitive State Analysis, Understanding, and Decoding from the Perspective of Brain Connectivity," in *Handbook of Neuroengineering*, N. V. Thakor, Ed. Singapore: Springer Singapore, 2021, pp. 1–35.

[16] P. L. Nunez and R. Srinivasan, *Electric fields of the brain: the neurophysics of EEG*, 2nd ed. Oxford ; New York: Oxford University Press, 2006.

[17] W. Klimesch, "Eeg alpha and theta oscillations reflect cognitive and memory performance: a review and analysis," *Brain research reviews*, vol. 29, no. 2, pp. 169–195, Apr. 1999.

[18] P. Zarjam, J. Epps, and N. H. Lovell, "Beyond subjective self-rating: Eeg signal classification of cognitive workload," *IEEE Transactions on Autonomous Mental Development*, vol. 7, no. 4, pp. 301–310, 2015.

[19] B. A. Urgen, M. Plank, H. Ishiguro, H. Poizner, and A. P. Saygin, "EEG theta and mu oscillations during perception of human and robot actions," *Frontiers in Neurorobotics*, vol. 7, 2013. [Online]. Available: http://journal.frontiersin.org/article/10.3389/fnbot.2013.00019/abstract

[20] L. F. Nicolas-Alonso and J. Gomez-Gil, "Brain computer interfaces, a review," *Sensors*, vol. 12, no. 2, pp. 1211–1279, Jan. 2012. [Online]. Available: http://www.mdpi.com/1424-8220/12/2/1211

[21] J. F. Cavanagh and M. J. Frank, "Frontal theta as a mechanism for cognitive control," *Trends in Cognitive Sciences*, vol. 18, no. 8, pp. 414–421, Aug. 2014. [Online]. Available: http://linkinghub.elsevier.com/retrieve/pii/S1364661314001077

[22] M. S. Clayton, N. Yeung, and R. Cohen Kadosh, "The roles of cortical oscillations in sustained attention," *Trends in Cognitive Sciences*, vol. 19, no. 4, pp. 188–195, Apr. 2015. [Online]. Available: https://linkinghub.elsevier.com/retrieve/pii/S1364661315000285

[23] S. Palva and J. M. Palva, "Functional Roles of Alpha-Band Phase Synchronization in Local and Large-Scale Cortical Networks," *Frontiers in Psychology*, vol. 2, 2011.

[24] G. Borghini, L. Astolfi, G. Vecchiato, D. Mattia, and F. Babiloni, "Measuring neurophysiological signals in aircraft pilots and car drivers for the assessment of mental workload, fatigue and drowsiness," *Neuroscience & Biobehavioral Reviews*, vol. 44, pp. 58–75, Jul. 2014.

[25] K. Mandrick, V. Peysakhovich, F. Rémy, E. Lepron, and M. Causse, "Neural and psychophysiological correlates of human performance under stress and high mental workload," *Biological Psychology*, vol. 121, pp. 62–73, Dec. 2016.

[26] O. Sporns and R. F. Betzel, "Modular brain networks," *Annual Review of Psychology*, vol. 67, no. 1, pp. 613–640, Jan. 2016. [Online]. Available: http://www.annualreviews.org/doi/10.1146/annurev-psych-122414-033634

[27] L. Byrge, O. Sporns, and L. B. Smith, "Developmental process emerges from extended brain–body–behavior networks," *Trends in Cognitive Sciences*, vol. 18, no. 8, pp. 395–403, Aug. 2014.

[28] M. W. Cole, J. R. Reynolds, J. D. Power, G. Repovs, A. Anticevic, and T. S. Braver, "Multi-task connectivity reveals flexible hubs for adaptive task control," *Nature Neuroscience*, vol. 16, no. 9, pp. 1348–1355, Sep. 2013.

[29] A. Nikolaidis and A. K. Barbey, "Network Dynamics Theory of Human Intelligence," in *The Cambridge Handbook of the Neuroscience of Creativity*, 1st ed., R. E. Jung and O. Vartanian, Eds. Cambridge University Press, Jan. 2018, pp. 382–404.

[30] S. M. Doesburg, N. Bedo, and L. M. Ward, "Top-down alpha oscillatory network interactions during visuospatial attention orienting," *NeuroImage*, vol. 132, pp. 512–519, May 2016. [Online]. Available: http://linkinghub.elsevier.com/retrieve/pii/S1053811916001944

[31] D. S. Bassett and O. Sporns, "Network neuroscience," *Nature Neuroscience*, vol. 20, no. 3, pp. 353–364, Mar. 2017. [Online]. Available: http://www.nature.com/articles/nn.4502

[32] R. M. Hutchison, T. Womelsdorf, E. A. Allen, P. A. Bandettini, V. D. Calhoun, M. Corbetta, S. Della Penna, J. H. Duyn, G. H. Glover, J. Gonzalez-Castillo, D. A. Handwerker, S. Keilholz, V. Kiviniemi, D. A. Leopold, F. de Pasquale, O. Sporns, M. Walter, and C. Chang, "Dynamic functional connectivity: promise, issues, and interpretations," *NeuroImage*, vol. 80, pp. 360–378, Oct. 2013. [Online]. Available: https://linkinghub.elsevier.com/retrieve/pii/S105381191300579X

[33] J. B. Lyons, K. Sycara, M. Lewis, and A. Capiola, "Human–Autonomy Teaming: Definitions, Debates, and Directions," *Frontiers in Psychology*, vol. 12, p. 589585, May 2021.

[34] G. Bales and Z. Kong, "Neurophysiological and Behavioral Differences in Human-Multiagent Tasks: An EEG Network Perspective," *ACM Transactions on Human-Robot Interaction*, vol. 11, no. 4, pp. 1–25, Dec. 2022.

[35] ——, "Neurophysiological and behavioral studies of human-swarm interaction tasks," in *2017 IEEE International Conference on Systems, Man, and Cybernetics (SMC)*, Oct. 2017, pp. 671–676.

[36] ——, "Cognitive correlates of eeg spectral power indicate human-swarm task performance," in *Proceedings of the 8th International Conference on the Internet of Things*, ser. IOT '18. New York, NY, USA: Association for Computing Machinery, 2018. [Online]. Available: https://doi.org/10.1145/3277593.3277613

[37] G. Bales, A. P. Anderson, J. Dekarske, S. Joshi, and Z. Kong, "An Investigation of EEG-Network-based Dynamic Trust Metrics in Human-autonomy Teaming," May 2023.

[38] G. L. Bales, J. Das, J. Tsugawa, B. Linke, and Z. Kong, "Digitalization of Human Operations in the Age of Cyber Manufacturing: Sensorimotor Analysis of Manual Grinding Performance," *Journal of Manufacturing Science and Engineering*, vol. 139, no. 10, Sep. 2017.

[39] G. Bales, J. Das, B. Linke, and Z. Kong, "Recognizing Gaze-Motor Behavioral Patterns in Manual Grinding Tasks — Elsevier Enhanced Reader," *Procedia Manufacturing*, vol. 5, pp. 106–121, 2016.

[40] J. Das, G. L. Bales, Z. Kong, and B. Linke, "Integrating Operator Information for Manual Grinding and Characterization of Process Performance Based on Operator Profile," *Journal of Manufacturing Science and Engineering*, vol. 140, no. 8, p. 081011, Jun. 2018.

[41] M. Cummings, L. Huang, H. Zhu, D. Finkelstein, and R. Wei, "The impact of increasing autonomy on training requirements in a UAV supervisory control task," *Journal of Cognitive Engineering and Decision Making*, vol. 13, no. 4, pp. 295–309, Dec. 2019. [Online]. Available: http://journals.sagepub.com/doi/10.1177/1555343419868917

[42] G. Podevijn, R. O'Grady, C. Fantini-Hauwel, and M. Dorigo, "Human responses to stimuli produced by robot swarms - the effect of the reality-gap on psychological state," in *Distributed Autonomous Robotic Systems*, R. Gross, A. Kolling, S. Berman, E. Frazzoli, A. Martinoli, F. Matsuno, and M. Gauci, Eds. Cham: Springer International Publishing, 2018, vol. 6, pp. 531–543.

[43] A. Steinfeld, T. Fong, D. Kaber, M. Lewis, J. Scholtz, A. Schultz, and M. Goodrich, "Common metrics for human-robot interaction," in *Proceeding of the 1st ACM SIGCHI/SIGART conference on Human-robot interaction (HRI '06)*. Salt Lake City, Utah, USA: Association for Computing Machinery, Mar. 2006, pp. 33–40. [Online]. Available: http://portal.acm.org/citation.cfm?doid=1121241.1121249

[44] M. I. Posner, *Cognitive neuroscience of attention*. New York, NY, USA: Guilford Press, 2011.

[45] A. Baddeley, "Working memory: theories, models, and controversies," *Annual Review of Psychology*, vol. 63, no. 1, pp. 1–29, Jan. 2012. [Online]. Available: http://www.annualreviews.org/doi/10.1146/annurev-psych-120710-100422

[46] M. J. Kane, A. R. A. Conway, D. Z. Hambrick, and R. W. Engle, "Variation in working memory capacity as variation in executive attention and control," in *Variation in Working Memory*, A. Conway, C. Jarrold, M. Kane, A. Miyake, and J. Towse, Eds. Oxford University Press, Mar. 2008, pp. 21–48. [Online]. Available: https://oxford.universitypressscholarship.com/view/10.1093/acprof:oso/9780195168648.001.0001/acprof-9780195168648-chapter-2

[47] A. Duchowski, *Eye tracking methodology: theory and practice*, 2nd ed. London: Springer, 2007.

[48] S. Christopher, F. De Blasio, S. Mcdonald, and J. Rushby, "Validating the use of emotiv epoc in resting eeg coherence research," vol. 9, Jan. 2015.

[49] M. Egerstedt and X. Hu, "Formation constrained multi-agent control," *IEEE Transactions on Robotics and Automation*, vol. 17, no. 6, pp. 947–951, Dec. 2001.

[50] N. Cowan, "The focus of attention as observed in visual working memory tasks: making sense of competing claims," *Neuropsychologia*, vol. 49, no. 6, pp. 1401–1406, May 2011. [Online]. Available: https://linkinghub.elsevier.com/retrieve/pii/S0028393211000522

[51] M. K. Islam, A. Rastegarnia, and Z. Yang, "Methods for artifact detection and removal from scalp EEG: a review," *Neurophysiologie Clinique/Clinical Neurophysiology*, vol. 46, no. 4-5, pp. 287–305, Nov. 2016. [Online]. Available: http://linkinghub.elsevier.com/retrieve/pii/S098770531630199X

[52] A. Hyvarinen, "Fast and robust fixed-point algorithms for independent component analysis," *IEEE transactions on Neural Networks*, vol. 10, no. 3, pp. 626–634, 1999.

[53] H. E. Wang, C. G. Benar, P. P. Quilichini, K. J. Friston, V. K. Jirsa, and C. Bernard, "A systematic framework for functional connectivity measures," *Frontiers in Neuroscience*, vol. 8, Dec. 2014. [Online]. Available: http://journal.frontiersin.org/article/10.3389/fnins.2014.00405/abstract

[54] J.-P. Lachaux, E. Rodriguez, J. Martinerie, and F. J. Varela, "Measuring phase synchrony in brain signals," *Human brain mapping*, vol. 8, no. 4, pp. 194–208, Nov. 1999.

[55] A. M. Bastos and J.-M. Schoffelen, "A tutorial review of functional connectivity analysis methods and their interpretational pitfalls," *Frontiers in Systems Neuroscience*, vol. 9, Jan. 2016. [Online]. Available: http://journal.frontiersin.org/Article/10.3389/fnsys.2015.00175/abstract

[56] M. Rubinov and O. Sporns, "Complex network measures of brain connectivity: Uses and interpretations," *NeuroImage*, vol. 52, no. 3, pp. 1059–1069, Sep. 2010. [Online]. Available: https://linkinghub.elsevier.com/retrieve/pii/S105381190901074X

[57] W. Klimesch, "Alpha-band oscillations, attention, and controlled access to stored information," *Trends in Cognitive Sciences*, vol. 16, no. 12, pp. 606–617, Dec. 2012. [Online]. Available: http://linkinghub.elsevier.com/retrieve/pii/S1364661312002434

[58] R. Gulbinaite, A. Johnson, R. de Jong, C. C. Morey, and H. van Rijn, "Dissociable mechanisms underlying individual differences in visual working memory capacity," *NeuroImage*, vol. 99, pp. 197–206, Oct. 2014. [Online]. Available: https://linkinghub.elsevier.com/retrieve/pii/S105381191400425X

[59] K. Akash, W.-L. Hu, N. Jain, and T. Reid, "A Classification Model for Sensing Human Trust in Machines Using EEG and GSR," *ACM Transactions on Interactive Intelligent Systems*, vol. 8, no. 4, pp. 1–20, Nov. 2018. [Online]. Available: https://dl.acm.org/doi/10.1145/3132743

[60] U. Braun, A. Schäfer, H. Walter, S. Erk, N. Romanczuk-Seiferth, L. Haddad, J. I. Schweiger, O. Grimm, A. Heinz, H. Tost, A. Meyer-Lindenberg, and D. S. Bassett, "Dynamic reconfiguration of frontal brain networks during executive cognition in humans," *Proceedings of the National Academy of Sciences*, vol. 112, no. 37, pp. 11 678–11 683, Sep. 2015. [Online]. Available: http://www.pnas.org/lookup/doi/10.1073/pnas.1422487112

[61] M. W. Cole, J. R. Reynolds, J. D. Power, G. Repovs, A. Anticevic, and T. S. Braver, "Multi-task connectivity reveals flexible hubs for adaptive task control," *Nature Neuroscience*, vol. 16, no. 9, pp. 1348–1355, Sep. 2013. [Online]. Available: http://www.nature.com/articles/nn.3470

[62] K. T. Wynne and J. B. Lyons, "An integrative model of autonomous agent teammate-likeness," *Theoretical Issues in Ergonomics Science*, vol. 19, no. 3, pp. 353–374, May 2018.

[63] V. Groom and C. Nass, "Can robots be teammates?: Benchmarks in human–robot teams," *Interaction Studies. Social Behaviour and Communication in Biological and Artificial Systems*, vol. 8, no. 3, pp. 483–500, Nov. 2007.

[64] J. Y. C. Chen and M. J. Barnes, "Human–Agent Teaming for Multirobot Control: A Review of Human Factors Issues," *IEEE Transactions on Human-Machine Systems*, vol. 44, no. 1, pp. 13–29, Feb. 2014.

[65] E. J. de Visser, M. M. M. Peeters, M. F. Jung, S. Kohn, T. H. Shaw, R. Pak, and M. A. Neerincx, "Towards a Theory of Longitudinal Trust Calibration in Human–Robot Teams," *International Journal of Social Robotics*, vol. 12, no. 2, pp. 459–478, May 2020.

[66] Y. S. Razin and K. M. Feigh, "Converging Measures and an Emergent Model: A Meta-Analysis of Human-Automation Trust Questionnaires," Mar. 2023.

[67] R. C. Mayer, J. H. Davis, and F. D. Schoorman, "An integrative model of organizational trust," *The Academy of Management Review*, vol. 20, no. 3, pp. 709–734, 1995. [Online]. Available: http://www.jstor.org/stable/258792

[68] J. D. Lee and K. A. See, "Trust in Automation: Designing for Appropriate Reliance," *Human Factors*, p. 31, 2004.

[69] P. A. Hancock, D. R. Billings, K. E. Schaefer, J. Y. C. Chen, E. J. de Visser, and R. Parasuraman, "A Meta-Analysis of Factors Affecting Trust in Human-Robot Interaction," *Human Factors: The Journal of the Human Factors and Ergonomics Society*, vol. 53, no. 5, pp. 517–527, Oct. 2011.

[70] B. M. Muir and N. Moray, "Trust in automation. Part II. Experimental studies of trust and human intervention in a process control simulation," *Ergonomics*, vol. 39, no. 3, pp. 429–460, Mar. 1996.

[71] S. C. Kohn, E. J. De Visser, E. Wiese, Y.-C. Lee, and T. H. Shaw, "Measurement of Trust in Automation: A Narrative Review and Reference Guide," *Frontiers in Psychology*, vol. 12, p. 604977, Oct. 2021.

[72] J.-Y. Jian, A. M. Bisantz, and C. G. Drury, "Foundations for an Empirically Determined Scale of Trust in Automated Systems," *International Journal of Cognitive Ergonomics*, vol. 4, no. 1, pp. 53–71, Mar. 2000.

[73] R. E. Yagoda and D. J. Gillan, "You Want Me to Trust a ROBOT? The Development of a Human–Robot Interaction Trust Scale," *International Journal of Social Robotics*, vol. 4, no. 3, pp. 235–248, Aug. 2012.

[74] N. Tenhundfeld, M. Demir, and E. De Visser, "Assessment of Trust in Automation in the "Real World": Requirements for New Trust in Automation Measurement Techniques for Use by Practitioners," *Journal of Cognitive Engineering and Decision Making*, vol. 16, no. 2, pp. 101–118, Jun. 2022.

[75] K. Akash, W.-L. Hu, N. Jain, and T. Reid, "A Classification Model for Sensing Human Trust in Machines Using EEG and GSR," *ACM Transactions on Interactive Intelligent Systems*, vol. 8, no. 4, pp. 1–20, Nov. 2018.

[76] W. Klimesch, "Alpha-band oscillations, attention, and controlled access to stored information," *Trends in Cognitive Sciences*, vol. 16, no. 12, pp. 606–617, Dec. 2012.

[77] G. G. Gregoriou, S. Paneri, and P. Sapountzis, "Oscillatory synchrony as a mechanism of attentional processing," *Brain Research*, vol. 1626, pp. 165–182, Nov. 2015.

[78] D. S. Bassett, A. N. Khambhati, and S. T. Grafton, "Emerging Frontiers of Neuroengineering: A Network Science of Brain Connectivity," *Annual Review of Biomedical Engineering*, vol. 19, no. 1, pp. 327–352, Jun. 2017.

[79] R. M. Hutchison, T. Womelsdorf, E. A. Allen, P. A. Bandettini, V. D. Calhoun, M. Corbetta, S. Della Penna, J. H. Duyn, G. H. Glover, J. Gonzalez-Castillo, D. A. Handwerker, S. Keilholz, V. Kiviniemi, D. A. Leopold, F. de Pasquale, O. Sporns, M. Walter, and C. Chang, "Dynamic functional connectivity: Promise, issues, and interpretations," *NeuroImage*, vol. 80, pp. 360–378, Oct. 2013.

[80] J. Faskowitz, R. F. Betzel, and O. Sporns, "Edges in brain networks: Contributions to models of structure and function," *Network Neuroscience*, pp. 1–28, Oct. 2021.

[81] A. Xu and G. Dudek, "Towards Modeling Real-Time Trust in Asymmetric Human–Robot Collaborations," in *Robotics Research*, M. Inaba and P. Corke, Eds. Cham: Springer International Publishing, 2016, vol. 114, pp. 113–129.

[82] M. X. Cohen, "A better way to define and describe Morlet wavelets for time-frequency analysis," *NeuroImage*, vol. 199, pp. 81–86, Oct. 2019.

[83] S. Sanei and J. Chambers, *EEG Signal Processing*. West Sussex, England: John Wiley & Sons, Ltd, 2007.

[84] V. Sakkalis, "Review of advanced techniques for the estimation of brain connectivity measured with EEG/MEG," *Computers in Biology and Medicine*, vol. 41, no. 12, pp. 1110–1117, Dec. 2011.

[85] K. Yoshinaga, M. Matsuhashi, T. Mima, H. Fukuyama, R. Takahashi, T. Hanakawa, and A. Ikeda, "Comparison of Phase Synchronization Measures for Identifying Stimulus-Induced Functional Connectivity in Human Magnetoencephalographic and Simulated Data," *Frontiers in Neuroscience*, vol. 14, p. 648, Jun. 2020.

[86] M. Rubinov and O. Sporns, "Complex network measures of brain connectivity: Uses and interpretations," *NeuroImage*, vol. 52, no. 3, pp. 1059–1069, Sep. 2010.

[87] M. E. J. Newman, "Assortative mixing in networks," *Phys. Rev. Lett.*, vol. 89, p. 208701, Oct 2002. [Online]. Available: https://link.aps.org/doi/10.1103/PhysRevLett.89.208701

[88] K. A. Hoff and M. Bashir, "Trust in Automation: Integrating Empirical Evidence on Factors That Influence Trust," *Human Factors: The Journal of the Human Factors and Ergonomics Society*, vol. 57, no. 3, pp. 407–434, May 2015.

[89] *MATLAB version 9.12.0.1956245 (R2022a) Update 2*, The Mathworks, Inc., Natick, Massachusetts, 2022.

[90] M. Kuhn and K. Johnson, *Applied Predictive Modeling.* New York, NY: Springer New York, 2013.

[91] F. Vása and B. Misić, "Null models in network neuroscience," *Nature Reviews Neuroscience*, vol. 23, no. 8, pp. 493–504, Aug. 2022.

[92] E. Bullmore and O. Sporns, "Complex brain networks: Graph theoretical analysis of structural and functional systems," *Nature Reviews Neuroscience*, vol. 10, no. 3, pp. 186–198, Mar. 2009.

[93] W. van den Bos, E. van Dijk, M. Westenberg, S. A. Rombouts, and E. A. Crone, "What motivates repayment? Neural correlates of reciprocity in the Trust Game," *Social Cognitive and Affective Neuroscience*, vol. 4, no. 3, pp. 294–304, 03 2009. [Online]. Available: https://doi.org/10.1093/scan/nsp009

[94] E. Goldstein, *Cognitive psychology: Connecting mind, research and everyday experience.* Cengage Learning, 2014.

[95] T. Wojtara, M. Uchihara, H. Murayama, S. Shimoda, S. Sakai, H. Fujimoto, and H. Kimura, "Human–robot collaboration in precise positioning of a three-dimensional object," *Automatica*, vol. 45, no. 2, pp. 333–342, 2009.

[96] J. Lee, B. Bagheri, and H.-A. Kao, "A Cyber-Physical Systems architecture for Industry 4.0-based manufacturing systems," *Manufacturing Letters*, vol. 3, pp. 18–23, Jan. 2015. [Online]. Available: http://linkinghub.elsevier.com/retrieve/pii/S221384631400025X

[97] E. Francalanza, J. Borg, and C. Constantinescu, "Development and evaluation of a knowledge-based decision-making approach for designing changeable manufacturing systems," *CIRP Journal of Manufacturing Science and Technology*, vol. 16, pp. 81–101, Jan. 2017. [Online]. Available: http://linkinghub.elsevier.com/retrieve/pii/S1755581716300335

[98] L. Wang, M. Törngren, and M. Onori, "Current status and advancement of cyber-physical systems in manufacturing," *Journal of Manufacturing Systems*, vol. 37, pp. 517–527, Oct. 2015. [Online]. Available: http://linkinghub.elsevier.com/retrieve/pii/S0278612515000400

[99] J. Das and B. Linke, "Effect of Manual Grinding Operations on Surface Integrity," *Procedia CIRP*, vol. 45, pp. 95–98, 2016. [Online]. Available: http://linkinghub.elsevier.com/retrieve/pii/S2212827116003735

[100] S. Mezghani and M. El Mansori, "Abrasiveness properties assessment of coated abrasives for precision belt grinding," *Surface and Coatings Technology*, vol. 203, no. 5-7, pp. 786–789, Dec. 2008. [Online]. Available: http://linkinghub.elsevier.com/retrieve/pii/S0257897208008062

[101] A. Khellouki, J. Rech, and H. Zahouani, "The effect of abrasive grain's wear and contact conditions on surface texture in belt finishing," *Wear*, vol. 263, no. 1-6, pp. 81–87, Sep. 2007. [Online]. Available: http://linkinghub.elsevier.com/retrieve/pii/S0043164807003961

[102] K. Odum, M. C. Castillo, J. Das, and B. Linke, "Sustainability analysis of grinding with power tools," *Procedia CIRP*, vol. 14, pp. 570–574, 2014.

[103] J. Das and B. Linke, "Evaluation and systematic selection of significant multi-scale surface roughness parameters (SRPs) as process monitoring index," *Journal of Materials Processing Technology*, Jan. 2017. [Online]. Available: http://linkinghub.elsevier.com/retrieve/pii/S0924013617300171

[104] M. F. Land, "Vision, eye movements, and natural behavior," *Visual neuroscience*, vol. 26, no. 01, pp. 51–62, 2009.

[105] T. Erez, J. J. Tramper, W. D. Smart, and S. C. Gielen, "A pomdp model of eye-hand coordination." in *AAAI*, 2011.

[106] W. Yi and D. Ballard, "Recognizing behavior in hand-eye coordination patterns," *International Journal of Humanoid Robotics*, vol. 6, no. 03, pp. 337–359, 2009.

[107] N. Sprague, D. Ballard, and A. Robinson, "Modeling embodied visual behaviors," *ACM Transactions on Applied Perception (TAP)*, vol. 4, no. 2, p. 11, 2007.

[108] Z. Kong and B. Mettler, "Modeling human guidance behavior based on patterns in agent–environment interactions," *Human-Machine Systems, IEEE Transactions on*, vol. 43, no. 4, pp. 371–384, 2013.

[109] B. Mettler, Z. Kong, B. Li, and J. Andersh, "Systems view on spatial planning and perception based on invariants in agent-environment dynamics," *Frontiers in neuroscience*, vol. 8, 2014.

[110] G. Bales, J. Das, B. Linke, and Z. Kong, "Recognizing Gaze-Motor Behavioral Patterns in Manual Grinding Tasks," *Procedia Manufacturing*, vol. 5, pp. 106–121, 2016. [Online]. Available: http://linkinghub.elsevier.com/retrieve/pii/S2351978916300117

[111] A. Kennedy, "Eye tracking: A comprehensive guide to methods and measures," 2016.

[112] A. Duchowski, *Eye tracking methodology: Theory and practice.* Springer Science & Business Media, 2007, vol. 373.

[113] F. Cristino, S. Mathôt, J. Theeuwes, and I. D. Gilchrist, "Scanmatch: A novel method for comparing fixation sequences," *Behavior research methods*, vol. 42, no. 3, pp. 692–700, 2010.

[114] D. Noton and L. Stark, "Scanpaths in saccadic eye movements while viewing and recognizing patterns," *Vision research*, vol. 11, no. 9, pp. 929–IN8, 1971.

[115] A. T. Duchowski, J. Driver, S. Jolaoso, W. Tan, B. N. Ramey, and A. Robbins, "Scanpath comparison revisited," in *Proceedings of the 2010 Symposium on Eye-Tracking Research & Applications*. ACM, 2010, pp. 219–226.

[116] K. Holmqvist, M. Nyström, R. Andersson, R. Dewhurst, H. Jarodzka, and J. Van de Weijer, *Eye tracking: A comprehensive guide to methods and measures*. Oxford University Press, 2011.

[117] D. D. Salvucci and J. H. Goldberg, "Identifying fixations and saccades in eye-tracking protocols," in *Proceedings of the 2000 symposium on Eye tracking research & applications*. ACM, 2000, pp. 71–78.

[118] M. Nyström and K. Holmqvist, "An adaptive algorithm for fixation, saccade, and glissade detection in eyetracking data," *Behavior Research Methods*, vol. 42, no. 1, pp. 188–204, Feb. 2010. [Online]. Available: http://www.springerlink.com/index/10.3758/BRM.42.1.188

[119] J. R. Wolpaw and E. W. Wolpaw, Eds., *Brain-Computer Interfaces: Principles and Practice*. Oxford New York: Oxford University Press, 2012.

Appendix A

Electroencephalography

Electroencephalography (EEG) is a common, noninvasive method for recording brain signals in humans. The electrical activity of neurons within the neocortex generate detectable voltages that can be recorded via electrodes placed directly onto the scalp [16]. Attention, memory performance, and cognitive workload have been studied using signals acquired via EEG [17, 18]. EEG has also been employed in social human-robot interaction research [19] and Brain Computer Interface (BCI) implementations [20, 119]. These studies primarily include the magnitude and spatial distribution of spectral power in the θ (4-8Hz), α (8-12Hz), β (12-30Hz), and γ (>30Hz) bands.

Human brain regions and their putative functions are shown in Tables A.1. The EEG studies in this dissertation compare traditional power based analysis against functional-connectivity metrics as detailed in Figure A.1a and Figure A.1b. Neural recording techniques with varying levels of resolution starting from single neurons up through average activity measured on the surface of the scalp are summarized in Table A.2. Table A.3 lists the EEG frequency bands that are common to studies in neural activity. The 10-20 International Standard of EEG channel locations on the scalp is detailed in Figure A.2. Finally, the EEG hardware used for each of the experiments is shown in Figure A.3a and Figure A.3b.

Table A.1: Brain Regions and Functions
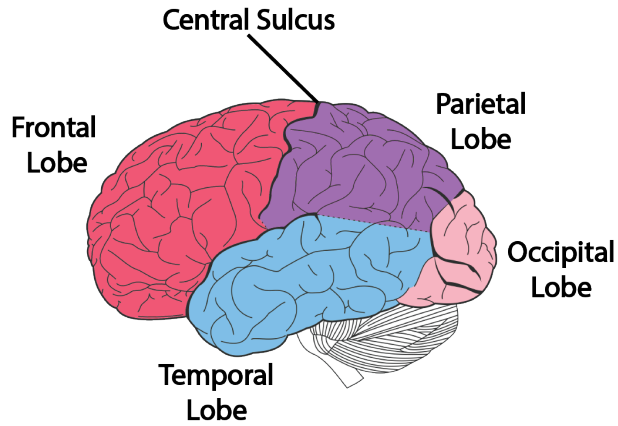
Lobe	Function
Frontal	• Behavior, emotions • Judgment, planning, problem solving • Body movement (motor strip) • Intelligence, concentration, self awareness
Parietal	• Interprets language, words • Sense of touch, pain, temperature (sensory strip) • Interprets signals from vision, hear, motor, sensory and memory • Spatial and visual perception
Occipital	• Visual processing, color identification
Temporal	• Memory • Hearing • Sequencing and Organization

Table A.2: Neuronal Recording Techniques

Recording Technique	Specific Methods
Electrical Recordings	• Electroencephalography (EEG) • Electrocorticography (ECoG) • Local field potential (LFP) • Single-unit recordings (spikes)
Magnetic Recordings	• Magnetoencephalography (MEG)
Neuronimaging Recordings	• Functional near-infrared recording (fNIR) • Functional magnetic resonance imaging (fMRI) • Positron emission topography (PET)
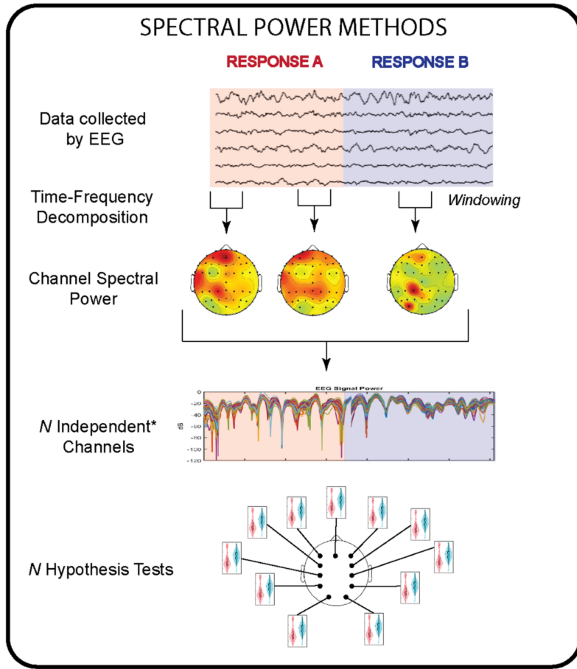
(a) Traditional power based methods   (b) Network based methods
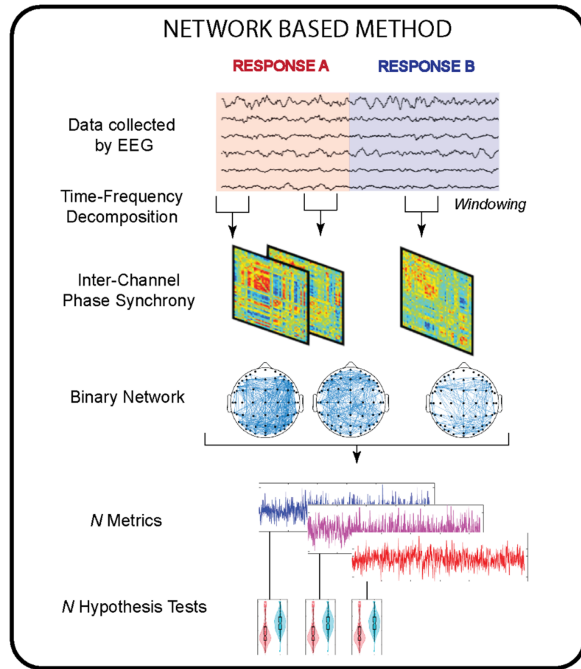
Table A.3: EEG Frequency Bands

Wave Type	Brain Location	Cognitive Description
θ (4-7Hz)	Various Locations	• Idling in adult (REM sleep) • Active when a person attempts to repress an action or response
α (8-15Hz)	Posterior region of the brain, both sides. Higher in amplitude on dominant side while the central sites at rest	• When eyes are closed and indicative of a relaxed/reflecting state • Associated with inhibition control (with purpose of timing inhibition in various brain locations)
β (16-31Hz)	Frontal lobe to both sides equally	• Alert or focused working state (active thinking or concentrating)
$\gamma > 31$Hz	Somato-sensory cortex (Midline brain sides to the anterior and posterior regions)	• Sensory processing • During short-term memory activities (heighten perception and problem solving) • At rest-state motor neurons
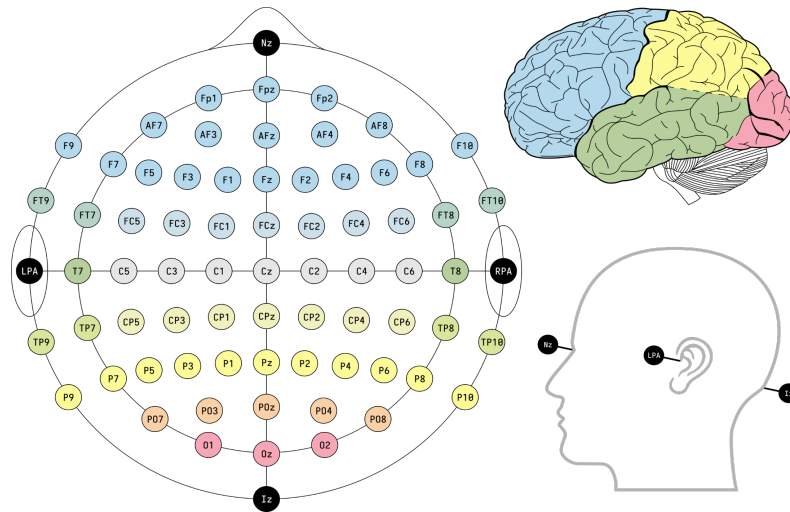
Figure A.2: The International 10-20 channel placement.
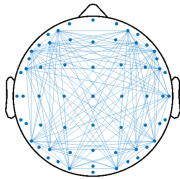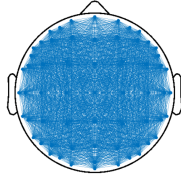
(a) Emotiv EPOC EEG headset used in Experiment 1

(b) g.tec g.HIAMP EEG headset used in Experiment 2

Appendix B

Network Theory

In this dissertation we use elements of graph theory to explore the interconnections between brain regions. Figure B.1 details the lobes of the brain along with a toy network for clarity.
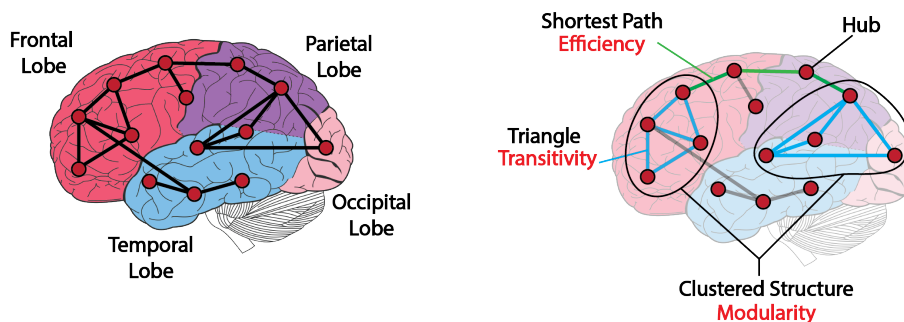
Figure B.1: Detail of brain lobes with embedded functional connectivity network.

A network is a binary, undirected graph $G = (V, E)$ comprised of a node set $V \in (1, 2, \ldots N)$ where N is the total number of nodes, and an edge set $E \subseteq V \times V$, where E is the edge set defined from the vertex set V. It is customary to describe the interconnectivity of the network nodes via a symmetric square matrix $A \in \mathbb{R}^{N \times N}$, known as the adjacency matrix. The elements of A are defined as

$$A_{lm} = \begin{cases} 1 & \psi_{lm} > \delta \\ 0 & otherwise \end{cases}$$

where ψ_{lm} is the phase synchrony between channels l and m. The parameter δ describes the maximum allowable phase difference. A dynamic network is one such that edges can form or dissolve as a function of time. Such a situation is known as dynamics of networks

since the number of nodes remains constant while the edges form and dissolve in time. Therefore, we can summarize the adjacency matrix as

$$A_{lm}(t) = \begin{cases} 1 & \psi_{lm}(t) > \delta \\ 0 & otherwise \end{cases}$$

Figure B.2a shows a toy example of such a network comprised of 12 nodes. Figure B.2b shows a dynamic network comprised on the same node set with edges that change with time.

(b) A dynamic network indexed by time. Nodes remain in existence, but network edges can form and dissolve in time.

(a) An binary, undirected network comprised of 12 nodes.

122

Appendix C

Network Metrics

The following sections list the network measures that have been used in this dissertation. Each network can be defined by a binary adjacency matrix A as described in Appendix B

C.1   Measures of Structure

Node Degree:

$$k_i = \sum_{j \in N} A_{ij}$$

The number of edges connected to node i

Degree Distribution:

$$P(k) = \sum_{k' \geq k} p(k')$$

The probability that a node will have a degree that is greater than or equal to k.

Average Neighbor Degree:

$$k_{nn,i} = \frac{\sum_{j \in N} A_{ij} k_j}{k_i}$$

The average degree of the neighbors of node i

Number of Triangles around a node i:

$$t_i = \frac{1}{2} \sum_{j,h \in N} A_{ij} A_{ih} A_{jh}$$

For each node i,

C.2   Measures of Integration

Characteristic Path Length:

$$L = \frac{1}{n} \sum_{i \in N} L_i = \frac{1}{n} \sum_{i \in N} \frac{\sum_{j \in N, j \neq i} d_{ij}}{n - 1},$$

where L_i is the average distance between nodes. The characteristic path length is the average of all the paths between all of the nodes. The distance d_{ij} is infinite for nodes located in separate disconnected componenets of the network. Consequently, one can use the inverse of the path length d_{ij}^{-1} which becomes zero for disconnected components. This leads to a definition of Global Efficiency

Global Efficiency:

$$E = \frac{1}{n} \sum_{i \in N} E_i = \frac{1}{n} \sum_{i \in N} \frac{\sum_{j \in N, j \neq i} d_{ij}^{-1}}{n - 1}$$

is the mean inverse path length between all of the paths between all of the nodes.

Transitivity:

$$T = \frac{\sum_{i \in N} 2t_i}{\sum_{i \in N} k_i(k_i - 1)}$$

The transitivity is a global measure the captures the average amount of closed triple connections divided by the number of all triple connections. It is the measure of how many of "my friends are friends of each other" in a network.

Clustering Coefficient:

$$C = \frac{1}{n} \sum_{i \in N} C_i = \frac{1}{n} \sum_{i \in N} \frac{2t_i}{k_i(k_i - 1)}$$

is a measure of the average number of triangles around a node. C_i is the clustering coefficient of the given node.

Local Efficiency:

$$E_{loc} = \frac{1}{n} \sum_{i \in N} E_{loc,i} = \frac{1}{n} \sum_{i \in N} \frac{\sum_{j,h \in N, j \neq i} a_{ij} a_{ih} \left[d_{jh}(N_i) \right]^{-1}}{k_i(k_i - 1)}$$

where the $d_{jh}(N_i)$ is the length of the shortest path between j and h that contains only neighbors of i.

Modularity:

$$Q_m = \frac{1}{2m} \sum_{i,j \in M} [A_{ij} - \gamma P_{ij}] \, \delta(\sigma_i, \sigma_j)$$

where $2m = \sum_{ij} A_{ij}$ is the total number of connections in the network, $\delta(\sigma_i, \sigma_j)$ is the Kronecker delta function, and P_{ij} is a null model. Maximizing Q_m requires optimization algorithms. The resulting modular structure is highly dependent on the density of the network, the type of null model, and the resolution parameter γ.

C.3 Measure of Resilience

Assortativity:

$$r = \frac{l^{-1} \sum_{i,j \in L} k_i k_j - \left[l^{-1} \sum_{i,j \in L} \frac{1}{2}(k_i + k_j) \right]^2}{l^{-1} \sum_{i,j \in L} \frac{1}{2}(k_i^2 + k_j^2) - \left[l^{-1} \sum_{i,j \in L} \frac{1}{2}(k_i + k_j) \right]^2}$$

It is a measure of correlation between nodes of high degree to nodes of low degree. Networks with positive assortativity, on average, poses high degree nodes that connect to other high degree nodes. Networks with negative assortativity, on average, contain high degree nodes that connect to low degree nodes.

Appendix D

Experiment 2: Statistical Tables

D.1 Hypothesis 1 Statistical Tables

Table D.1: Hypothesis 1: α Band Principal Component Statistics for the Factor Configuration

Principal Component	$F(1,176)$	p	$\Delta\mu_{LB}$	$\Delta\mu$	$\Delta\mu_{UB}$
4	5.59	1.92×10^{-2}	8.851×10^{-3}	5.355×10^{-2}	9.825×10^{-2}
5	6.46	1.19×10^{-2}	1.153×10^{-2}	5.159×10^{-2}	9.166×10^{-2}
8	5.46	2.06×10^{-2}	4.589×10^{-3}	2.960×10^{-2}	5.462×10^{-2}

Table D.2: Hypothesis 1: α Band Connectivity Statistics for the Factor Configuration

Connection	χ^2	p	$\Delta\mu_{LB}$	$\Delta\mu$	$\Delta\mu_{UB}$
AF3-F3	13.90	1.92×10^{-4}	1.645×10^{-3}	3.514×10^{-3}	5.197×10^{-3}
F7-FC5	69.08	1.11×10^{-16}	5.880×10^{-3}	7.886×10^{-3}	1.005×10^{-2}
F3-FC5	26.40	2.78×10^{-7}	3.035×10^{-3}	4.851×10^{-3}	6.706×10^{-3}
FC5-T7	37.22	1.05×10^{-9}	4.371×10^{-3}	6.522×10^{-3}	8.470×10^{-3}
F3-O1	23.06	1.57×10^{-6}	3.173×10^{-3}	5.469×10^{-3}	7.327×10^{-3}
FC5-O1	26.67	2.41×10^{-7}	3.459×10^{-3}	5.802×10^{-3}	7.728×10^{-3}
T7-O2	22.05	2.66×10^{-6}	3.022×10^{-3}	4.873×10^{-3}	7.253×10^{-3}
F3-P8	29.64	5.20×10^{-8}	3.526×10^{-3}	5.621×10^{-3}	7.875×10^{-3}
FC5-FC6	19.17	1.19×10^{-5}	2.730×10^{-3}	4.746×10^{-3}	6.973×10^{-3}
P8-FC6	21.81	3.01×10^{-6}	2.792×10^{-3}	4.664×10^{-3}	7.150×10^{-3}
P8-F8	26.492	2.65×10^{-7}	3.206×10^{-3}	5.375×10^{-3}	7.632×10^{-3}
F4-F8	7.17	7.41×10^{-3}	-4.420×10^{-3}	-2.341×10^{-3}	-7.778×10^{-4}
T7-AF4	21.94	2.81×10^{-6}	2.641×10^{-3}	4.763×10^{-3}	6.959×10^{-3}

Table D.3: Hypothesis 1: θ Band Principal Component Statistics for the Factor Configuration

Principal Component	$F(1, 176)$	p	$\Delta\mu_{LB}$	$\Delta\mu$	$\Delta\mu_{UB}$
1	4.05	4.58×10^{-2}	0.029	1.506	2.984
8	37.67	5.41×10^{-9}	-1.528	-1.156	-0.784
9	18.29	3.11×10^{-5}	0.447	0.831	1.214
12	26.38	7.40×10^{-7}	-0.999	-0.722	-0.444

Table D.4: Hypothesis 1: θ Band Connectivity Statistics for the Factor Configuration

Connection	χ^2	p	$\Delta\mu_{LB}$	$\Delta\mu$	$\Delta\mu_{UB}$
F3-FC5	42.66	6.51×10^{-11}	4.329×10^{-3}	6.121×10^{-3}	8.011×10^{-3}
F3-T7	24.28	8.34×10^{-7}	2.924×10^{-3}	5.177×10^{-3}	7.030×10^{-3}
F3-P8	23.49	1.26×10^{-6}	3.135×10^{-3}	5.536×10^{-3}	7.359×10^{-3}
P8-T8	14.45	1.44×10^{-4}	1.849×10^{-3}	3.651×10^{-3}	5.450×10^{-3}
P8-F8	26.23	3.03×10^{-7}	3.521×10^{-3}	5.575×10^{-3}	7.710×10^{-3}
T8-F8	17.06	3.62×10^{-5}	2.081×10^{-3}	4.351×10^{-3}	6.360×10^{-3}
FC6-F8	5.64	1.75×10^{-2}	-4.214×10^{-3}	-2.321×10^{-3}	-3.694×10^{-4}
F3-AF4	18.04	2.17×10^{-5}	2.670×10^{-3}	4.920×10^{-3}	6.874×10^{-3}
T7-AF4	34.90	3.47×10^{-9}	4.366×10^{-3}	6.519×10^{-3}	8.405×10^{-3}
F4-AF4	41.67	1.08×10^{-10}	4.596×10^{-3}	6.596×10^{-3}	8.747×10^{-3}
F8-AF4	20.97	4.66×10^{-6}	2.724×10^{-3}	4.780×10^{-3}	6.959×10^{-3}

D.2 Hypothesis 2 Statistical Tables

Table D.5: Hypothesis 2: α Band Principal Component Statistics for the Factor Performance

Principal Component	$F(1, 176)$	p	$\Delta\mu_{LB}$	$\Delta\mu$	$\Delta\mu_{UB}$
4	4.10	4.44×10^{-2}	1.154×10^{-3}	4.580×10^{-2}	9.044×10^{-2}
7	16.04	9.14×10^{-5}	3.170×10^{-2}	6.250×10^{-2}	9.330×10^{-2}
8	7.18	8.06×10^{-3}	8.865×10^{-3}	3.363×10^{-2}	5.839×10^{-2}
12	6.65	1.08×10^{-2}	4.912×10^{-3}	2.096×10^{-2}	3.700×10^{-2}

Table D.6: Hypothesis 2: α Band Connectivity Statistics for the Factor Performance

Connection	χ^2	p	$\Delta\mu_{LB}$	$\Delta\mu$	$\Delta\mu_{UB}$
F7-F3	21.84	2.96×10^{-6}	2.953×10^{-3}	5.102×10^{-3}	6.882×10^{-3}
F7-FC5	58.76	1.79×10^{-14}	5.362×10^{-3}	7.182×10^{-3}	9.221×10^{-3}
FC5-T7	50.94	9.52×10^{-13}	5.409×10^{-3}	7.449×10^{-3}	9.645×10^{-3}
O2-FC6	16.46	4.98×10^{-5}	2.433×10^{-3}	4.633×10^{-3}	6.617×10^{-3}
O1-F4	12.13	4.96×10^{-4}	1.364×10^{-3}	3.693×10^{-3}	5.811×10^{-3}
T8-F8	16.07	6.10×10^{-5}	-6.417×10^{-3}	-3.970×10^{-3}	-2.079×10^{-3}
FC6-F8	85.47	0.00	7.356×10^{-3}	9.394×10^{-3}	1.104×10^{-2}
P8-AF4	16.54	4.77×10^{-5}	2.167×10^{-3}	4.015×10^{-3}	6.331×10^{-3}

Table D.7: Hypothesis 2: θ Band Principal Component Statistics for the Factor Performance

Principal Component	$F(1, 176)$	p	$\Delta\mu_{LB}$	$\Delta\mu$	$\Delta\mu_{UB}$
1	7.35	7.36×10^{-3}	0.544	1.999	3.453
10	6.12	1.43×10^{-2}	-0.831	-0.462	-0.093
11	13.14	3.79×10^{-4}	0.291	0.639	0.987
12	14.49	1.94×10^{-4}	0.264	0.548	0.832

Table D.8: Hypothesis 2: θ Band Connectivity Statistics for the Factor Performance

Connection	χ^2	p	$\Delta\mu_{LB}$	$\Delta\mu$	$\Delta\mu_{UB}$
F7-T7	59.81	1.04×10^{-14}	-1.029×10^{-2}	-8.429×10^{-3}	-5.957×10^{-3}
FC5-P7	25.75	3.88×10^{-7}	-7.603×10^{-3}	-5.568×10^{-3}	-3.287×10^{-3}
F3-T8	21.57	3.41×10^{-6}	-6.391×10^{-3}	-4.470×10^{-3}	-2.437×10^{-3}
T7-F8	30.22	3.85×10^{-8}	-7.130×10^{-3}	-5.375×10^{-3}	-3.362×10^{-3}
P8-F8	15.84	6.90×10^{-5}	-6.418×10^{-3}	-4.382×10^{-3}	-2.132×10^{-3}
FC6-F8	21.07	4.43×10^{-6}	2.596×10^{-3}	4.642×10^{-3}	6.491×10^{-3}
F7-AF4	20.59	5.69×10^{-6}	-6.688×10^{-3}	-4.414×10^{-3}	-2.713×10^{-3}

Appendix E

Experiment 3: Trust Surveys

Please mark on each line at the point which best describes your feeling or impression (1 = disagree/never, 5 = agree/constantly).
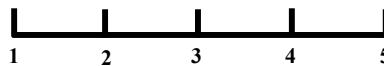
1. When I have a lot to do, it makes sense to delegate a task to automation.
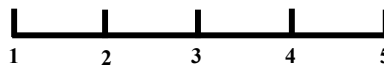
    1   2   3   4   5
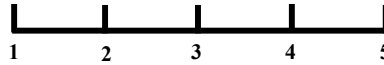
2. If life were busy, I would let an automated system handle some tasks for me.

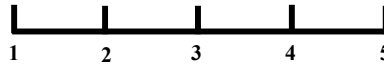   1   2   3   4   5

3. Automation should be used to ease people's workload.

    1   2   3   4   5

4. If automation is available to help me with something, it makes sense for me to pay more attention to my other tasks.

    1   2   3   4   5

5. Even if an automated aid can help me with a task, I should pay attention to its performance.

    1   2   3   4   5
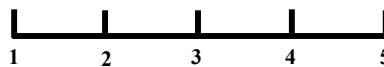
6. Distractions and interruptions are less of a problem for me when I have an automated system to cover some of the work.

    1   2   3   4   5

7. Constantly monitoring an automated system's performance is a waste of time.

    1   2   3   4   5

8. Even when I have a lot to do, I am likely to watch automation carefully for errors.

    1   2   3   4   5

9. It's not usually necessary to pay much attention to automation when it is running.

    1   2   3   4   5
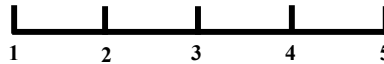
10. Carefully watching automation takes time away from more important or interesting things.

    1   2   3   4   5

Pre-Experiment Demographic Questionnaire

Title of research study: Space Habitats Optimized for Missions of Exploration

Investigator: Dr. Zhaodan Kong

1. Subject Number: _____

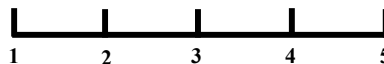2. Please state your: Age _____ and Sex _____

3. Please respond to the following statement: I got adequate sleep last night. (circle one)

   Strongly Agree   Agree   Neutral   Disagree   Strongly Disagree

4. How many hours of sleep did you get last night? _____

5. Have you consumed alcohol in the last 6 hours? (please circle one) Yes / No

6. Have you consumed coffee in the last 6 hours? (please circle one) Yes / No

7. Do you have a known history of seizures? (please circle one) Yes / No

8. What is your handedness/which is your dominant hand? _____

9. How often do you play video games? (please circle one or fill in one blank)

   Never   Monthly _____hrs. Weekly_____hrs.   Daily_____hrs.

10. Do you use robotic or autonomous systems at least once per week? Yes / No

    Please explain _____

11. Do you use a navigational aid (e.g., Google Maps, Waze, etc.) at least once week? Yes / No

12. What is your approximate level of experience with aerospace or spaceflight relevant
    information displays? (please circle one)

    No experience   Some experience   Moderate experience   Extensive experience

    Please explain _____

(Note: not at all=1; extremely=7)

1. The system is deceptive

1	2	3	4	5	6	7

2. The system behaves in an underhanded manner

1	2	3	4	5	6	7

3. I am suspicious of the system's intent, action, or outputs

1	2	3	4	5	6	7

4. I am wary of the system

1	2	3	4	5	6	7

5. The system's actions will have a harmful or injurious outcome

1	2	3	4	5	6	7

6. I am confident in the system

1	2	3	4	5	6	7

7. The system provides security

1	2	3	4	5	6	7

8. The system has integrity

1	2	3	4	5	6	7

9. The system is dependable

1	2	3	4	5	6	7

10. The system is reliable

1	2	3	4	5	6	7

11. I can trust the system

1	2	3	4	5	6	7

12. I am familiar with the system

1	2	3	4	5	6	7